UNIVERSITY OF BRASÍLIA
INSTITUTE OF GEOSCIENCES

GRADUATE PROGRAM IN APPLIED GEOSCIENCES AND GEODYNAMICS

INSIGHTS ABOUT DEEP MOONQUAKES ORIGINS

LYARA VILLANOVA SILVERIO

Master's Thesis
nº 182

Brasília
2021

UNIVERSITY OF BRASÍLIA
INSTITUTE OF GEOSCIENCES

LYARA VILLANOVA SILVERIO

INSIGHTS ABOUT DEEP MOONQUAKES ORIGINS

Thesis presented to the GRADUATE PROGRAM IN APPLIED GEOSCIENCES AND GEODYNAMICS of INSTITUTE OF GEOSCIENCES of UNIVERSITY OF BRASÍLIA as a partial requirement to obtain the Master's degree in APPLIED GEOPHYSICS.

Supervisor: *ELDER YOKOYAMA*

Brasília
2021

Villanova, Lyara S.
Insights about deep moonquakes origins. Villanova, L.S. Brasília, 2021, 127 páginas.

Orientador: Prof. Dr. Elder Yokoyama

Dissertação (mestrado) – Universidade de Brasília (UnB). Geofísica Aplicada – Programa de Pós Graduação em Geociências Aplicadas e Geodinâmica, 2021.

Inclui bibliografia e lista de figuras.

1. Geofísica. 2. Sismologia planetária. 3. Sismos lunares profundos.

Acknowledgements

First of all, I am grateful for all the difficulties, as they taught me about my limits, desires and dedication capacity.

Primeiramente, agradeço a todas as dificuldades, pois estas me ensinaram sobre os meus limites, anseios e capacidade de dedicação.

I am grateful to my parents, especially my mom, who gave me emotional support to overcome all the difficulties of life and my advisor, Elder Yokoyama, who more than working together in all my academic projects, was also helping and supporting in all my decisions and dreams, professional and personal. To you, teacher, I leave my 'Thank you very much' for being that 'big father' and I hope that we will continue to work together, even from afar. I also thank my "adoptive mother", Claudia, who supported me a lot in many ways.

Agradeço aos meus pais, em especial a minha mãe, que me deu suporte emocional para superar todas as dificuldades da vida e ao meu orientador, Elder Yokoyama, que mais do que trabalhar em conjunto em todos os meus projetos acadêmicos, também esteve auxiliando e apoiando em todas as minhas decisões e sonhos, profissionais e pessoais. A você, professor, deixo aqui o meu 'Muito Obrigada', por ter sido esse 'paizão' e espero que continuemos a trabalharmos juntos, mesmo de longe. Também agradeço a minha "mãe adotiva", Claudia, que me apoiou muito em vários sentidos.

I am grateful to my friends from the course and work colleagues, who made this path a little easier and less lonely. In particular, thank you very much, Matheus Figueredo, who helped me a lot in aspects of life, especially those that involved scripts and programming in general (laughs). Thank you very much Adlla, for all the support and friendship you have provided me. Thank you Dong, who supported me emotionally throughout the master's degree, and Yellinson, Vitória, Lavô, Brunna, Isabele, Matheus, Marcos, Douglas, Carlos, Gustavo, Bruno, for all the incredible moments. Thanks to you, I had the courage and strength to conclude.

Agradeço aos meus amigos de curso e companheiros de trabalho, que fizeram essa trajetória um pouco mais fácil e menos solitária. Em especial, muito obrigada a você, Matheus Figueredo, que me ajudou muito em quesitos da vida, principalmente os que involveram scripts e programação em geral (risos). Muito obrigada Adlla, por todo o apoio e amizade que você me propiciou. Obrigado Dong, que me apoiou emocionalmente durante o mestrado, e Yellinson, Vitória, Lavô, Brunna, Isabele, Matheus, Marcos, Douglas, Carlos, Gustavo, Bruno, por todos os momentos incríveis. Graças a vocês eu tive ânimo e força para concluir.

I am grateful to the employees of the Seismological Observatory, who helped me for almost 4 years with everything I needed, especially Dona Cida, with her coffee; Claudia, who kept our materials and spaces clean; Roberto and Dona Val, for their unforgettable warm conversations.

Agradeço aos funcionários do Observatório Sismológico, que tanto me auxiliaram durante

quase 4 anos em tudo o que precisei, em especial Dona Cida, com seu café; Claudia, que mantinha nossos materiais e espaços limpos; Roberto e Dona Val, por suas conversas inesquecivelmente calorosas.

I thank the Professors of the Institute of Geosciences, in particular George Sand, Luciana Prado, Susanne Maciel, Marcelo Rocha and Lucas Vieira who helped me a lot during my undergraduate and master's degrees.

Agradeço aos Professores do Instituto de Geociências, em especial George Sand, Luciana Prado, Susanne Maciel, Marcelo Rocha e Lucas Vieira que me ajudaram muito durante a graduação e durante o mestrado.

Finally, I would like to thank CAPES, for financial assistance during the entire period of research development, making everything possible.

Por fim, agradeço à CAPES, pelo auxílio financeiro durante todo o período de desenvolvimento da pesquisa, fazendo com que tudo fosse possível.

Silence in the deep
over a motionless span
relativity is special and general
warping shapes and appearances
passing through
growing apart space expands ephemeral
though in situ motionless
honeycombed membranes of virtual fields
sparked with a breath exhales the real

.

First breath and last
filling echoes with worlds words
mathematical constructions, chains of circumstance
curved filling slots with zeros and ones
others with something sharp
musically chorded ones
molecular symphonic combinations began,
woven across abyssal plains

.

Pieces travelling like ships
knight, kings and queens
bishop pairs viewing the long diagonals
of marine phytoplankton from a distance
like virtual particles
in all positions over the verse-waves
that could be or become and were
after silence shared the void

—UNKNOWN

Resumo

A gênese dos sismos profundos tem desafiado os cientistas há décadas. Cinquenta anos após a missão Apollo 11, algumas questões sobre as características geofísicas da Lua ainda permanecem sem resposta. Um deles envolve o mecanismo casual de terremotos lunares profundos, que são eventos sísmicos de baixa magnitude ($M \leq 2$) que variam de 700 km a 1200 km de profundidade. Embora a interpretação dos dados sismológicos das Missões Apollo tenha fornecido informações essenciais sobre a composição e estrutura da Lua, a relação entre esta estruturação e como as forças gravitacionais no sistema Terra-Lua-Sol influenciam eventos profundos ainda não está clara. Estudos anteriores sugerem que esses sismos lunares profundos podem ser desencadeados pela variabilidade gravitacional, produzida pelo movimento da Lua em torno da Terra (como os períodos/meses sinódicos, anomalísticos e siderais), ou seja, a periodicidade das marés. Os terremotos lunares profundos, por exemplo, foram associados à ciclicidade orbital lunar. No entanto, o estresse cíclico de maré não é suficiente para causar ruptura em pressões confinantes onde ocorrem os eventos profundos, uma vez que seus hipocentros ocorrem em áreas mais profundas e não são sensíveis ao estresse de maré. Na Terra, terremotos profundos ocorrem perto da zona de transição no manto e sua origem está frequentemente associada à desidratação de placas litosféricas. Além disso, a relação angular entre o apse lunar paralelo ao eixo de rotação da Terra tem sido associada a um aumento no número de grandes terremotos, devido ao estresse das marés. Aqui foi analisada uma série temporal de sismos lunares profundos (correlacionados com sismos terrestres profundos) com o número de eventos sísmicos por dia e parâmetros orbitais correspondentes calculados, como variações na distância, ocorrência angular e temporal entre a Lua e os planos orbitais Sol-Terra . Essa análise foi realizada usando as abordagens de Aprendizado de Máquina e Wavelet. Em contraste com estudos anteriores, os resultados sugeriram que os elementos orbitais sujeitos a distúrbios solares não influenciam significativamente os sismos lunares profundos. Alternativamente, os sismos lunares profundos estão principalmente relacionados a parâmetros orbitais que descrevem a posição da Lua em seu plano orbital, em relação ao sistema de coordenadas referenciado pela eclíptica e equinócio da época J2000.0 (onde as missões Apollo registraram todos os eventos que nós conhecemos). Os resultados mostram que estes eventos profundos são desencadeados pelo movimento da Terra e da Lua em seu próprio plano orbital. Aqui foi encontrado que a sismicidade profunda advêm dos movimentos orbitais de Inclinação do plano lunar (IN), Longitude do Nodo Ascendente (OM), Anomalia Verdadeira (TA) e Argumento do Perifoco (W). Sismos profundos ocorrem em regiões sísmicas específicas, sugerindo que a sismicidade pode ser induzida por fatores externos ao corpo planetário. Esses resultados também sugeriram que a Terra e a Lua possuem camadas específicas com comportamento elástico que respondem sismologicamente de forma semelhante.

Palavras-chave: Lua, sismos lunares, profundo, sismicidade, periodicidade, ciclicidade, mecanismo físico.

Abstract

The genesis of deep quakes has been challenged scientists for decades. Fifty years after the Apollo 11 mission, some questions on the geophysical characteristics of the Moon still remain unanswered. One of them involves the casual mechanism of deep moonquakes, which are low magnitude seismic events ($M \leq 2$) that ranges from 700 km to 1200 km in depth. Although the interpretation of seismological data from the Apollo Missions has provided essential information on the composition and structure of the Moon, a relationship between this structuration and how the gravitational forces in the Earth-Moon-Sun system influence deep moonquakes is still unclear. Previous studies suggest that these deep quakes can be triggered by gravitational variability, produced by the motion of the Moon around the Earth (such as the synodic, anomalistic, and sidereal periods/months), i.e., tidal periodicity. Deep moonquakes, for example, have been associated with lunar orbital cyclicity. However, cyclic tidal stress is not sufficient to cause rupture at confining pressures where deep moonquakes occur, since its hypocenters occur in deeper areas and may not be sensitive to tidal stress. On Earth, deep quakes occur close to the transition zone in the mantle and their origin is often associated with dehydration of lithospheric slabs. Also, the angle relation between the lunar apse parallel to the axis of rotation of the Earth has been associated with an increase in the number of large earthquakes, due to tidal stresses. Here was analyzed a time series of deep moonquakes (correlating with deep earthquakes) with the number of seismic events per day, and calculated correspondent orbital parameters, such as variations in distance, angular and temporal occurrence between the Moon and the Sun-Earth orbital planes. This analysis was performed using Machine Learning and Wavelet approaches. In contrast to previous studies, the results suggested that the orbitals elements subject to solar disturbances do not significantly influence deep moonquakes. Alternately, deep moonquakes are mainly related to orbital parameters that describe the position of the Moon in its orbital plane, in relation to the coordinate system referenced by the ecliptic and equinox of the J2000.0 epoch (where Apollo missions recorded all the events that we know). The results show that deep quakes are triggered by the movement of the Earth and the Moon in their own orbital plane. Here was found that deep seismicity arises from the orbital movements of Inclination of the lunar plane (IN), Longitude of Ascending Node (OM), True Anomaly (TA), and Argument of Perifocus (W). Deep quakes occur in specific seismic regions suggesting that seismicity may be induced by external factors to the planetary body. These results also suggested that the Earth and the Moon have specific layers with elastic behavior that respond seismologically in a similar way.

Keywords: Moon, moonquakes, deep, seismicity, periodicity, cyclicity, physical mechanism.

Contents

List of Figures

CHAPTER 1

Introduction

Since ancient times, humankind has been digressing about the relationship between the Moon and life on Earth (Badescu, 2012). For example, the Chinese had the myth of Chang'e, a lunar goddess. In the same way, the Greeks had the lunar goddess Selene, who drove a chariot across the dark sky. All these myths helped humankind to understand the Moon before modern science that arising at about 1600 CE (Silveira, 2009). The scientific knowledge about the Moon has developed continuously from the observations of Galileo Galilei, in the 17th century, having its peak during the Apollo space missions (Badescu, 2012).

Although robust knowledge about the Moon had been produced over the centuries, several issues about their origins and evolution remain uncleared, such as the Moon origin itself. The most widely accepted hypothesis of the Moon's origin postulate that a planetary body about the size of Mars collided with Earth 4.5 billion years ago. This impact sent materials from the Earth and the body through space and part of them came together, due to forces and orbital movements around the Earth, forming the Moon (Figure 1.1). Unlike the Earth, the Moon preserves most of its geological evolution history. Thus, due to the proximity of Earth and its origin relationships (Kuskov and Fabrichnaya, 1994; Kuskov and Kronrod, 1998; Lognonné et al., 2003; Hao et al., 2018; Watters et al., 2019), the Moon has been increasingly targeted for studies focused on understanding the evolution of the primitive Earth (Frohlich and Nakamura, 2009; Kolvankar and Atomic, 2010; Gupta, 2012; Zhao et al., 2012; Jaumann et al., 2012).

Among the Earth-Moon relationships, gravitational is the most important, controlling from the movement of the fluid at the mantle-core boundary to the position of the Earth's orbital axis at an inclination of 23.4° (Figure 1.2). This angle ensures climate stability and defines the swell of terrestrial tides. The effects of tidal forces (from oceanic fluids and solid earth) are caused by Earth's orbital motion around its axis that is faster than the Moon in its orbit. Therefore, the Earth tends to accelerate the rotation of the Moon and, at the same time, the Moon tends to pull the Earth, decreasing the rotation velocity of the planet. The friction resulting from this tug of war forces the Moon into a wider orbit, and the interaction of these Forces causes the effects of a solid-body tide, which affects the Moon's gravitational torque and its orientation in space (Pavlov et al., 2016; Cuk et al., 2016; Canup and Asphaug, 2018; Hachay and Khachay, 2019). According to Williams and Boggs (2015) the influence of the solid body tide for an elastic sphere is small. However, the presence of energy dissipation in the subsurface material introduces changes in the model that depend on the time in which a specific point on the body was submitted to the applied Force. The friction resulting from this tug of war forces the Moon into a wider orbit, and the interaction of these Forces causes the effects of a solid-body tide, which affects the Moon's gravitational torque and its orientation in space (Pavlov et al., 2016; Cuk et al., 2016; Canup and Asphaug, 2018; Hachay and Khachay, 2019).

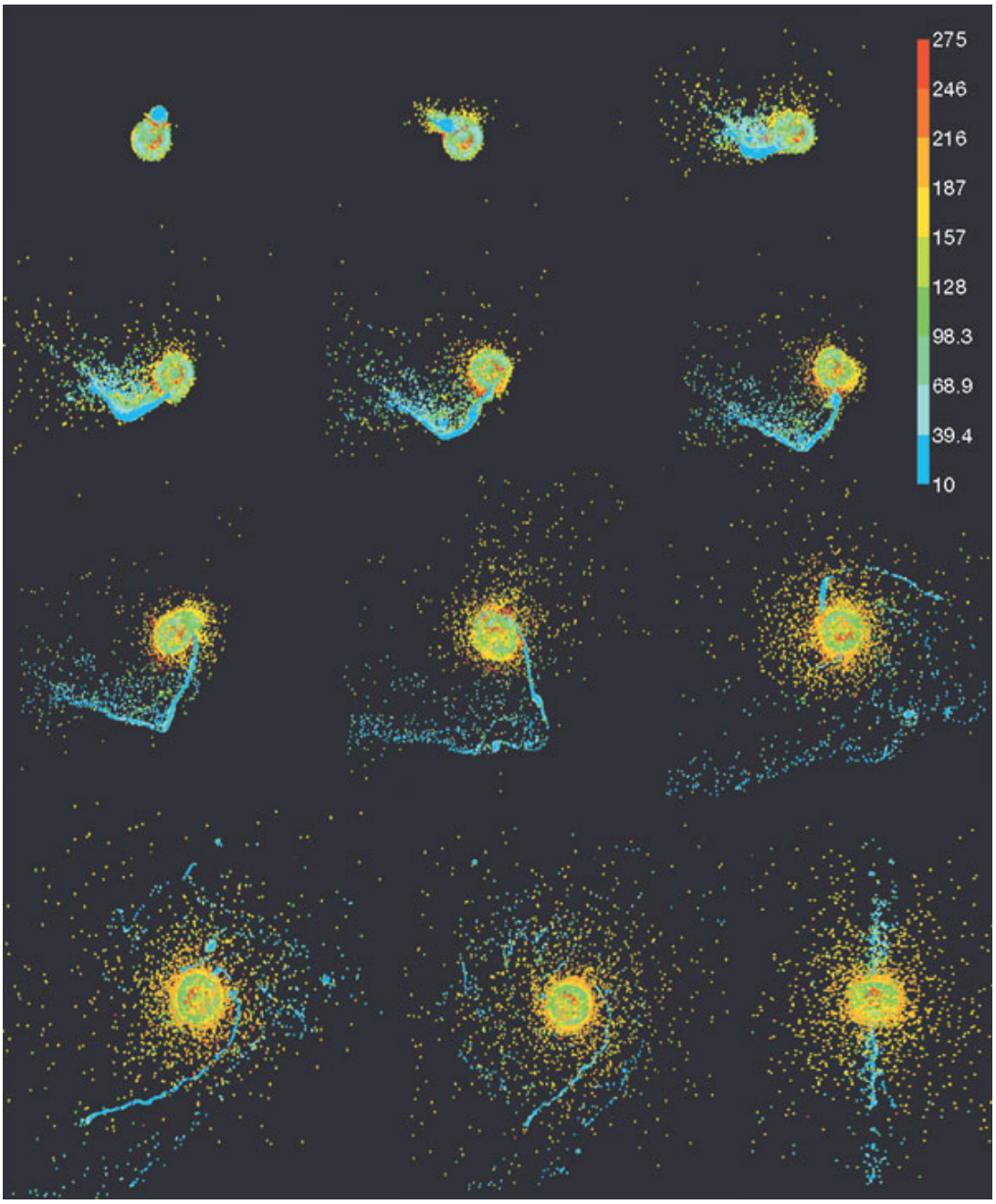

Figure 1.1 Time series of simulation of the forming impact of the Moon. Results are shown looking down onto the plane of the impact at times = 0.3, 0.7, 1.4, 1.9, 3, 3.9, 5, 7.1, 11.6, 17 and 23 hours. Colour scales shown on the colour bar in units of $6.67x10^{8} erg.g^{-1}$. From Canup and Asphaug, 2001.

The elastic characteristics of the solid medium are directly linked to the capacity to accumulate stresses of materials (Pernet-Fisher et al., 2019) and release the accumulated energy that, in general, occurs through quakes (Burmin et al., 2016; Watters et al., 2019). In terms of comparison, terrestrial earthquakes generally last around half a minute. On the other hand,

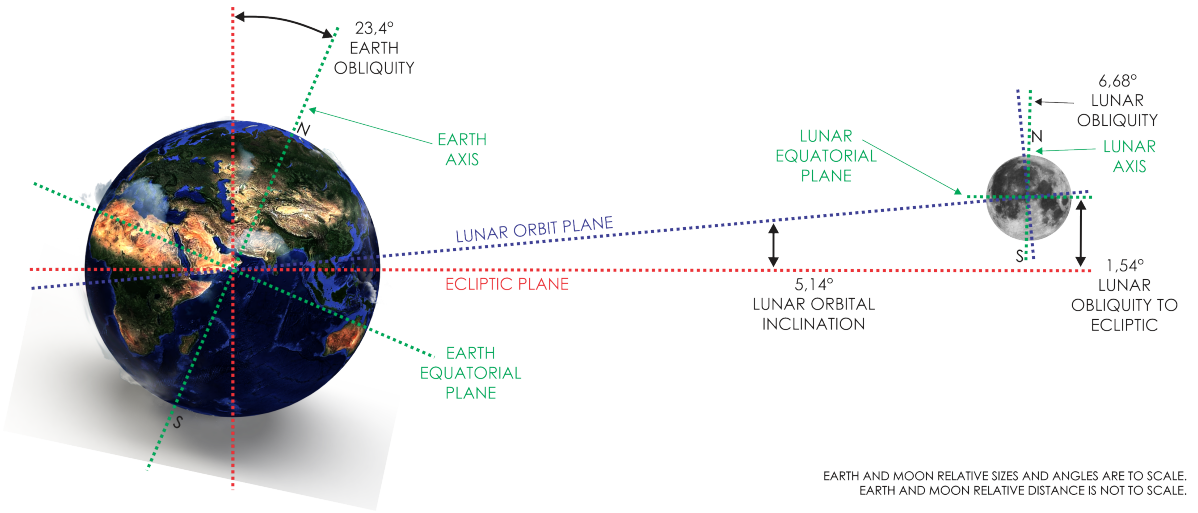

Figure 1.2 Angular relations between Moon and Earth.

moonquakes can last from 10 minutes to a few hours. The cause of these moonquakes is not clear, but they highlight one of the reasons why liquid water is of paramount importance in the composition of the Earth, in contrast to the lunar subsurface, which is much drier: This helps to spread the released energy, damping the vibrations of earthquakes (Karato, 2013; Kronrod et al., 2018). Thus, studying moonquakes, their characteristics, their causalities, and their forms of occurrence, can help in understanding how seismic activity on Earth could be during periods with less liquid water (as in the Glacial Ages or during the formation of the planet), in a better comprehension of the cause and effect relationships in the Earth-Moon system, since, proportionally, what happens on the Moon also occurs on Earth, according to the physical laws of action and reaction (Kolvankar and Atomic, 2010) and the understanding of causal mechanisms of quakes in general (Kuskov et al., 2016), therefore, the physical model generated to explain the occurrence of moonquakes may also be applied to Earth in future studies, helping to understand the causalities of earthquakes.

In the context, one of the most relevant contributions was the registration of about 13,000 moonquakes (Nakamura, 2005), which were subdivided (Figure 1.3) into shallow moonquakes, deep moonquakes, thermal moonquakes and impact moonquakes. The recording and interpretation of these data provided essential information about the composition (Kuskov and Kronrod, 1998; Gagnepain-Beyneix et al., 2006; Jaumann et al., 2012; Kuskov et al., 2016; Pernet-Fisher et al., 2019; Zhao et al., 2019) and the internal structure of the Moon (Lognonné et al., 2003; Nakamura, 2005; Weber et al., 2010; Zhao et al., 2012). However, some questions about the deepest lunar seismicity are still a subject of debate, such as the mechanism that generates these deep moonquakes, the periodicity of their occurrence, and the frequency of the locations of the epicenters of the events.

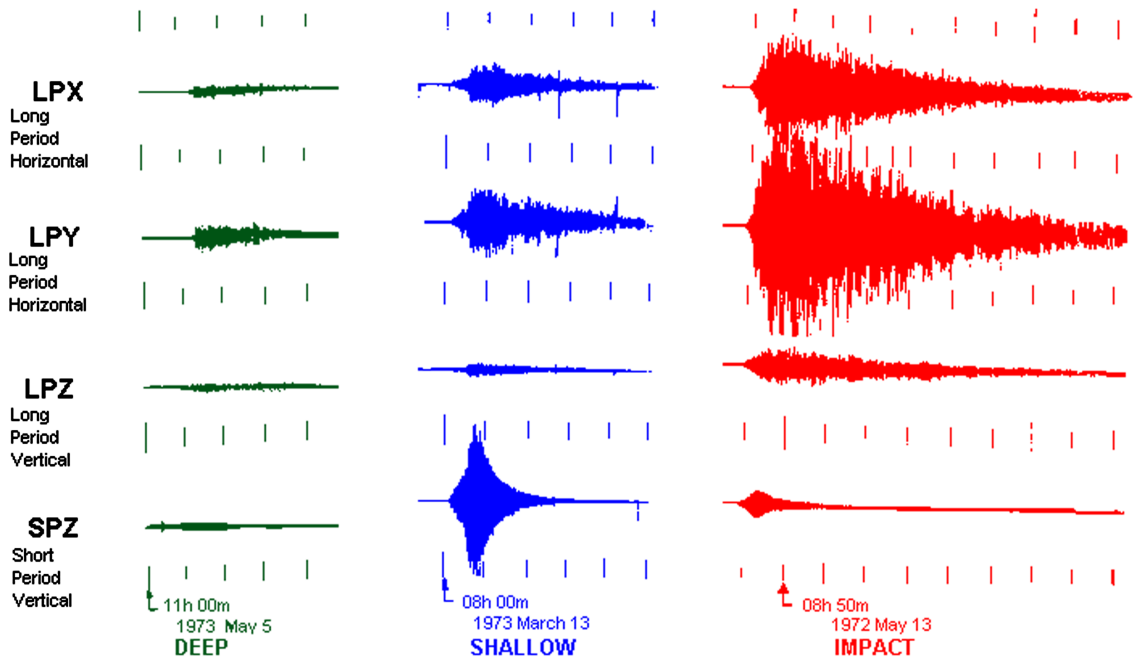

Figure 1.3 Typical seismic signature of moonquakes, observed in the recorded data. Each moonquake type has a different amplitude and recording time from each other. Each line on the time scale is equivalent to 10 minutes. Adapted from Nunn et al., 2020.

1.1 Objectives

The main objective of this thesis is to reinterpret lunar seismology data to refine the understanding of the physical causal mechanism of deep moonquakes and their cyclicity of occurrence.

Specifically, the research aimed to (i) analyze the depth and shape of the lunar regolith layer below the seismographic stations, which strongly influences the noise recorded in seismograms; (ii) to understand the causality and cyclicality in the occurrence of deep moonquakes, which are also related to deep earthquakes; and (iii) correlate the causality of events with geological and orbital mechanisms, based on information on frequency, amplitude and recording time extracted from the events.

1.2 Thesis structure

This thesis is set up in 5 chapters. The first is an introductory chapter, where it is possible to have an overview of the relationship between the Earth and the Moon, the formation and evolution of the Moon, and its seismicity. The second chapter is the theoretical background, which comprise the rheological/geological evolution, the seismological acquisition made in the Apollo missions, and the orbital parameters that influence the evolution of the Earth-Moon

system. The third chapter is about the data used, how the database was made, pre-processed, and processed.

Chapter 4 contains the results, which are subdivided into papers 1, 2, and 3. The regolith is indicated as the most influencing parameter in the noise contained in the record of seismic experiments. Paper 1 analyzes the regolith layer below the Apollo stations, where there were active seismic experiments (Apollo 14 and 16), in order to understand whether the composition, age, layer shape, and variability of the grains in each geological site of the Moon change the noise registered. Paper 2 suggests the physical causal mechanism of deep moonquakes, as well as correlating them with the occurrence of deep earthquakes. Deep quakes showed a correlation in their period of occurrence and also occur in specific structural layers. Paper 3 investigates whether the orbital factors pointed out in Paper 2 also influence noise, in addition to influencing the occurrence of deep quakes. Although the regolith, discussed in paper1, is the most influencing factor, orbital factors also subtly influence the noise recording.

Finally, chapter 5 brings the final considerations.

CHAPTER 2

Background

Each Apollo seismographic station was installed in a geological area with different chemical compositions, ages, and evolution in each terrain. This implies different responses of the seismological records and models in each acquisition site. For this reason, understanding the rheological/geological evolution, the seismological records made in the missions, and the orbital parameters that influenced the evolution of the Earth-Moon system are of prime importance for the interpretation and discussion of the models, as well as the physical mechanisms influencing the moonquakes.

2.1 The Apollo Seismographic Network and the records

Seismographic stations were installed on the lunar surface during Apollo 11, 12, 14, 15, and 16 missions. The Apollo 11 station operated just 21 Earth days before lost its signal, which ended its operation. The remaining four stations (Apollo 12, 14, 15, and 16) make up the Apollo Seismographic Network. This network covers only the frontal center of the Moon in an area similar to an equilateral triangle with a spacing of 1100 km between the stations (stations 12 and 14 are separated by 181 km in one corner of the triangle) (Figure 2.1).

Each seismographic station consists of three long-period sensors combined and orthogonally aligned to measure a vertical component (LPZ) and two horizontal components (LPX and LPY). The station also includes a single-axis short-period sensor (SPZ) sensitive to vertical movement at higher frequencies (for more specifications, see Appendix IV).

At Apollo 17 (Figure 2.1), the equipment implemented was a lunar surface gravimeter (LSG), not a seismometer. The primary objective was for LSG to use the Moon as an instrumented antenna to detect the gravitational wave predicted by Einstein's theory of general relativity. A secondary objective would be to measure the deformation of the Moon's tidal forces. However, when the instrument was turned on, it was not possible to balance it in the proper position. It was then determined that an error in arithmetic made by La Coste and Romberg (NASA, 1980) had not been corrected, so the instrument had an excellent performance on Earth, but was out of tolerance for lunar gravimetric variations. This changed the frequency response of the sensor to a significantly higher than intended. The initial analysis of the recorded data of the Apollo 17 was made at the University of Maryland, indicating that the LSG did not function to detect gravitational waves, but could detect some lunar seismic events. Direct comparisons of LSG data with other seismic measuring devices on the Moon showed that it had, within a narrowband, a greater degree of sensitivity. Koyama and Nakamura (Koyama and Nakamura, 1979) analyzed the LSG seismic data and concluded that they were of sufficient quality for

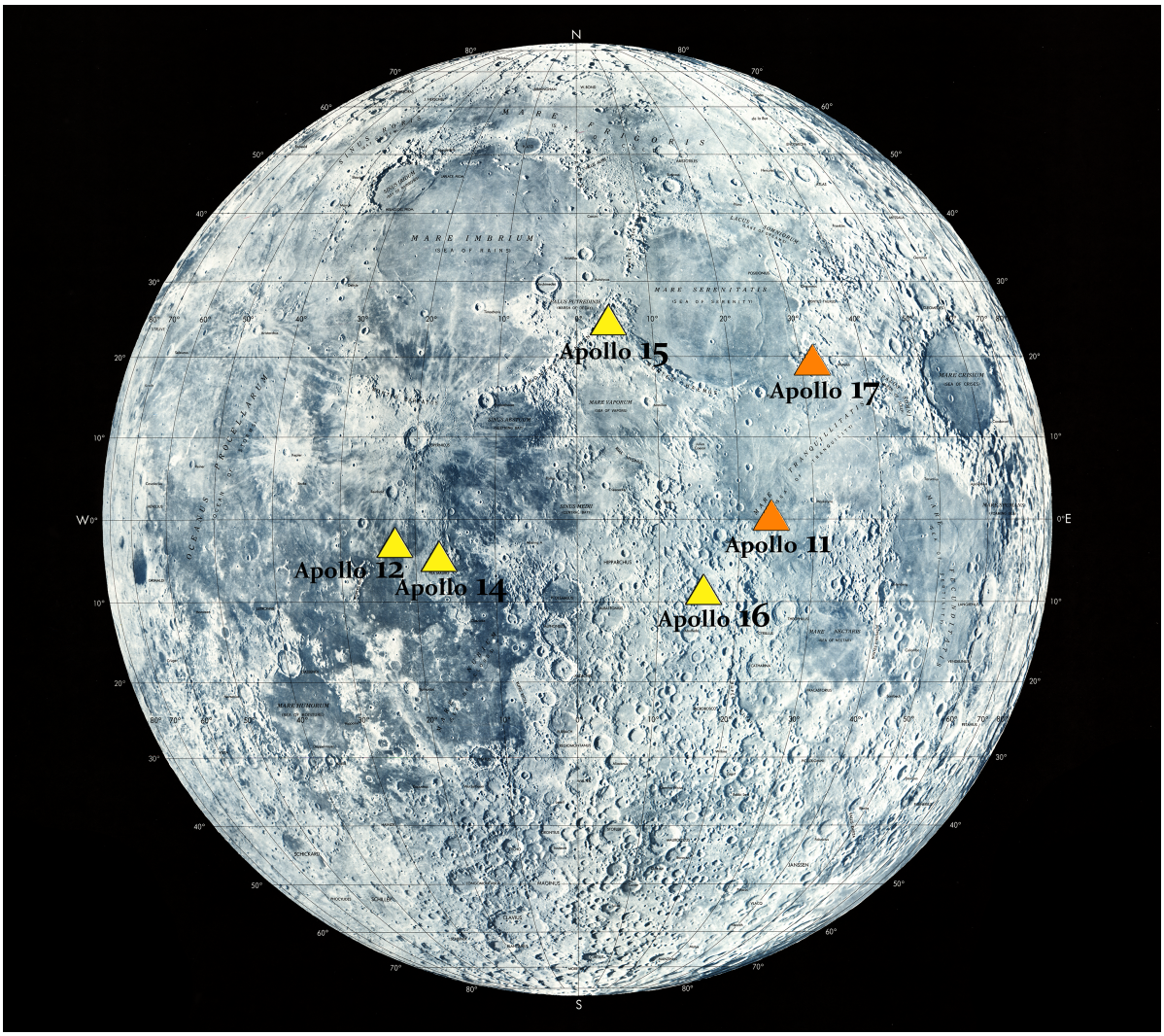

Figure 2.1 Apollo seismographic network, represented by yellow triangles. Orange triangles represent stations that recorded events, but due to their short operating time (Apollo 11) or their type of equipment (Apollo 17), they are not considered part of the network.

analysis together with the data from the Apollo Seismographic Network.

Lunar seismic signals have emergent beginnings, gradually increase to a maximum and then slowly decline, lasting up to several hours (on Earth, signal durations under equivalent conditions would be measured in minutes). After the first or the first two cycles of the initial movement of the P wave, the movement of the ground (regolith) becomes so complex that there is little or no correlation between any two components. Thus, many of the analysis techniques considered useful in terrestrial seismology cannot be applied to lunar signals, and it is rarely possible to determine the direction of propagation of the particle movement by analyzing a single station (Latham et al., 1972). These and other unusual characteristics of lunar seismic signals have been interpreted as resulting from waves that were subjected to high dissipation due to the heterogeneous layer in terms of composition and depth of regolith that covers the

entire surface of the Moon. Part of the dissipated energy gradually propagates to the lunar interior as a long signal of seismic waves, it undergoes new dispersion when it enters the lunar surface layer again and is observed as a prolonged signal in another station (for additional understanding about the lunar regolith and its influence on the seismic record, see Paper 1 and Paper 3, in Chapter 4: Results and discussions).

The background noise in the records of each station has different characteristics, apparently related to the depth and elastic properties of the regolith in each site. This would explain the much greater sensitivity at station 16, for example, in relation to the records compared across all stations. To explain these differences, below station 16 should have a greater regolith thickness than below other Apollo stations, according to the applied criteria (Villanova et al., 2021a).

Passive seismic experiments of the Apollo missions allow identifying different types of natural seismic sources, which reflect the dynamic state of the lunar interior and the interplanetary environment around the Moon. Deep moonquakes are events of small magnitude that are often correlated to tidal forces generated by the Earth and the Sun (Frohlich and Nakamura, 2009; Weber et al., 2010; Harada et al., 2014). The total number of distinct epicenter locations identified to date is 166 (Nakamura, 2005). Shallow moonquakes have a predominantly high-frequency signal and are called HFT events (High-Frequency Telessismic). Frohlich and Nakamura (Frohlich and Nakamura, 2009) observed that the occurrence of HFT events is correlated with the lunar sidereal period of 27.32 days, that is, HFT events are significantly more common when the seismic network at the front of the Moon is oriented in a particular direction with respect to the celestial sphere. Thermal moonquakes are very small disturbances caused by temperature variations on the moon's surface. They are detectable only up to a few kilometers away from a seismic station. The mechanism for its generation is not well understood, but it appears to originate in young craters and large rocks. Impact moonquakes are not from an internal causality and, therefore, do not represent true lunar seismicity. However, it is an important source of information about the interplanetary environment. These meteoroids detected by long-period seismometers have estimated mass ranging from 500 g to 50 kg (Latham et al., 1972). The much more numerous impacts detected by short-period seismometers represent those of smaller masses. Small meteoroids (less than 1 kg) show a strong cluster in a region of impacts, many of which are identified as rains known from terrestrial meteor studies. Large meteoroids (more than 1 kg) can be derived from asteroids close to Earth.

Previous studies have been suggesting that peaks in the total activity of deep moonquakes, taken as the sum of all events detected in a given station per unit of time, occur at intervals of about 14 days. This periodicity was first published by Latham et al. (1972) (Figure 2.2). The most prominent peaks in the graph of Figure 2.2 occur over periods of 14 and 28 days. These are the periods of the main tidal components, close to the lunar position of its apogee and perigee. However, the pattern of occurrence is not simply related to monthly changes in the apogee-perigee cycle. Indeed, this pattern may also be associated with other components of solar and terrestrial disturbances in lunar orbit (see Paper 2, in Chapter 4: Results and discussions).

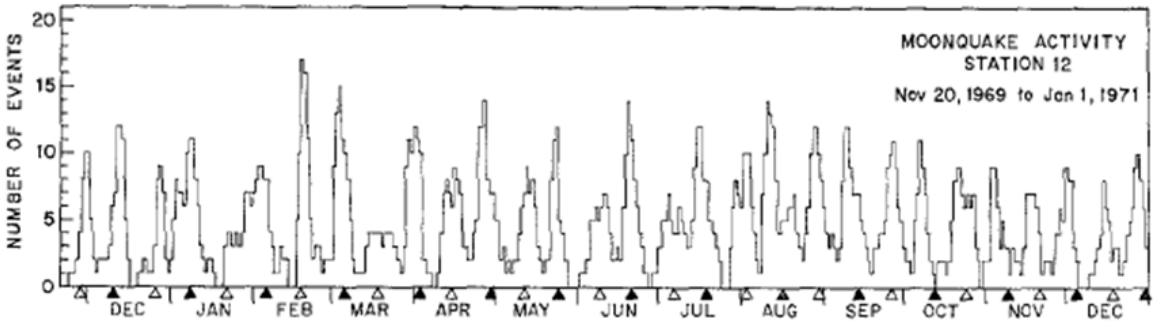

Figure 2.2 Number of moonquakes per day recorded at station 12 between November 20, 1969 and January 1, 1971. Black triangles indicate perigee and white triangles indicate apogee. From Latham et al., 1972.

2.2 Lunar seismology

Lunar seismicity has events with different moment magnitudes and distributions at different depths (Kuskov and Fabrichnaya, 1994; Lognonné et al., 2003; Nakamura, 2005; Frohlich and Nakamura, 2009; Weber et al., 2010; Zhao et al., 2012; Harada et al., 2014; Kuskov et al., 2016; Hao et al., 2018; Watters et al., 2019; Hachay and Khachay, 2019). The events are classified according to the depth of their epicenters, being impact (on the surface, with magnitudes varying according to the characteristics of the impact body and impact speed), thermal (approx. 50 m deep, in the crust, with varying magnitude), shallow (between 50 and 200 km deep, with magnitudes $\geq$ M5) and deep (between 700 and 1200 km deep, with magnitude $\leq$ M2). Current studies on the more superficial seismicity show that the occurrence of thermal moonquakes is associated with the expansion and compression of the lunar crust, due to the wide variation in thermal amplitude on a lunar day (Weber, 2016) and the occurrence of shallow moonquakes is associated the generation of failures and movement of the regolith (Ling et al., 2019; Watters et al., 2019). The deeper seismicity, on the other hand, has been the subject of studies for a longer time, due to its cyclical occurrence, which is not so well observed in other types of moonquakes, but its causality and its physical generating mechanism are still not well understood (Nakamura, 2005; Frohlich and Nakamura, 2009; Weber et al., 2010; Hao et al., 2018; Hachay and Khachay, 2019). The constant recurrence of deep moonquakes shows that the study region (lower mantle and core-mantle boundary (CMB)) is too complex and dynamically active.

From an analysis of the timing of these events, it was observed that the occurrence of most shallow moonquakes was closely linked to the distance of the Moon in relation to Earth (Watters et al., 2019). The analytical modeling, carried out by Watters et al. (2019), of the tidal forces that contribute to the state of lunar stress, indicated that these events occur at or near the peak of compressive stress, which occurs at the apogee. A global fault network was discovered by analyzing high-resolution images (0.5 - 2 m/pixel), obtained by the Lunar Reconnaissance Orbiter (LRO) mission, confirming that the Moon suffered a recent global stress contraction, where the influence of solid earth tidal forces contributes significantly to the state of lunar tension (Harada et al., 2014; Pavlov et al., 2016; Cuk et al., 2016; Hao et al., 2018). Tidal

stresses superimposed on tensions arising from contraction result in non-isotropic compressive stresses consistent with fault orientations. According to Watters et al. (2019), in the apogee, the daytime tensions are more compressive near the tidal axis, while in perigee they are more compressive at 90° from the tidal axis. These results were related to the distance from Earth to the Moon over the Apollo seismic experiment. The demodulation of the time series showed a non-random distribution of shallow moonquakes with the distance from the apogee at the time of occurrence of the events. This grouping of events reflected, then, that the orbital speed of the Moon is lower in the apogee compared to the speed in the perigee (defined by Kepler's laws), with more time for the accumulation of tensions near the apogee than for any other position in the lunar orbit.

In recent years, models of the lunar internal structure have been explored more intensively, complementing Apollo's seismic data with selenodetic data from NASA's Gravity Recovery and Interior Laboratory (GRAIL) and Lunar Laser Ranging (LLR) missions. Important information about the thickness of the crust, low velocity/viscosity zone, and seismic wave velocity was obtained, but the structure and composition of the lunar mantle and the lunar core are still uncertain (Kronrod et al., 2018). The difference in the concentrations of refractory elements can be interpreted by models of the origin and geological/rheological evolution of the Moon. To answer these questions, studies have been developed whose general methodology is to combine geophysical and geochemical models and a thermodynamic approach (Kuskov and Fabrichnaya, 1994; Lognonné et al., 2003; Gagnepain-Beyneix et al., 2006; Zhao et al., 2012; Kuskov et al., 2016; Kronrod et al., 2018; Kuskova et al., 2018), in order to corroborate composition and structure, where physical factors are listed, such as mean lunar radius (R), mass (M), mean moment of inertia (Is) and Love Numbers of the gravimetric potential of grade 2; Mineral physical properties, such as density gradient in the mantle and geochemical restrictions, according to the theory of Moon formation derived from an impact on Proto-Earth and; Travel time data of seismic waves, to form a probability function (Kronrod et al., 2018).

The variation in the amplitude of influence of the tidal forces in a solid planetary body occurs by dissipation, depending on its structural, thermal, and orbital states. It is expected, according to calculations of the Moon's response to these Forces (Harada et al., 2014; Williams et al., 2017), that the attenuation of seismic waves in the deepest part of the Moon is consistent with a low viscosity layer at the core-mantle boundary, being able to explain the dependence of the dissipation to the frequency observed geodetically in the period of the lunar tides. Harada et al. (2014) numerically simulated the lunar viscoelastic response for a layer with frequency-dependent tidal dissipation, which corresponded to the measurements of tidal dissipation in the monthly and annual periods. Compared to the lunar Asthenosphere, the viscosity calculated in the lunar Mesosphere is low. This suggests that partial melting at the core-mantle boundary and tidal dissipation not evenly distributed within the lunar interior, but located in the low viscosity layer. These conditions imply that this layer may directly influence the thermal evolution of the Moon.

The conclusion obtained from the results of the researches developed so far (Lognonné et al., 2003; Gagnepain-Beyneix et al., 2006; Zhao et al., 2012; Harada et al., 2014; Kuskov et al., 2016; Williams et al., 2017; Kronrod et al., 2018), in this scope, is that a low viscosity layer exists at the core-mantle boundary, inducing strong tidal dissipation, being equivalent to

the high attenuation zone determined seismologically. Likewise in the Earth, the lunar core-mantle boundary would be surrounded by an ultra-low viscosity zone, which may correspond to a fusion or even a critical rheological state. The inverse relaxation time of the ultra-high zone is close to the rate of angular variation of the lunar orbit. According to Harada et al. (2014), this is probably the consequence of a stable thermal balance, where the variation of the tidal range of influence in the low viscosity layer balances the heat transport due to solid-state convection, in addition to the possible liquid migration if the partial merger occurs. It is worth mentioning that tidal heating is located within the low viscosity zone, that is, the low viscosity layer plays a role as a "blanket" for the cooling of the core, resulting in a delay of the dynamo.

2.3 Implications of the Moon's internal evolution

The Moon and the Earth form a system that has a center of mass in common. A complete lunar orbit around the Earth takes 27.3 days (Sidereal Period) and periodic changes in the geometry of the Earth-Moon-Sun system (which are responsible for the lunar phases) are repeated every 29.5 days (Synodic Period). The rotation velocity of the Moon decreased from the beginning of its formation until the present moment due to the friction of the tidal forces, being locked in a synchronous state, so that the same lunar hemisphere is always sighted from Earth (Kolvankar and Atomic, 2010; Gupta, 2012; Jaumann et al., 2012).

According to Jaumann et al. (2012), the thermal evolution of the Moon can be summed up as a quick joining of part of the pulverized materials coming from the impact of a planetary body with the Proto-Earth; The development of a global ocean of magma, whose fractional crystallization resulted in the deposition of mafic minerals (originating an ultramafic mantle) and in the rising concentration of plagioclase (forming an anorthositic crust), followed by a concentration of KREEP materials in the last crystallization zones, presumably at the base of the Crust; The sinking of the Fe-Ti-rich layer crystallized in the mantle due to density instability, taking magnesian crystals to the upper part of the mantle; extrusion of molten materials (from the crust and the upper mantle), facilitated by the weakening of the crust due to meteoritical impacts.

Based on gamma-spectrometry data from the Lunar Prospector (NASA) mission, Jolliff et al. (2000) divided the crust and the lunar mantle into layers, where each one has distinct geochemical, geophysical, and geological characteristics. In the crust, the two largest terranes are the Procellarum KREEP Terrane (PKT) and the Feldspathic Highlands Terrane (FHT) (Figure 2.3). The FHT makes up about 60 % of the surface and mainly presents old rocks of anorthositic composition, with concentrations of Thorium (Th) that vary between 1 and 3 ppm. Basaltic flows in the FHT were formed during the Imbrian period and generally exhibit low to moderate concentrations of TiO_2 (<6 % wt). High concentrations of Th, from 3 to 12 ppm, and abundant basaltic lava flows characterize the PKT. The global balance calculations of Torium (Jaumann et al., 2012) indicated that approximately 30 % of the heat-producing elements may be located in the PKT, resulting in a greater flow of heat in this region. Compared to FHT rocks, PKT basalts are richer in FeO and TiO_2 and poor in Al_2O_3, containing more olivine and/or pyroxene, being considered a product of the layers formed in the Mantle during the early fractional crystallization of the Moon.

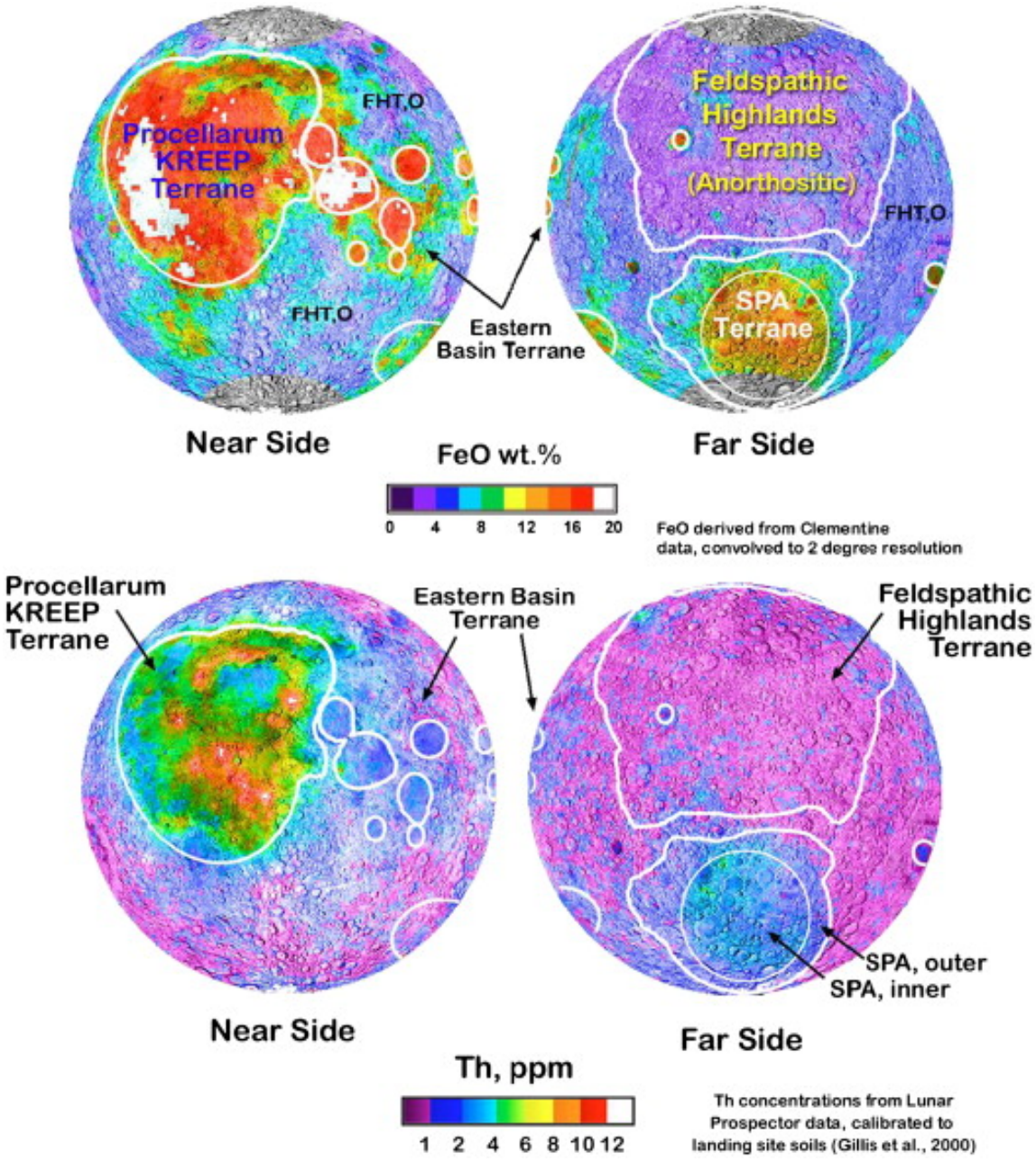

Figure 2.3 The two most extensive lunar terrains (Procellarum KREEP Terrane (PKT) and the Feldspathic Highlands Terrane (FHT)), inferred according to the distribution of FeO and Th. From Jaumann et al., 2012.

The Moon has no tectonic plates, unlike Earth, preserving evidence of its initial volcanic history (Jaumann et al., 2012). Basalts constitute approximately 30 % of the lunar surface on the side close to Earth and the warming due to the radioactive elements present in its composition resulted in partial melting of the material of the ultramafic mantle at depths between approximately 60 and 500 km in depth, generating a magma of basaltic composition (Hiesinger

and Head, 2006). The Moon is classified as a planetary body of a stagnant plate (Hiesinger and Head, 2006; Jaumann et al., 2012). The stagnant plate originates from the initial formation process of the Moon, from the solidification of the magma ocean, creating a crust with low density, due to the fractional crystallization steps (Figure 2.4). Due to slow convection, most of the Moon's internal heat was lost by conduction (Jaumann et al., 2012).

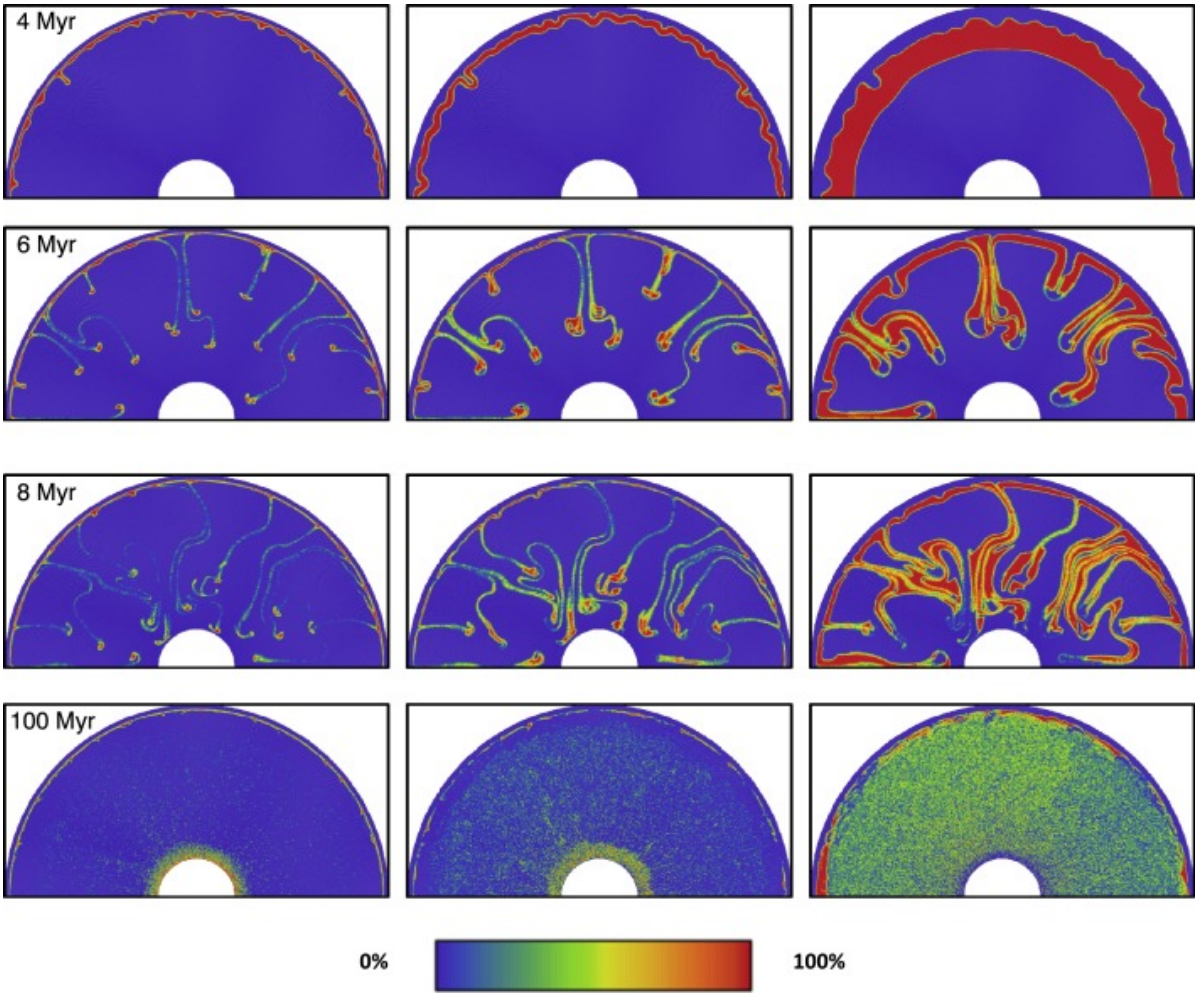

Figure 2.4 Two-dimensional sections of subsurface differentiation, as a function of time. The color scale shows the concentration of materials coming from the layer of ilmenite, rich in Fe-Ti. In 6 Myr, diapires from the layer reached the deepest mantle. After 100 Myr, the layer deposited at the bottom of the Mantle. From Zhao et al., 2019.

The knowledge about the cooling of the Moon made it scientifically accepted that there was no dynamic internal lunar activity, however, after the records of the moonquakes by the Apollo seismometers, it was verified that the Moon was still active, generating more interest in the scientific community in understanding its internal structure and selenodynamics (Jaumann et al., 2012). Internal structure models, using seismic velocity of P wave (Vp) and S wave (Vs) data of the Apollo missions and selenodetic data from Gravity Recovery and Interior Laboratory (GRAIL) and Lunar Laser Ranging (LLR) (all from NASA - For more information on the

missions, see Appendix II), they brought important information about the internal structure of the Moon (Kronrod et al., 2018; Hachay and Khachay, 2019; Mallik et al., 2019), where, currently, it is accepted that the Moon consists of nine layers: Megaregolith, crust, four-layer mantle, low viscosity zone (LVZ), fluid outer core and solid inner core (Figure 2.5). In each zone, the physical properties are considered to be constant (Kronrod et al., 2018).

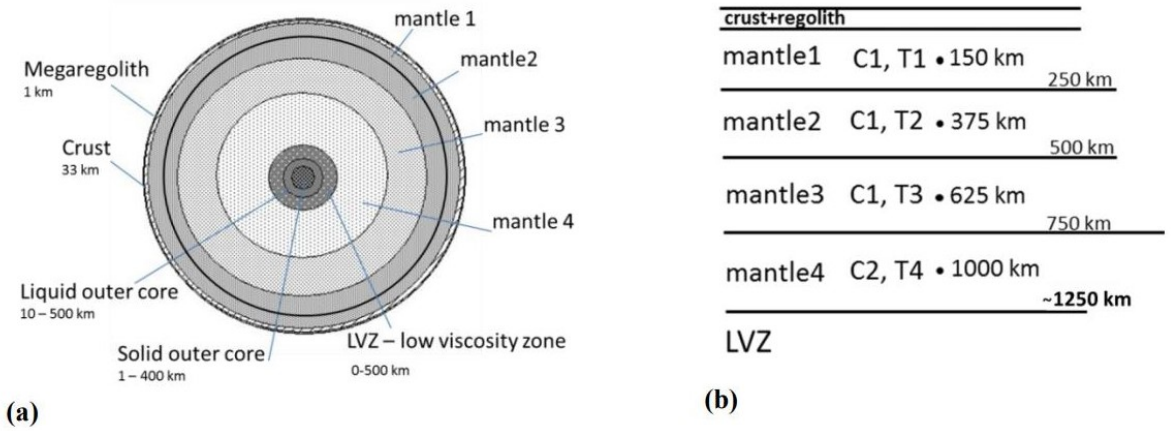

Figure 2.5 (a) Model of the internal structure of the Moon; (b) The structure of the mantle. The concentrations of temperature (T1-T4) and main oxides (Al_2O_3, FeO, MgO) (C1, C2) were specified according to the depth of the medium of each layer. From Kronhod et al., 2017.

Numerous studies on the chemical composition of the mantle are consistent about an olivine-pyroxene mixture (Lognonné et al., 2003; Zhao et al., 2012; Kronrod et al., 2018; Mallik et al., 2019; Zhao et al., 2019). The presence of Fe-Ti-rich minerals in the lunar mantle was stipulated as the cause of the differentiation, occurring in the formation process of the Moon, where the final crystallization of the magma ocean produced a layer rich in radioactive elements (KREEP) and a layer rich in ilmenite (Fe-Ti) below the low density crust, rich in plagioclase (Kronrod et al., 2018). The Fe-Ti-rich layer sank to deeper parts of the mantle due to its higher density and lower viscosity and if, in fact, the Moon has a Fe-rich core, that layer could have descended to the core-mantle boundary, where was subjected to heating by radioactive decay and rekindled, due to the range of thermal buoyancy. The resurgence provided sufficient heat for partial melting, producing the Maria basalts on the lunar subsurface (Mallik et al., 2019; Zhao et al., 2019) (Figure 2.6).

Apollo's seismic data record indicated that seismic velocities are approximately constant in the upper mantle and heterogeneously distributed in the middle mantle and the lower mantle. There is evidence of a seismic discontinuity in the middle mantle, around 560 km deep, which may indicate a change in the composition in this area (Lognonné et al., 2003; Gagnepain-Beyneix et al., 2006; Khan et al., 2006; Zhao et al., 2012; Kuskov et al., 2016). If this discontinuity is of global extent, it may reflect the initial melting depth during the magma ocean phase resulting from the initial differentiation of the Moon. If it is present only in the nearby hemisphere, it may represent the maximum melting depth of the region of origin of Maria basalts under the PKT (Kuskov and Fabrichnaya, 1994; Wieczorek and Phillips, 2000; Gagnepain-

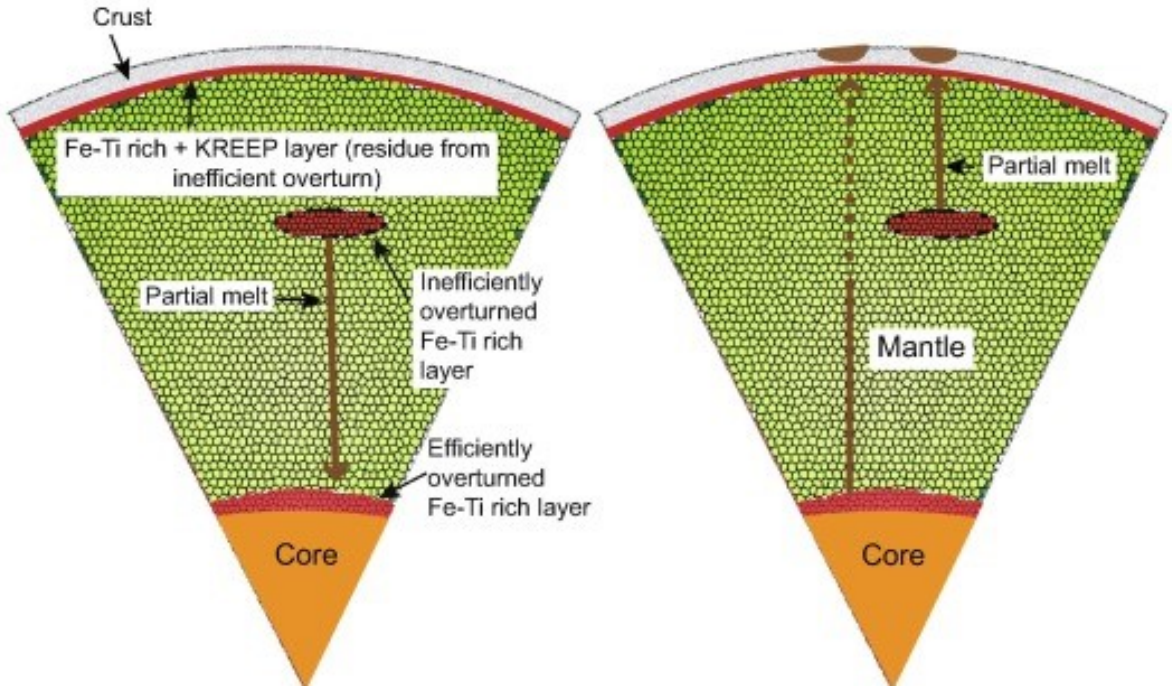

Figure 2.6 Schematic drawings that describe the two scenarios with respect to the partial melting of the Fe-Ti-rich layer and the surrounding lunar mantle. From Mallik et al., 2019.

Beyneix et al., 2006; Frohlich and Nakamura, 2009; Harada et al., 2014; Hao et al., 2018). In the lower mantle, at depths above 1150 km, seismic waves are strongly attenuated. This attenuation was interpreted as a partial melt zone that extends from 1150 km to the core-mantle boundary (CMB) (Nakamura, 2005; Gagnepain-Beyneix et al., 2006; Frohlich and Nakamura, 2009; Weber et al., 2010; Harada et al., 2014; Hao et al., 2018) (Figure 2.7).

The application of some seismological techniques by Weber et al. (2010) led to the identification of phases reflected in the lunar interior. The results were consistent with the existence of a partial melt layer in the lower mantle, a Fe-rich liquid outer core and a solid inner core (Figure 2.8). The registered deep moonquakes occurred in the so-called "nests", which are located at depths between 700 and 1100 km (Nakamura, 2005; Zhao et al., 2012; Jaumann et al., 2012; Hachay and Khachay, 2019). These nests repeatedly release seismic energy with specific observed cyclicality (Nakamura, 2008; Frohlich and Nakamura, 2009; Watters et al., 2019).

The lunar gravitational field also provides important information about the spatial distribution of mass on the surface and inside the Moon. There is a displacement of 1.9 km from the center of mass in relation to the center of the Moon towards the Earth, which is attributed to a pronounced dichotomy between the thickness of the nearby lateral crust and the distant hemisphere, established during the magma phase of the Moon.

The Moon is in synchronous rotation in relation to the Earth, that is, it is in a rotation coupling in 1:1 orbit. However, due to the orbital eccentricity (e = 0.0549) and the variation in the orbital angular velocity of the Moon along its elliptical trajectory, the exact timing is given only at two points in the orbit (Ascending nodes - Nodal Period). Near perigee, the angular

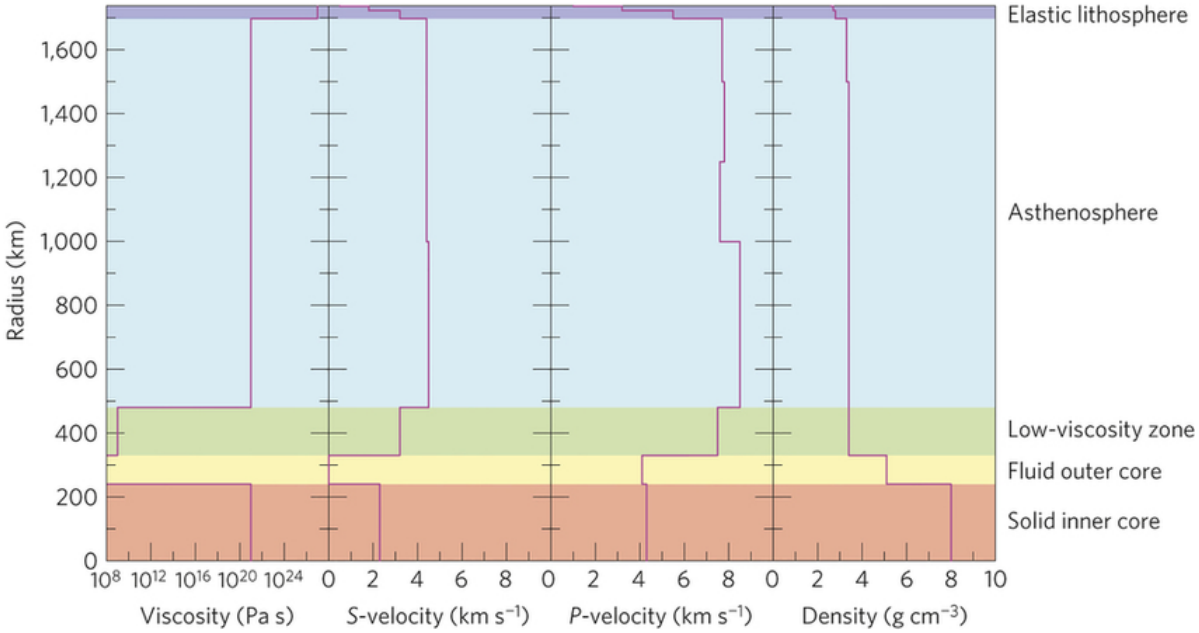

Figure 2.7 The low viscosity layer (green) corresponds to melting areas. Viscosity, velocity of P and S waves and density (purple lines) are plotted according to the lunar ray. From Harada et al., 2014.

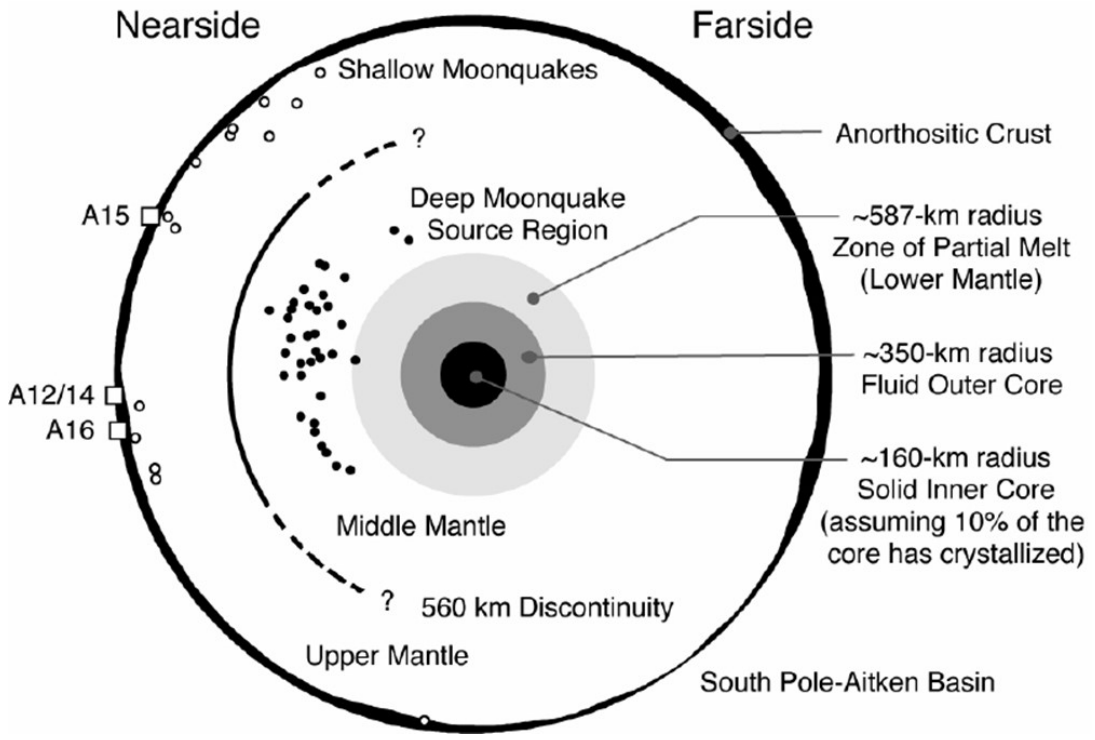

Figure 2.8 Cross section of the lunar structure, based on geophysical measurements. The projected hypocenters of moonquakes along the 0° meridian are shown. From Weber et al., 2019.

velocity of rotation is less than the orbital angular velocity, in the apogee this relationship is reversed. This relationship causes longitudinal librations (at about 8.6°). The inclination of the Moon's orbit (i = 5.15°) in relation to the ecliptic plane causes latitudinal librations (about 6.9°). The librations generate tidal forces essential for the dissipation of orbital energy on the Moon, which tends to decrease the orbital eccentricity (e) and the semi-major axis (a), while the tidal torques, exerted by the Earth, tend increasing the orbital eccentricity of the Moon and the semi-major axis. Although lunar tides contribute only 1 % to the Moon's orbital acceleration, they significantly contribute to changes in the rate of dissipation (Frohlich and Nakamura, 2009; Williams et al., 2017), so orbital evolution is closely linked to thermal state of the lunar interior and the selenodynamo. The presence of the partial melt zone in the lunar interior, then, is directly linked to the rate of dissipation, elasticity and thickness of the mantle, composition and physical state of the core (Kuskov and Kronrod, 1998; Lognonné et al., 2003; Zhao et al., 2012; Harada et al., 2014; Kronrod et al., 2018; Hao et al., 2018; Watters et al., 2019).

2.4 Lunar terranes

The lunar crust and underlying mantle are distinct terranes that possess unique geochemical, geophysical, and geological characteristics. The two most extensive terranes are the Procellarum KREEP Terrane (PKT) and the Feldspathic Highlands Terrane (FHT) (Jaumann et al., 2012)(Figure 2.9). The Feldspathic Highlands Terrane covers 60% of the Moon's surface area and is composed primarily of ancient anorthositic rocks, presumed to be mainly of the ferroan anorthositic suite. This terrane is characterized by crustal Th concentrations that range from less than 1 to 2–3 ppm. Basaltic flows in this terrane made a volumetrically small contribution, and generally exhibit low to moderate concentrations of TiO_2 ($\geq$6 wt%). High Th concentrations of 3–12 ppm and a high abundance of mare basaltic lava flows that erupted from at least 4.2 Ga to about 1 Ga characterize the Procellarum KREEP Terrane in the Oceanus Procellarum and Mare Imbrium regions. The high abundances of heat-producing elements within the Procellarum KREEP Terrane are likely the cause of extensive magmatic productivity and volcanic longevity within this region. Global Th mass-balance calculations indicate that 30% of the Moon's heat-producing elements may be located within the Procellarum KREEP Terrane (Jolliff et al., 2000), resulting in an increased heat flow and enhanced rates of viscous relaxation of basins within this terrane (Jaumann et al., 2012).

2.5 Basic concepts of celestial mechanics

In studies of astronomy and celestial mechanics, an "epoch" is a moment used as a reference point for coordinates of celestial bodies or time-varying orbital elements, where astronomical quantities are generally specified as a polynomial as a function of time, being a given epoch the time point of origin ($t0$) of the system, that is, the values obtained for the coordinates of a given celestial body in an interval t after the selected epoch is equal to $f(epoch+t)$.

The celestial coordinate systems most used are the equatorial and ecliptic coordinates. They

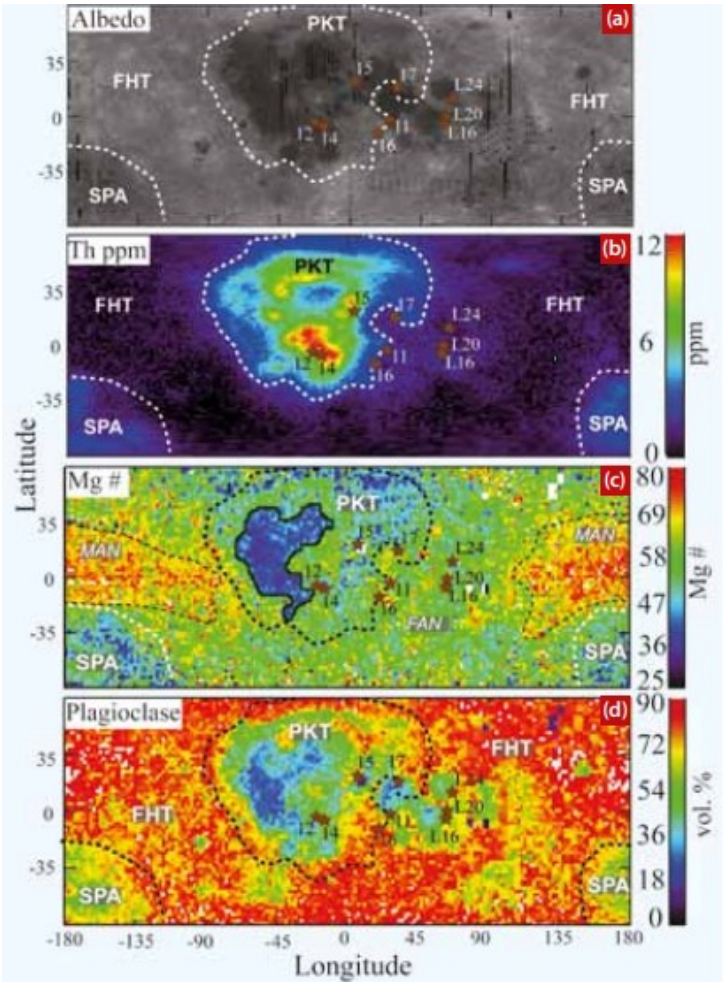

Figure 2.9 Lunar terranes with different compositions and albedo. From Pernet-Fisher et al., 2019.

are defined in relation to the position of the Earth's axis of rotation and the orbit around the Sun. The reference to an equinox or the equator/ecliptic of a given moment t addresses changes in the coordinate system of the astronomical variables, expressed in terms of terrestrial time, with an equivalent Julian Day.

As the Moon is relatively close to the Earth and is kept in orbit by the gravitational attraction, its orbit resembles an ellipse, with the Earth in one of the foci, however, its real orbit changes over time, due to gravitational disturbances exerted by the Sun, by other celestial bodies, and due to the effects of relativity.

According to celestial mechanics studies (Szebehely, 1967), at least six parameters are needed to describe the movement of a body around the Earth (Figure 2.10), as it has six degrees of freedom, being three dimensions corresponding to the position (x, y, z) and three defined by the velocity in each of the dimensions. Two of these define the shape of the ellipse:

- Eccentricity (e) - the shape of the ellipse, describing how much it is elongated compared to a circle (dimensionless parameter).

- Semi-major axis (a) - in classic orbits of two elements, it is the distance between the

centers of the bodies (in km).

Two define the orientation of the orbit plane:

- Inclination (i) - the vertical inclination of the ellipse in relation to the plane of the ascending node, that is, the inclination between the orbital and the ecliptic plane (in degrees).

- Longitude of Ascending node (Ω) - horizontal orientation of the ascending node in the ellipse in relation to the vernal point (Υ). Indicates the angle between the vernal equinox and the point of the orbit where the satellite crosses the ecliptic from south to north (in degrees).

Two define the orientation of the body:

- Argument of Periapsis (ω) - orientation of the ellipse in the orbital plane, as a measured angle from the ascending node to Periapsia (Periapsia is the point at which the Moon comes closest to Earth) (in degrees). NOTE: Apoapsis and Periapsis are “generic” terms for any celestial body. When orbiting the Earth (as in the case of the Moon), the two terms are known as Apogee and Perigee.

- True anomaly (υ) - defines the position of the body in orbit along the ellipse (in degrees).

Other secondary elements are independent of any particular coordinate system: "M", the mean anomaly (in degrees), and "n", the average daily movement (degrees/day). The “a” and “e” parameters are also independent. But the argument of Periapsis, the length of the ascending node, and the inclination of the orbital plane are all dependent on coordinates and the reference structure of the equinox/ecliptic of the chosen time. The mean anomaly (M) is an angle that varies linearly with time but does not correspond to a real geometric angle. From it, one can find the real angle in the plane of the ellipse, the true anomaly (υ), between the Periapsis and the position of the Moon. The angles of inclination, length of the ascending node, and argument of Periapsis also can be described as “Euler angles”, which define the orientation of the orbit in relation to the referential coordinate system.

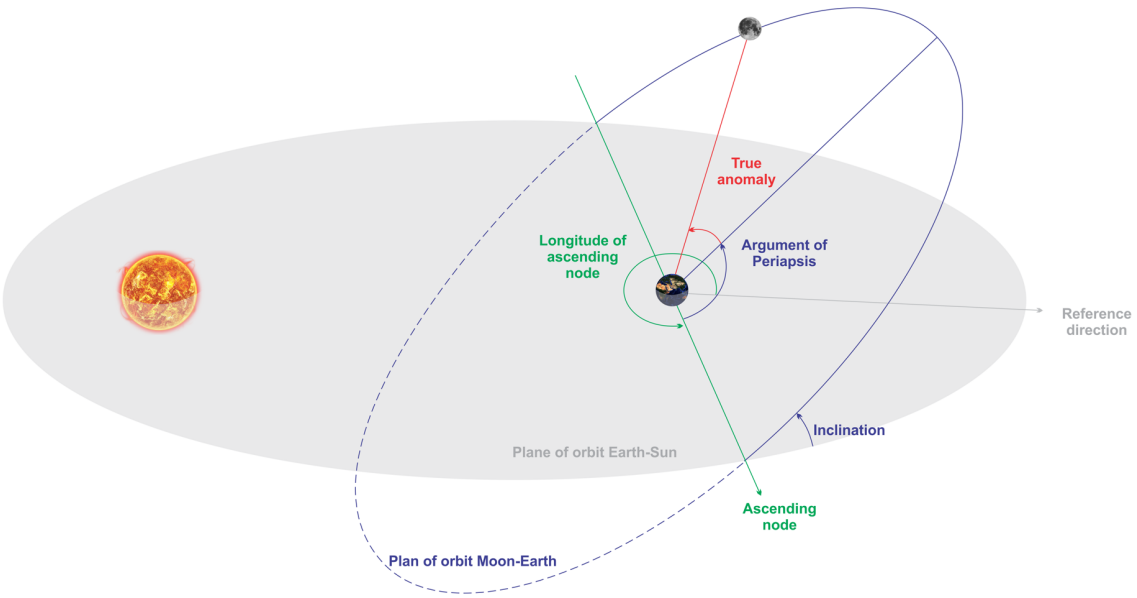

Figure 2.10 Angular relationships between basic orbital parameters.

CHAPTER 3

Materials and methods

The used data were the records of deep moonquakes and deep earthquakes, as well as the calculation of orbital parameters of the Earth-Moon-Sun system for the same period of the occurrence of the deep quakes. Pre-processing involved statistical studies and trending/stationarity removal from the data. Processing involved several methods, including wavelets, machine learning and spectrogram.

3.1 Data

For the development of the research, two types of data were used: The records of seismological events recorded between 1970 and 1977, by the Apollo missions (NASA), and the calculations of orbital parameters of the Moon-Earth-Sun system for the same time of the seismograms.

Apollo missions recorded moonquakes at different periods between some stations, Apollo 11 (between 7/21/1969 and 8/3/1969, between 8/19/1969 and 8/26/1969), Apollo 12 (between 11/19/1969 and 09/30/1977), Apollo 14 (between 02/05/1971 and 09/30/1977), Apollo 15 (between 07/31/1971 and 09/30/1977), Apollo 16 (between 21/04/1972 and 09/30/1977) and Apollo 17 (between 03/01/1976 and 09/30/1977). Apollo 11 consists of non-continuous data (in relation to the registration period of the other stations), generating a gap in the deep moonquakes time series. For this reason, these data were not used. The data from the Apollo Seismographic Network are available in the "Technical Reports On Lunar Data", in the NASA directory, under constant review by Dr. Yosio Nakamura (Nakamura, 2008). To view the seismograms and make the seismic catalog, the "Moon Seismic Monitor" was used, an online software from JAXA (Japan Aerospace Exploration Agency), available at *'https://www.darts.isas.jaxa.jp/planet/seismology/apollo/app/'*. The Moon Seismic Monitor shows characteristics of each event, such as latitude and longitude of the epicenters and depth of the hypocenters, as well as their classification (shallow, deep, thermal, etc) (Figure 3.1). This information in the JAXA directory was used to produce the lunar seismic catalog (totaling 13,055 events in all).

In possession of the lunar seismic catalog, only events classified as "deep" were used, discarding all others. Due to the non-continuous nature of registration in 1969, the use of data from 01/01/1970 to 09/30/1977 (last recorded day of stations) was limited. So, in summary, the deep moonquakes time series consists of counting events classified as "deep" per day, for a total of 2830 days. For the discussion of results and validation, a time series of deep earthquakes per day was also carried out during the same period. To make the earthquakes series, the "Wilber 3", Tool from IRIS (Incorporated Research Institutions for Seismology) was used, available at

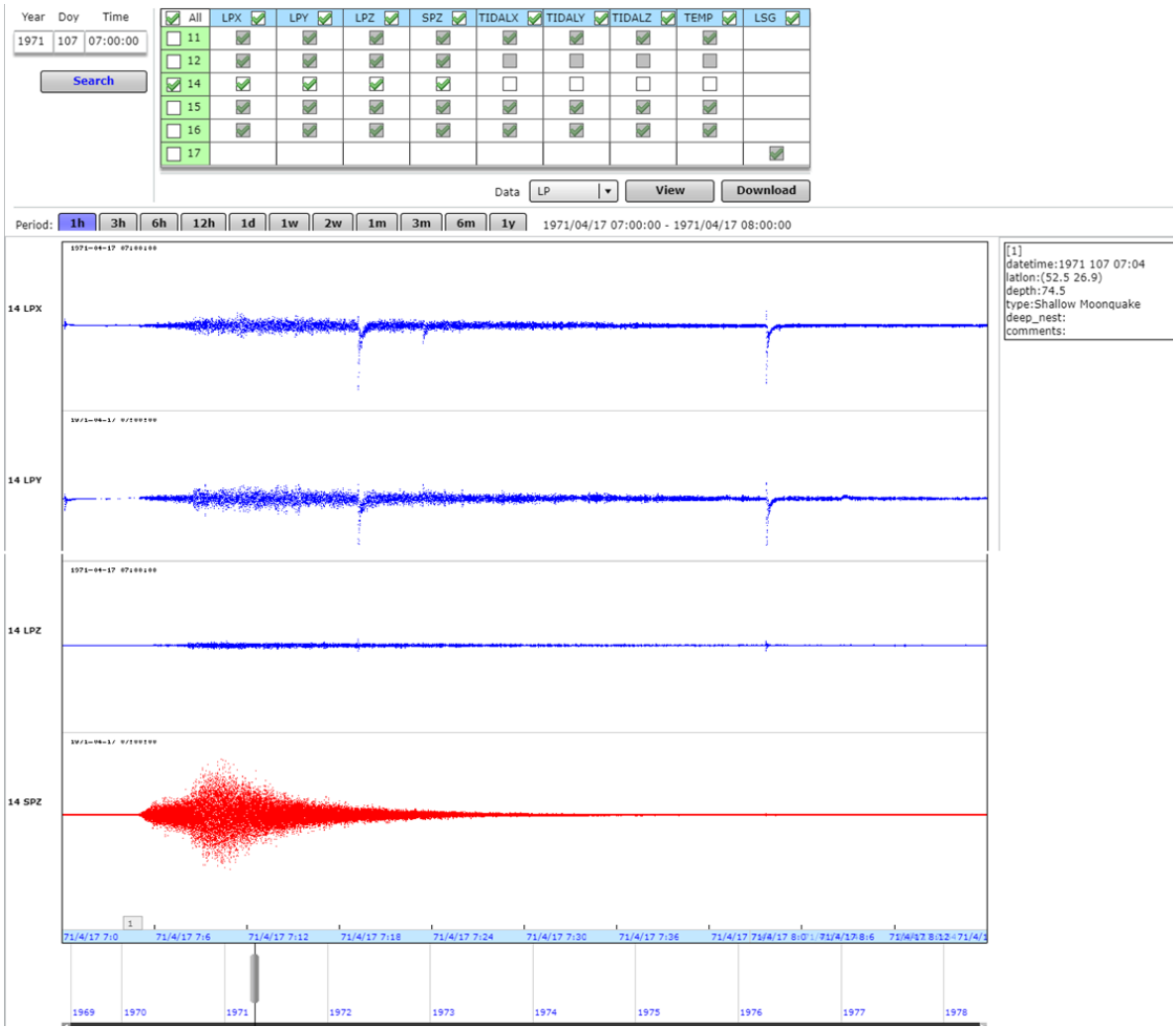

Figure 3.1 Example of data in the Moon Seismic Monitor (JAXA), where it is possible to choose components, station, date, and also have information such as hypocenter depth, latitude, longitude, and moonquake type.

$'http://ds.iris.edu/wilber3/find\_event'$.

The orbital parameters of the Moon-Earth-Sun system were calculated using the HORIZONS software, used by NASA to calculate the orbits of the space agency's manned and unmanned missions (including sending satellites). The software is free, but closed, requiring a limited use request by the user. For the calculation, the following configurations were used:

- Target Body: Moon [Luna] [código 301],
- Mass Center: Earth-Moon Barycenter [código 500@3],
- Time Span: Start = 1970-01-01, Stop = 1977-09-29, Step = 1 day,
- Table Settings: output units = KM-S; TP type = RELATIVE.

Each orbital parameter (A, AD, EC, IN, JD, MA, N, OM, PR, QR, TA, Tp, W) was arranged

in a time series separately, composed of the value calculated in the respective units of each parameter per day, in a total of 2830 days. What are each of the parameters used for the calculated ones is set out in Appendix III.

3.2 Pre-processing

A time series is a set of ordered observations, which are dependent on time. An analysis of a time series is performed to understand the causal mechanism of the series or of one or more parameters. Understanding the mechanism of the series makes it possible to find periodicities and obtain reasons for their behavior. The analysis of time series implies that there is an approximately constant causal mechanism, related to time, which exerted an influence on the data creating non-random patterns detectable by some statistical process. According to the classic model, time series is composed of four patterns: (i) trend, long-term behavior of the series; (ii) cycles, bias fluctuations in the values of the variable lasting more than one year and which are repeated with certain periodicity; (iii) seasonality, tendentious fluctuations in the values of the variable lasting less than one year and which are repeated annually; (iv) irregular variations, unexplained fluctuations resulting from unexpected facts. It is important to note that, although the analysis of the series is taking into account all the classic patterns, it will not always present all the components.

The models used to describe time series are stochastic processes, that is, controlled by probabilistic laws. A time series is said to be stationary when it develops in time around a constant average, reflecting some form of stable equilibrium. Most time series show some kind of non-stationarity, as a trend. So, it is important to check in the first instance whether or not all series have a stationary character, analyzing whether there is any unit root and whether they have a trend. Below are the analysis results for the series of orbital parameters and for the series of deep moonquakes (Figure 3.2). The analysis was carried out using the Action Stat software.

	Trend Test				Stationary Test			
Time series	Statistic	P-Value	Significance Level	Conclusion	Statistic	P-Value	Significance Level	Conclusion
A	0.0029	0.8191	0.05	Trend Not Detected	-304.4468	0.0100	0.05	Stationary
AD	-0.0147	0.2408	0.05	Trend Not Detected	-46.4101	0.0100	0.05	Stationary
EC	-0.0175	0.1635	0.05	Trend Not Detected	-44.4712	0.0100	0.05	Stationary
IN	-0.0239	0.0568	0.05	Trend Not Detected	-9.2199	0.0100	0.05	Stationary
JD	1.0000	0.0000	0.05	Trend Detected	1.7321	0.9900	0.05	Non Stationary
MA	0.0020	0.8733	0.05	Trend Not Detected	-18.9363	0.0100	0.05	Stationary
N	-0.0029	0.8191	0.05	Trend Not Detected	-307.3832	0.0100	0.05	Stationary
OM	-0.9967	0.0000	0.05	Trend Detected	-9.1975	0.0100	0.05	Stationary
TA	0.0019	0.8774	0.05	Trend Not Detected	-19.4637	0.0100	0.05	Stationary
Tp	-0.0020	0.8723	0.05	Trend Not Detected	-18.1695	0.0100	0.05	Stationary
W	0.2236	0.0000	0.05	Trend Detected	-7.9675	0.0100	0.05	Stationary
Deep Moon	0.0293	0.0294	0.05	Trend Detected	-21.3979	0.0100	0.05	Stationary

Figure 3.2 Results and conclusions of stationary and trend tests of the time series.

The p-value of the Mann-Kendall test (trend test) is 0.0294. Therefore, the null hypothesis will be rejected (the series' observations are independent and identically distributed) at the

significance level of 0.05. Therefore, concluding that there is a significant trend if the statistic is less than 0.0294. The p-value of the Dickey-Fuller test (stationarity test) is 0.01. Therefore, the null hypothesis will be rejected (there is at least one root within the unit circle) at the significance level of 0.05. Therefore, concluding that the data is stationary if the statistic is less than 0.01.

It was possible to verify that all parameters, except JD (Julian Day), are stationary, implying that (in a way, expected) the orbital parameters and the deep moonquakes reflect an occurrence with stable equilibrium, with its cyclicality oscillating around their average in a relatively orderly manner. The JD parameter has a non-stationary nature, since it is a count of days, with no fixed average over an infinite period or changing the analyzed period. The trend in the series of parameters JD, OM, W, and that of deep moonquakes is linked to a change in the medium or long level. In other words, the trend reflects the decline/increase in the average value of the long-term time series.

Thus, before processing the data, the trend of the JD series (Figure 3.3), OM (Figure 3.4), W (Figure 3.5), and Deep Moonquakes (Figure 3.6), and the non-stationarity of the JD series (Figure 3.3) were removed, in order that all series had the same behavioral pattern, not interfering erroneously in the processing, in the final model, and in its interpretation.

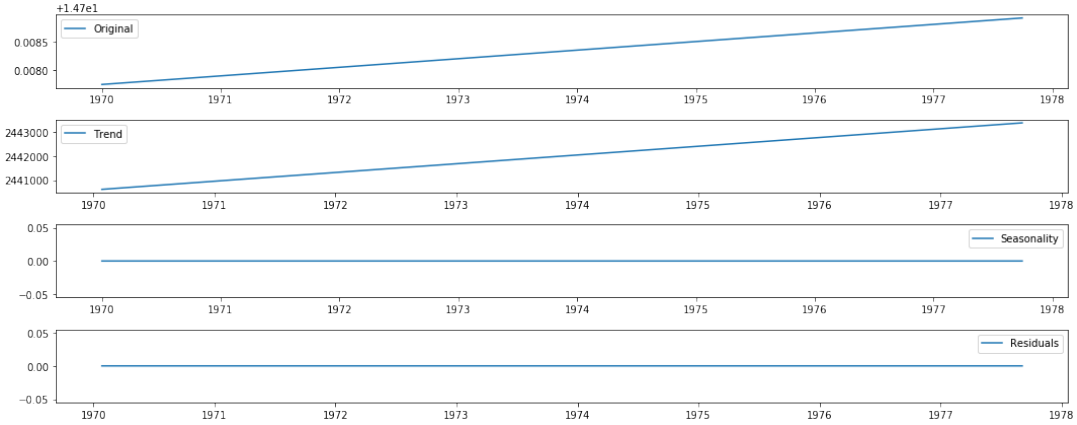

Figure 3.3 JD's original time series and its patterns: trend, seasonality, and residual.

For a complete understanding of the data, a simple statistical study of all series was also carried out, on distribution, mean, variance, maximum, and minimum values (Figure 3.7). In Python, graphs of each series were plotted, related to the number of daily events (for example, Figure 3.8). The x-axis of the graphs corresponds to the Julian Day (date), the y-axis corresponds to the value of the time series parameter and the colors correspond to the number of moonquakes recorded on the same time. It is possible to perceive in a good part of the graphs (Attachment I), as, for example, in the graph of the parameter W (Figure 3.8), that specific periods (middle of 1971 (approx. 2440750 JD) and middle of 1977 (approx. 2443250 JD)) have a higher count of daily moonquakes (higher concentration of green balls). All graphs, from all series, are in Attachment I.

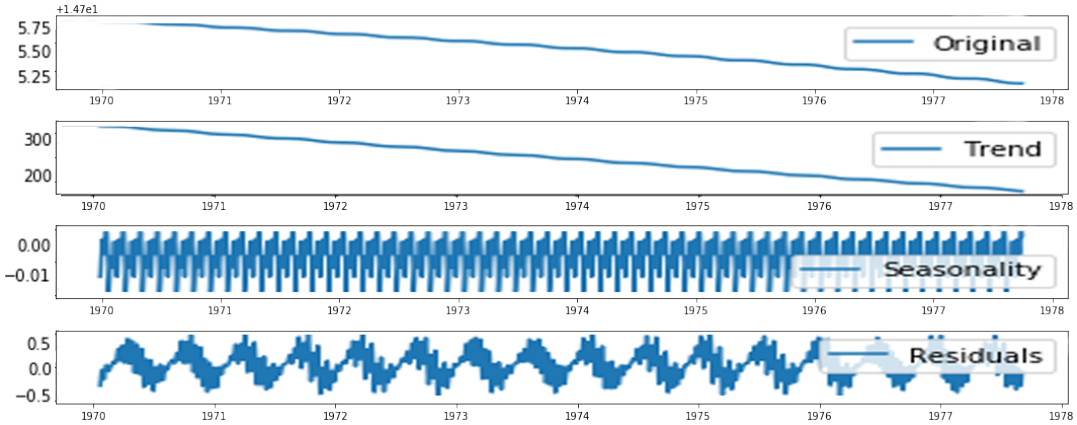

Figure 3.4 OM's original time series and its patterns: trend, seasonality, and residual.

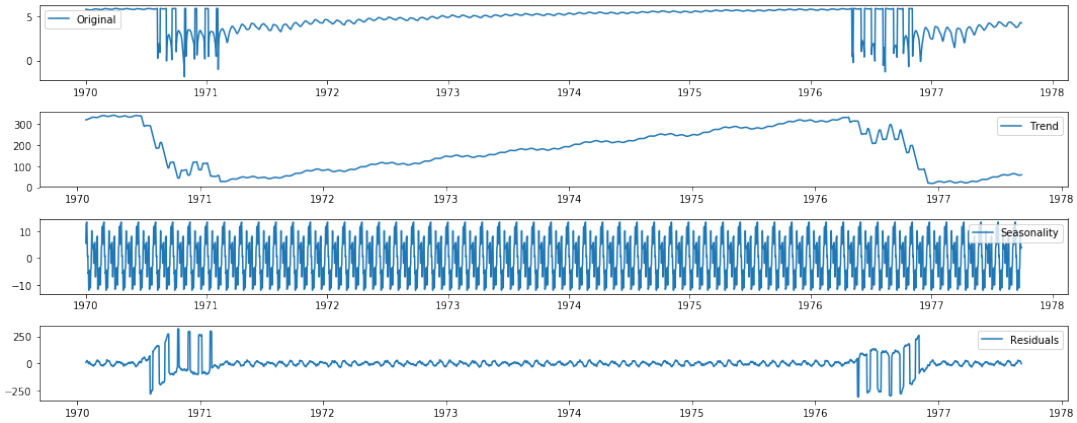

Figure 3.5 W's original time series and its patterns: trend, seasonality, and residual.

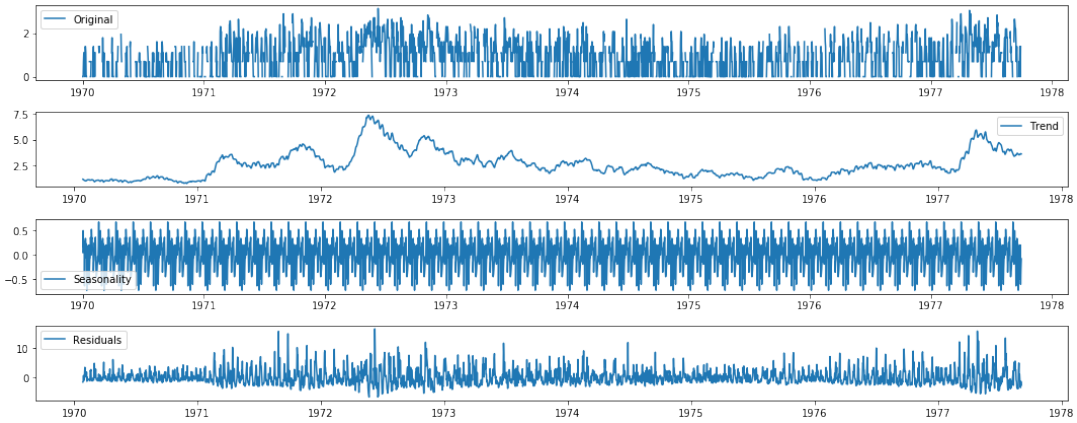

Figure 3.6 Deep moonquake's original time series and its patterns: trend, seasonality, and residual.

.

	count	mean	std	min	25%	50%	75%	max
A	2830.0	3.787413e+05	2428.699208	3.749575e+05	3.763307e+05	3.787089e+05	3.810852e+05	3.829804e+05
AD	2830.0	3.997613e+05	4771.714248	3.852137e+05	3.981988e+05	4.002755e+05	4.016115e+05	4.109567e+05
EC	2830.0	5.551316e-02	0.011929	2.586736e-02	4.690720e-02	5.670815e-02	6.552211e-02	7.700539e-02
IN	2830.0	5.158821e+00	0.096196	4.991971e+00	5.066094e+00	5.162072e+00	5.254120e+00	5.301351e+00
JD	2830.0	2.442002e+06	817.094956	2.440588e+06	2.441295e+06	2.442002e+06	2.442709e+06	2.443416e+06
MA	2830.0	1.802970e+02	101.807833	5.243799e-02	9.422224e+01	1.807975e+02	2.665800e+02	3.599662e+02
N	2830.0	1.533210e-04	0.000001	1.507709e-04	1.518970e-04	1.533289e-04	1.547846e-04	1.556357e-04
OM	2830.0	2.707318e+02	43.306813	1.955353e+02	2.322348e+02	2.694854e+02	3.069577e+02	3.444857e+02
PR	2830.0	2.348232e+06	22588.468115	2.313094e+06	2.325812e+06	2.347894e+06	2.370028e+06	2.387729e+06
QR	2830.0	3.577214e+05	5419.292782	3.485598e+05	3.526720e+05	3.572800e+05	3.629808e+05	3.671569e+05
TA	2830.0	1.802994e+02	98.314384	6.067308e-02	1.004142e+02	1.807117e+02	2.602647e+02	3.599605e+02
Tp	2830.0	3.095946e+03	691420.830406	-1.188695e+06	-6.029697e+05	3.349803e+03	6.156857e+05	1.184886e+06
W	2830.0	1.751517e+02	116.638481	1.622741e-01	6.141166e+01	1.688907e+02	2.877936e+02	3.599620e+02
Deep	2830.0	2.595053e+00	2.925487	0.000000e+00	0.000000e+00	2.000000e+00	4.000000e+00	2.300000e+01

Figure 3.7 Statistics of the time series.

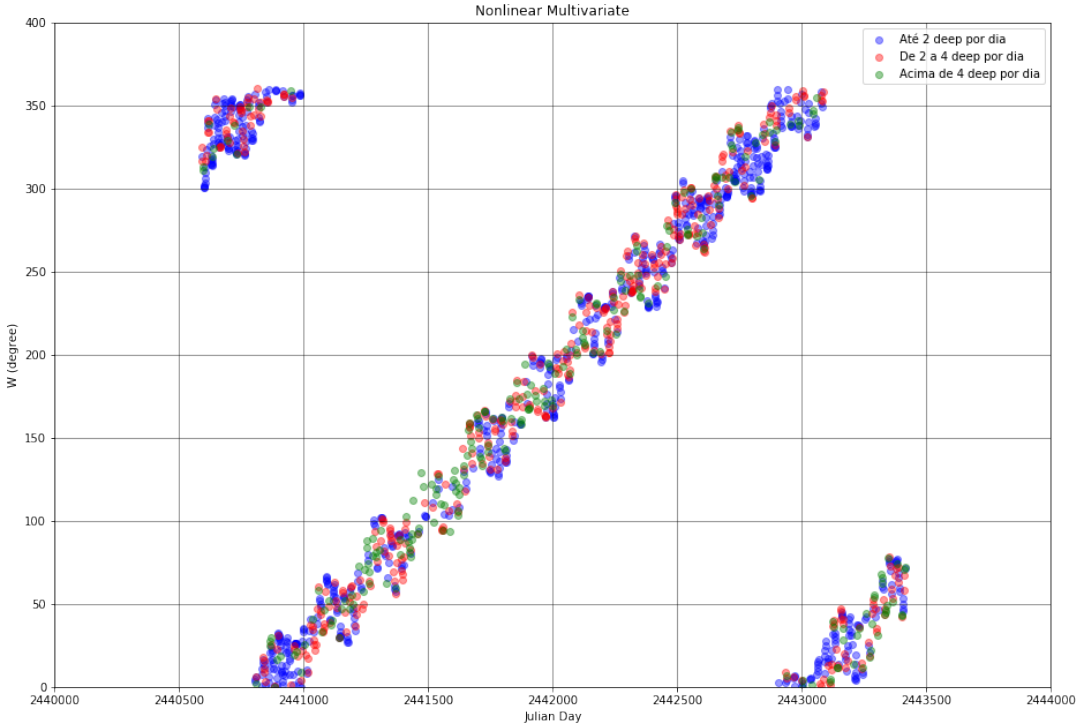

Figure 3.8 Graph relating the parameter W to the number of daily deep moonquakes. The x-axis corresponds to the Julian Day (date), the y-axis corresponds to the value of the W time series by day and the colors correspond to the number of deep moonquakes recorded on the same day. In blue, until 2 deep moonquakes per day, in red between 2 and 4, and in green, more than 4 events per day.

3.3 Data processing

First, the study of time series, with a focus on cyclicity, took place through the analysis of the Wavelet Transform (WT). As said in Appendix VI, WT allows decomposing the frequencies that compose a signal, to understand patterns and higher concentrations of energy. In the graphs (Figure 3.9 to 3.14), the dark blue regions show frequencies equal to 0 and the yellow regions have the maximum frequencies of the signal.

It is possible to observe that the wavelets of the series of parameters A (Figure 3.9a), N (Figure 3.9b), and PR (Figure 3.9c), have the frequencies concentrated in the periods of approximately 15 days (0.0438 yr) and approximately 1 month (0.8333 yr). This indicates that they are of a continuous biweekly/monthly nature.

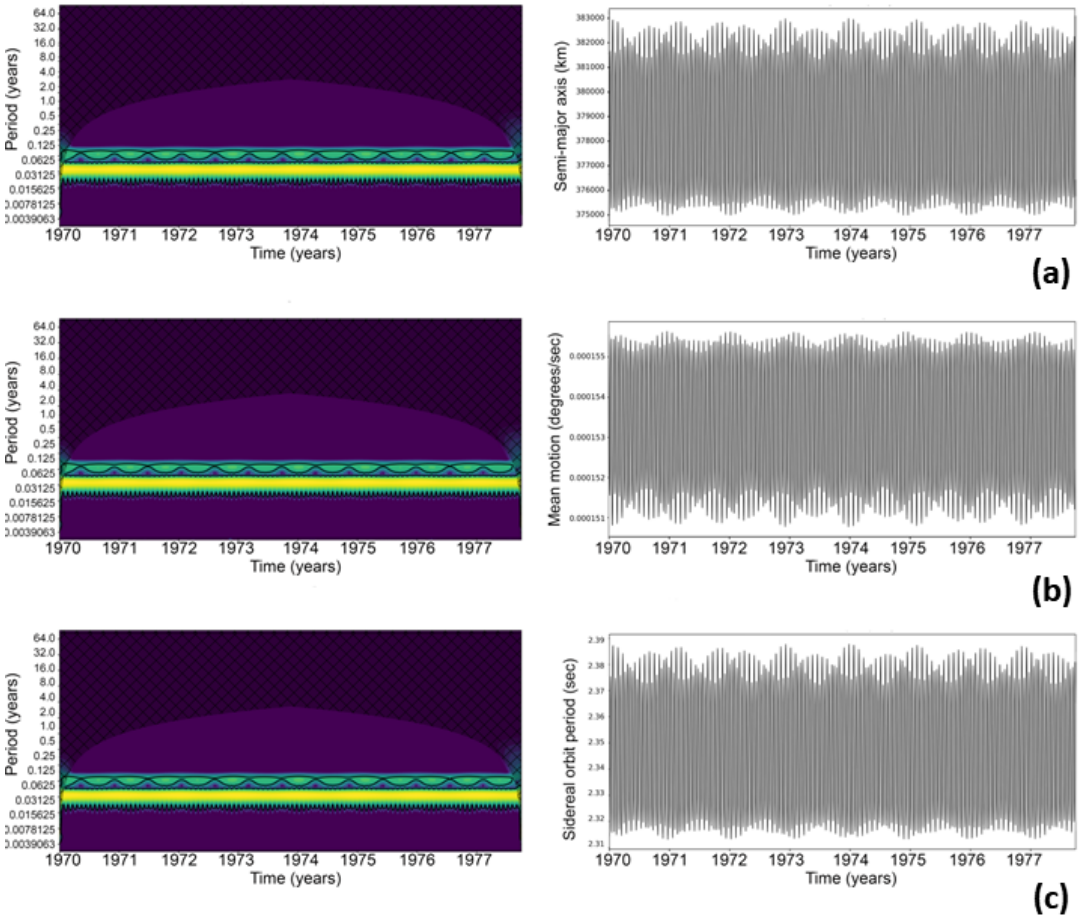

Figure 3.9 (a) Wavelet of the orbital parameter A (left) and the graph of the time series (right). (b) Wavelet of the orbital parameter N and the graph of the time series. (c) Wavelet of the orbital parameter PR and the graph of the time series.

The parameters AD (Figure 3.10a), EC (Figure 3.10b), and QR (Figure 3.10c) have signal frequencies concentrated in the periods of approximately 10 days (0.0273 yr), approximately 15 days (0.0438 yr), approximately 1 month (0.8333 yr) and 0.5 years. Indicating continuous occurrence every 1.5 weeks and fortnightly.

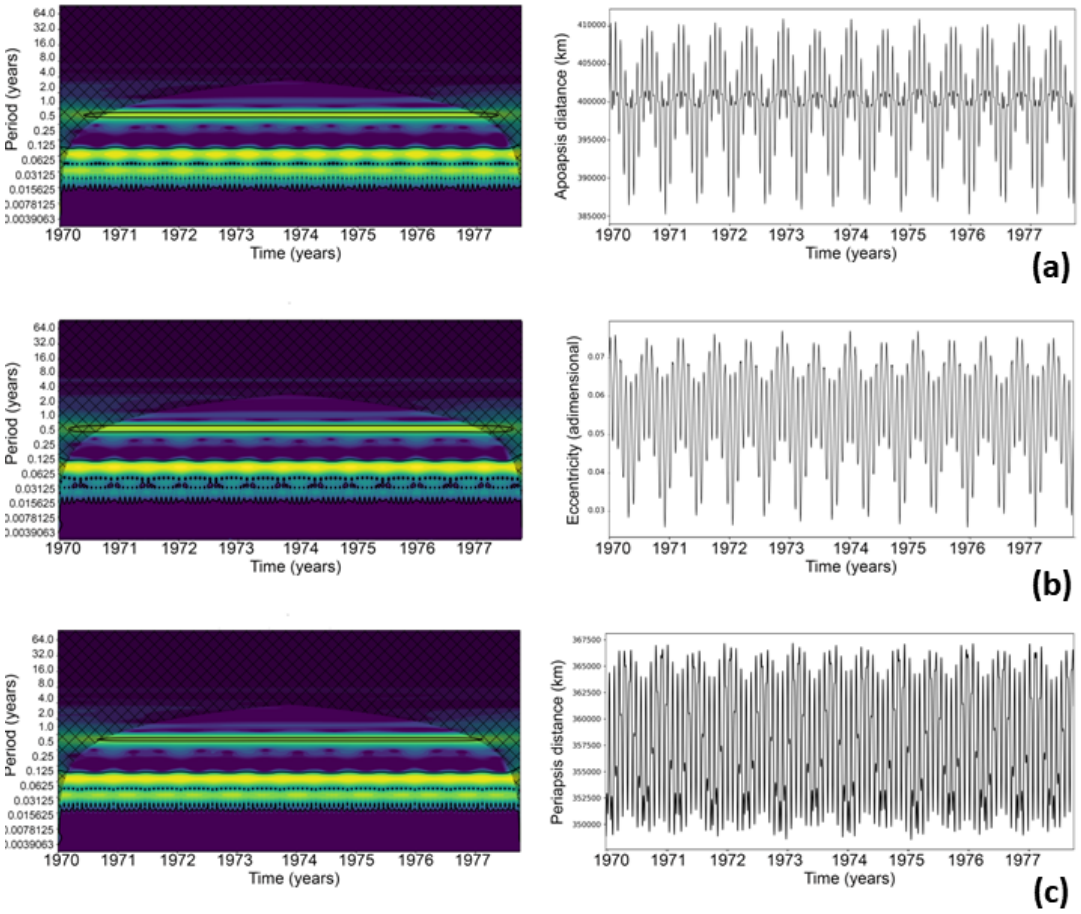

Figure 3.10 (a) Wavelet of the orbital parameter AD (left) and the graph of the time series (right). (b) Wavelet of the orbital parameter EC and the graph of the time series. (c) Wavelet of the orbital parameter QR and the graph of the time series.

In the parameters IN (Figure 3.11a) and OM (Figure 3.11b), the frequency of the signal is concentrated in the periods of approximately 15 days and 0.5 years.

The parameters MA (Figure 3.12a), TA (Figure 3.12b), and Tp (Figure 3.12c), have signal frequencies concentrated in the periods of approximately 1 day (0.0039 yr) to approximately 1.5 months (0.125 yr).

Finally, the W parameter (Figure 3.13a) has the signal frequencies concentrated in the periods from approximately 1 day (0.0039 yr) to approximately 1.5 months (0.125 yr), in specific years (1970/1971 - 1976/1977).

The series of deep moonquakes (Figure 3.14) and deep earthquakes (Figure 3.14) have signal frequencies combined in daily, weekly, biweekly, monthly and annual periods. Comparing

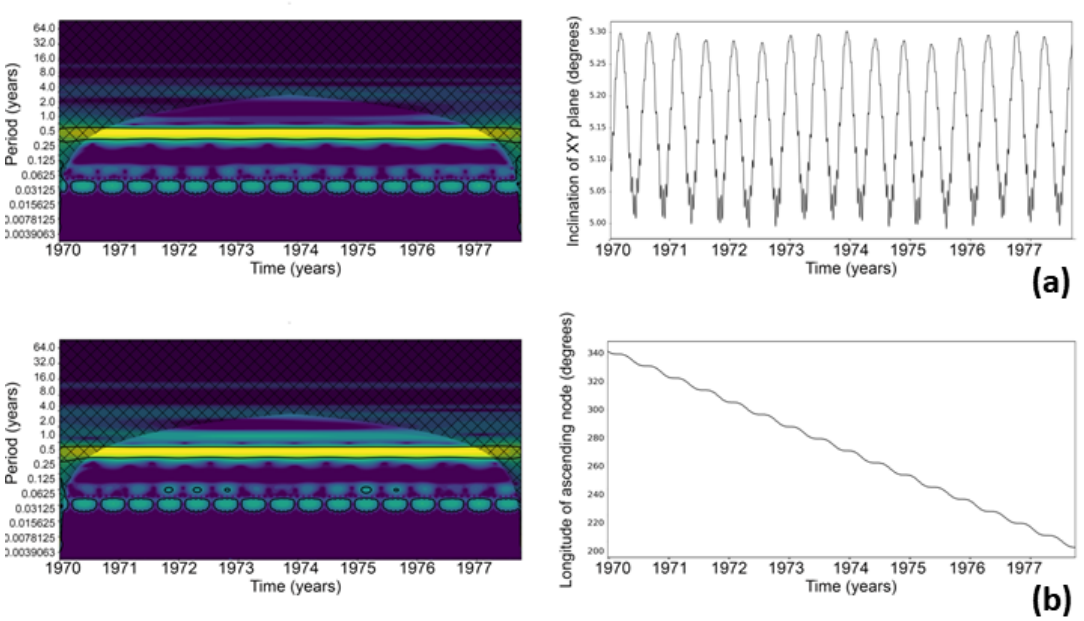

Figure 3.11 (a) Wavelet of the orbital parameter IN (left) and the graph of the time series (right). (b) Wavelet of the orbital parameter OM and the graph of the time series.

both wavelets, it is possible to see that the two have similar spikes in frequencies (count of quakes per day), in similar periods (middle of 1971 and middle of 1977), and with similar behavior (Figure 3.14).

Using the same two series, Wavelet Coherence (WC) analysis was performed. As said in Appendix VI, the WC allows detecting similarities between two parameters in terms of time-scale, extracting causal relationships between two series, analyzing how their respective occurrences are correlated over time, where the null correlation is equal to 0 (blue on the color scale) and the total correlation is equal to 1 (red). It is possible to observe in the WC graph (Figure 3.15) that the time series of deep moonquakes and deep earthquakes are correlated in periods of days, months, and years, but the greatest correlations occur in periods of up to 31 days and total correlations occur in approximately 8 and 18 days.

The analysis by WC was intended to correlate the forces acting with the events, in order to delimit the periods of greatest influence in the deep moonquakes, since their occurrence is cyclical, as well as the orbital periods that interfere in the gravitational forces acting in the system.

Being aware that deep moonquakes and deep earthquakes are correlated, all series (including orbital parameters again) were grouped in a single database, normalized (due to their different physical quantities, such as km, km/sec, sec, degrees, degrees/sec, etc) and analyzed using machine learning (ML), in the Weka software (Witten et al., 2016), in order to detect which orbital relationships influence the occurrence of quakes. All possible ML models for numerical data were used and the results are shown below (Figure 3.16).

In figure 3.16, the best results are written in green. The closer the coefficient correlation to

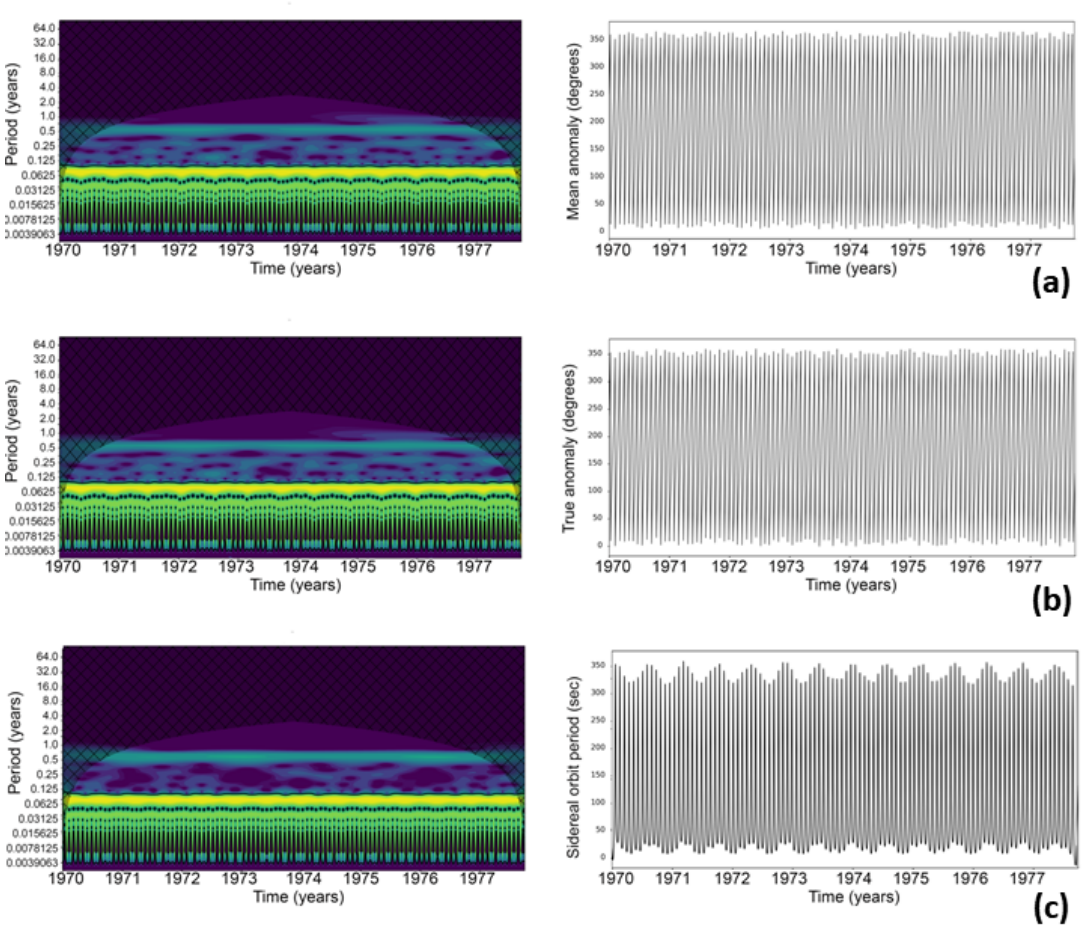

Figure 3.12 (a) Wavelet of the orbital parameter MA (left) and the graph of the time series (right). (b) Wavelet of the orbital parameter TA and the graph of the time series. (c) Wavelet of the orbital parameter Tp and the graph of the time series.

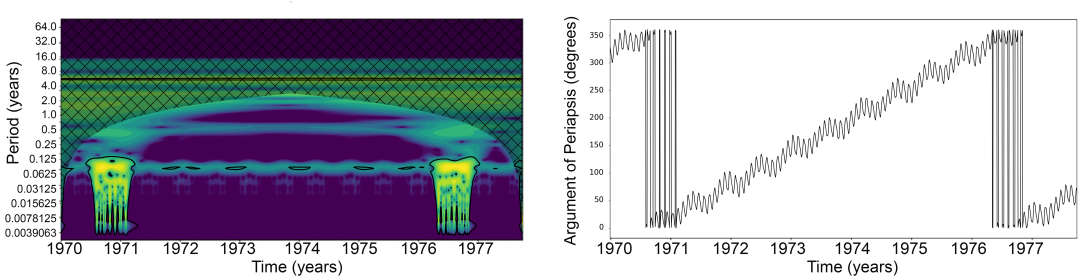

Figure 3.13 Wavelet of the orbital parameter W (left) and the graph of the time series (right).

“1.0” and the closer to “0.0” the errors, better the adequacy of the model. The best ones were the Random Committee and the Random Tree, both models are of the "Decision Tree” style and indicated the W as the “main branch/mother”. Random Tree had 11921 total branches and

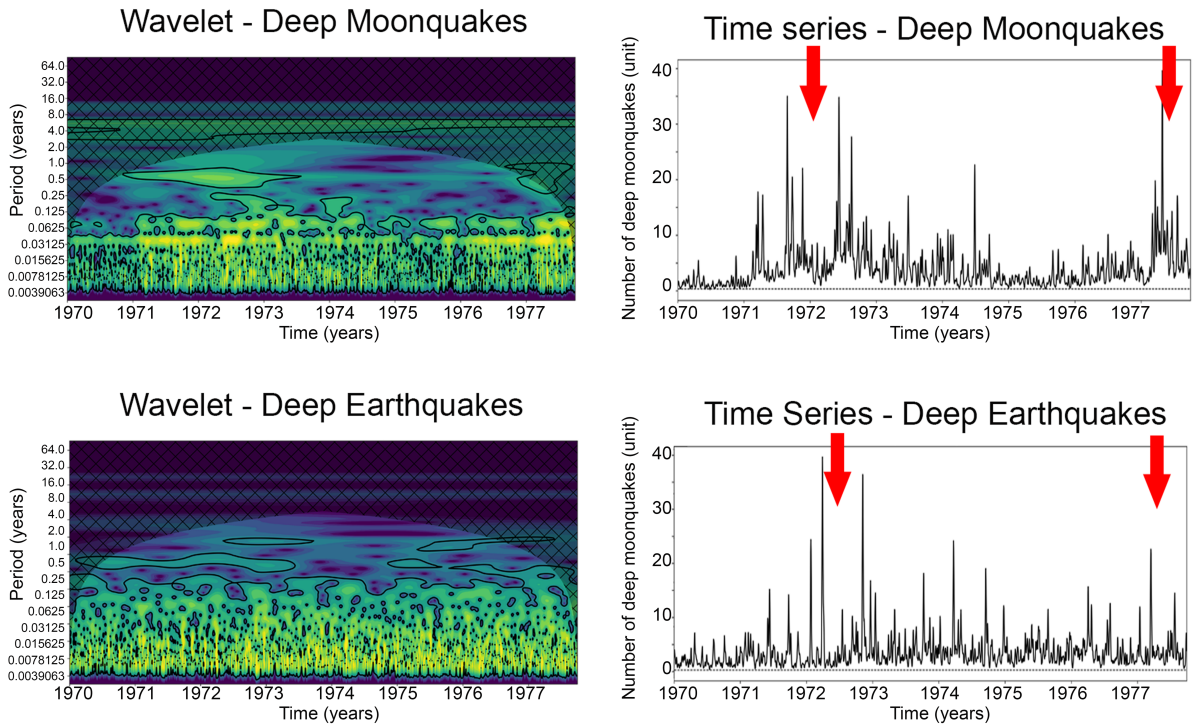

Figure 3.14 Wavelets of deep moonquakes and deep earthquakes, in the left. In the right, the time series showing prominent peaks of a large number of quakes occurrences.

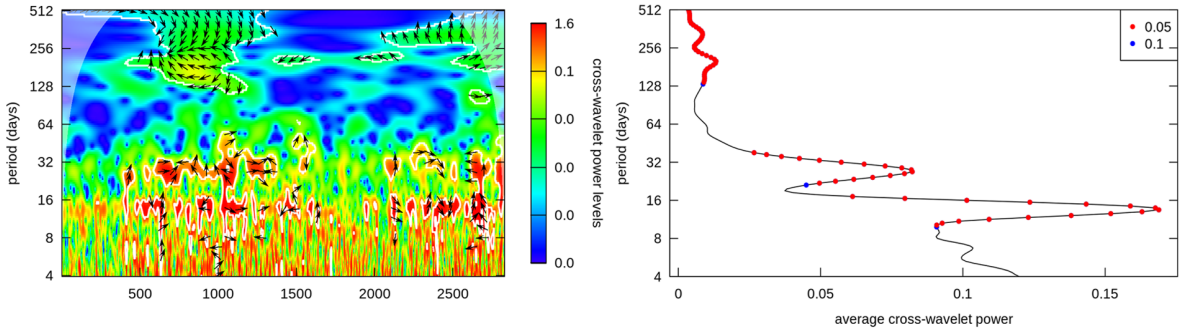

Figure 3.15 Coherence wavelet between deep moonquakes and deep earthquakes. The highest correlations occur in periods of 8, 18, and 182 days (blue balls).

Random Committee had 11161 total branches. Both models had an error of 4 %, which means that, of 2830 deep quakes, 113 are classified in the wrong way. Figure 3.17 shows the graph of the errors in the classification of the Random Tree model. The numeric/colored legend is the classes of counts of deep quakes per day that the model separated. The events correctly classifieds are “x” and the errors are the squares, which 100 % of the time the algorithm classified to a lower value of daily moonquakes.

Type ML model: functions	Type ML model: lazy	Type ML model: meta	Type ML model: misc	Type ML model: rules	Type ML model: trees
Classify	**Correlation coefficient**	**Mean absolute error**	**Root mean squared error**	**Relative absolute error**	**Root relative squared error**
Gaussian Processes	0.4943	1.8543	2.5427	85.03%	86.93%
Linear Regression	0.4912	1.858	2.5478	85.20%	87.10%
MultilayerPerceptron	0.9182	0.9891	1.317	45.36%	45.03%
SMOreg	0.4691	1.7686	2.6439	81.10%	90.39%
IBk	0.9871	0.0873	0.4691	4.00%	16.04%
Kstar	0.9862	0.123	0.4852	5.64%	16.59%
LWL	0.4633	1.9338	2.6226	88.67%	89.66%
AdditiveRegression	0.4316	1.9347	2.6386	88.72%	90.21%
Bagging	0.8048	1.2461	1.7787	57.14%	60.81%
CVParameterSelection	0	2.1808	2.925	100%	100%
MultiScheme	0	2.1808	2.295	100%	100%
RandomCommittee	0.9871	0.0873	0.4691	4.00%	16.04%
RandomizableFilteredClassifier	-0.0336	2.3774	3.6243	109.01%	123.91%
RandomSubSpace	0.7503	1.426	1.9917	65.39%	68.09%
RegressionByDiscretization	0	2.1808	2.925	100%	100%
Stacking	0	2.1808	2.925	100%	100%
Vote	0	2.1808	2.925	100%	100%
WeightedInstancesHandlerWrapper	0	2.1808	2.925	100%	100%
InputMappedClassifier	0	2.1808	2.925	100%	100%
InputMappedClassifier	0	2.1808	2.925	100%	100%
DecisionTable	0.6812	1.5015	2.1414	68.85%	73.21%
M5Rules	0.5488	1.7839	2.4451	81.80%	83.59%
ZeroR	0	2.1808	2.925	100%	100%
DecisionStump	0.2753	2.0805	2.812	95.40%	96.14%
M5P	0.5489	1.7839	2.4449	81.80%	83.59%
RandomForest	0.9604	0.6562	0.9609	30.09%	32.85%
RandomTree	0.9871	0.0873	0.4691	4.00%	16.04%
REPTree	0.6813	1.4921	2.1412	68.42%	73.20%

Figure 3.16 Results of ML models.

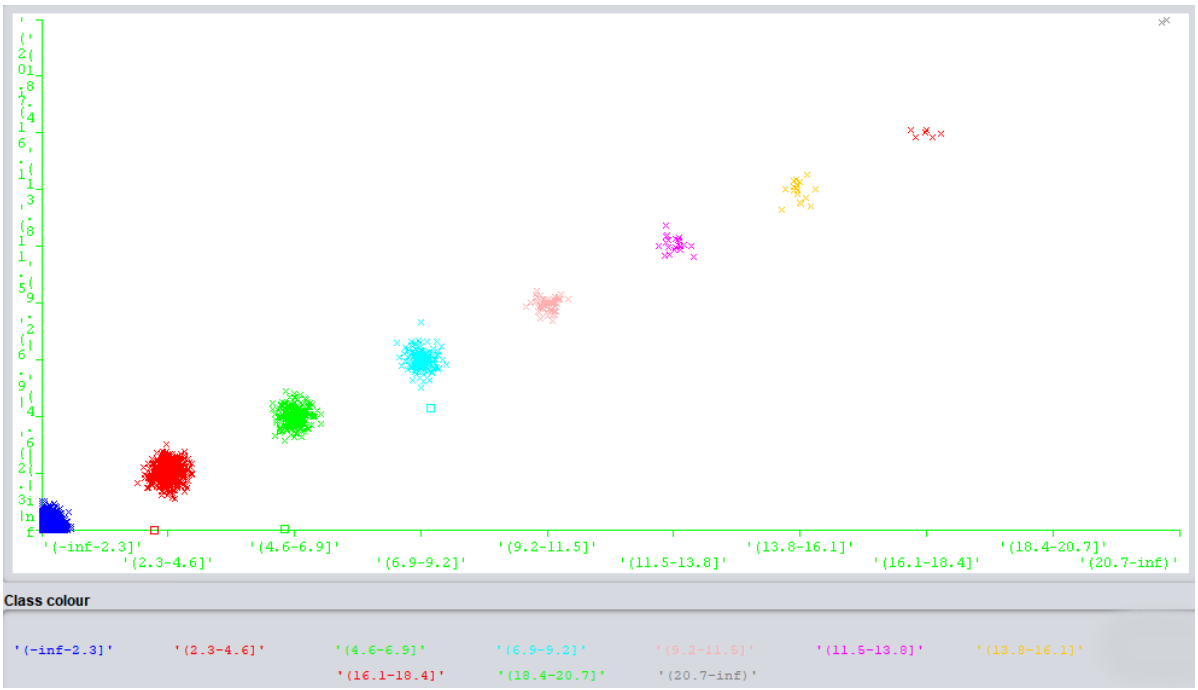

Figure 3.17 ML Random Tree model error, where the events of which class of deep quakes correctly classifieds are “x” and the errors are the squares.

Finally, the database was analyzed, still with ML (in Weka software), using the attribute evaluator mode. This mode infers the attributes/parameters that correlate within the database and the percentage to which they relate. It is necessary to inform the software which is the main parameter, which will be correlated with the others, then, the same step was performed twice,

once where the parameter deep moonquake was informed as to the main one and another where the deep earthquake is the main one. The correlation result between all 15 database parameters is shown below (Figure 3.18).

Parameters	Correlation (%)	Correlation (%)
A	-	-
AD	20	-
EC	50	-
IN	**100**	-
JD	20	-
MA	10	-
N	-	-
OM	-	**100**
PR	60	-
QR	50	-
TA	**90**	-
Tp	-	-
W	**100**	-
Deep_Moon	-	**100**
Deep_Earth	**100**	-

Legend:
Moon as principal parameter
Earth as principal parameter

Figure 3.18 Attributes correlation. The blue column represents the results from the deep moonquakes as the main time series and the orange column represents the results from the deep earthquakes as the main time series.

The relevant parameters for correlation with the deep earthquakes found in the processing were: The longitude of the ascending node (OM), 100 %, which is the horizontal orientation of the ascending node in the ellipse in relation to the vernal point and the deep moonquakes. The relevant parameters for correlation with deep moonquakes were: The inclination of the orbital plane (IN), 100 %; the argument of the Periapsia (W), 100 %, which is the orientation of the ellipse in the orbital plane; the true anomaly (TA), 90 %, which defines the position of the body in orbit along the ellipse; and the deep earthquakes. The argument of the Periapsia (W), the longitude of the ascending node (OM), and the inclination of the orbital plane (IN) are all dependent on coordinates and the reference structure of the chosen equinox/ecliptic of the epoch (time). The True Anomaly (TA) is the real angle in the plane of the ellipse, between Periapsia and the position of the Moon (Figure 3.19).

This result implies that only parameters of the Moon's position in the orbital plane itself influence the occurrence of deep moonquakes and, likewise, the position of the Earth in its own plane influences the occurrence of deep earthquakes. This means that the movement of the analyzed planetary body itself (angular velocity, torque) is the main causality of the events.

The remaining orbital elements that describe the orientation of the lunar orbit in relation to a particular coordinate system (that is, the longitude of the ascending node (OM) and argument of the Periapsia (W)) undergo secular and periodic changes. The regression period

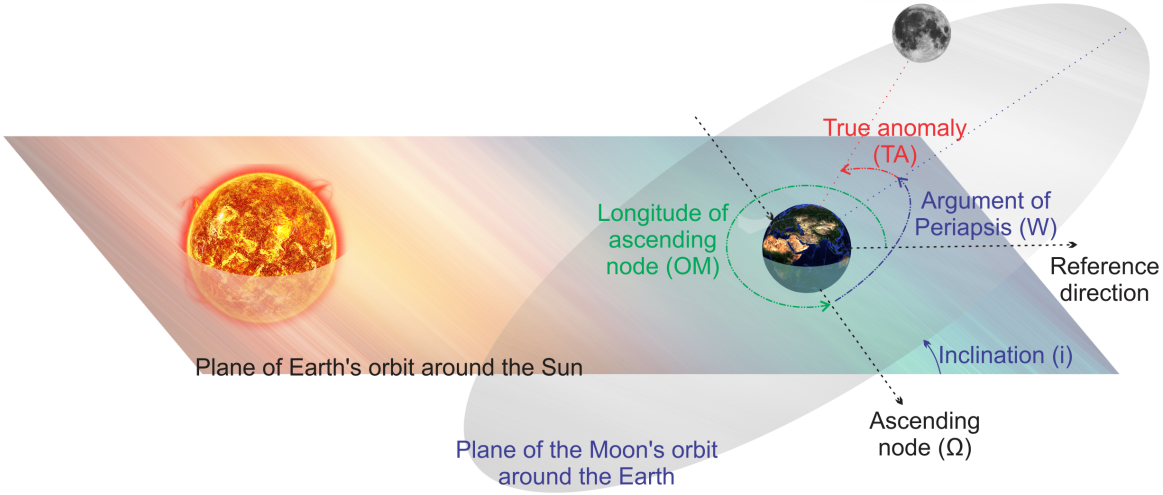

Figure 3.19 Relevant parameters for correlation with deep earthquakes and deep moonquakes.

for the longitude of the ascending node is 18.6 years. The precession period of the argument of the periapsis is 6.0 years [Note: The precession period of the periapsis longitude = 8.85 years]. With respect to a coordinate system referenced by the Earth's equator and equinox, the precession period of the argument of the periapsis is 8.85 years. With respect to a coordinate system referenced by the equator and the equinox of the Earth, the longitude of the ascending node does not regress by 360 degrees, oscillating on a straight rise of 0° over a period of 18.6 years. Therefore, there is no secular fee for the longitude of the ascending node. As a result, the precession period of the argument of the periapsis, when measured in relation to a coordinate system referenced by the Earth's equator and the equinox, is equal to the precession period of the periapsis longitude, when measured in relation to the referenced coordinate system by the ecliptic and the equinox.

The period of approximately 6 years in the relationship of the terrestrial and lunar orbital planes is consistent with the prominent peaks in the deep moonquakes and deep earthquakes series (middle of 1971 and middle of 1977), confirming that the highest occurrence of these events occurs when the planetary bodies are at the maximum points of its orbit, representing the greatest periods seen in wavelets, where a greater number of quakes occur, but with a low frequency (approx. 6 years). The correlation between the time series of deep moonquakes and deep earthquakes found in the analysis of WC, in periods of approximately 8 and 18 days, correspond to the moments when the Moon reaches the critical points of its orbit (maximum and minimum points of the orbital plane and nodal points) around the Earth, representing the shortest periods seen in wavelets, where fewer quakes occur, but with a very high frequency. For more details and discussion of the results, see Paper 2, in Chapter 4.

CHAPTER 4

Results and discussions

The results were arranged in three papers. The first one is in revision, the second one is in submission, and the last one is in preparation. The first deals with the shallower lunar layer, the regolith, which strongly influences the noise recorded in seismograms. Paper 1 analyzes the regolith layer below the Apollo 14 and 16 stations, in order to understand whether the composition, age, layer shape, and variability of the grains in each landing site change the noise registered.

The second deals with the physical causal mechanism of deep moonquakes, correlated with deep earthquakes. Deep quakes showed a correlation in their period of occurrence and also occur in specific structural layers.

The third makes the link between noise and seismogram, by analyzing the frequency contained in the records. Paper 3 investigates whether the orbital factors pointed out in Paper 2 also influence noise. Although the regolith, discussed in paper1, is the most influencing factor, orbital factors also subtly influence the noise recording.

4.1 Paper 1

ESTIMATION OF THE LUNAR REGOLITH LAYER USING APOLLO MISSION ACTIVE SEISMIC DATA

LS Villanova, E Yokoyama and STR Maciel

IN REVISION

[1]Villanova, L.S. - lyara.villanova@aluno.unb.br; http://lattes.cnpq.br/8444097347243654
[2]Yokoyama, E. - eyokoyama@unb.br; http://lattes.cnpq.br/9806242954314478
[3]Maciel; S.T.R. - susanne.maciel@gmail.com; http://lattes.cnpq.br/9121152391343596

[1][2]Institute of Geosciences - University of Brasília (UnB) - Brazil, Brasilia, Federal District, 70297-400
[3]Mathematics Department - University of Brasília (UnB) - Brazil, Brasilia, Planaltina, 73345-010

Abstract: Over the past 50 years, a significant advance in the progress of lunar research has reached due to the combination of telescopic, orbital, and surface observations. However, some fundamental scientific issues remain unclear, such as the dissipation of seismic waves in the regolith layer. The thickness of the regolith and its elastic properties has been debated since

1971 when the first results of seismic experiments from the Apollo mission were obtained. Since the Active Seismic Experiment developed at Apollo 14 and 16 missions throughout the 1970s, many studies have inferred different values for the regolith layer, as the Passive Seismic Experiment (PSE) records have a large amount of noise and these are affected by the difference in thickness, chemical composition, slopes and gradual transitions of shape of grains and breccias of the regolith layer in each Apollo station. In this context, the present study provides a new estimate of the thickness of the lunar regolith, using tomography inversion, interpretation of the critical point of refractive seismic and analytical solutions by synthetic model, focusing on the best estimate of the shape of the lunar surface layers. In our model slopes and depth changes in shallow regolith layers were based on re-analysis of active seismic data collected in the ASE experiments. The profiles generated in the processing showed a depth of approximately 8.3 m for the Apollo 14 data and 10.4 m for the Apollo 16, which is consistent with the values published by previous studies.

Introduction

The models currently accepted for the origin of the Earth-Moon system describe that the Moon was formed due to a giant impact between proto-Earth and a large planetesimal (Hartmann and Davis, 1975; Cameron, 2000; Borg et al., 2011; Rai and Westrenen, 2014; Canup and Asphaug, 2018). Due to the high energy and high fusion rate, some studies suggest that the Moon underwent a planetary differentiation process (Warren, 1985; Longhi, 2006; Elkins-Tanton, 2012). The lunar differentiation process is based on surface geological data, collected by Apollo missions and data acquired by remote sensors on orbital missions (Shkuratov, 2001; Fa, 010a; Bart et al., 2011). Besides, geophysical data were also acquired during the Apollo missions (e.g., magnetometry, gravimetry, and seismology) and their interpretations corroborate with the lunar differentiation model (Khan et al., 2006; Yan et al., 2011; Ling et al., 2019). Among the geophysical data, the seismographic data are the ones that present greater subsidies to support the lunar differentiation process and its stratification.

Throughout the Apollo missions, between 1969 and 1977, seismic activity was monitored on the lunar surface (Nakamura, 2008; Weber et al., 2010). The Passive Seismic Experiment (PSE), where seismographic stations recorded more than 13,000 seismic events (Latham et al., 1972; Nakamura, 2005), suggest that the Moon has a stratification similar to that of the Earth, with a crust (approx. 50 km thick), a mantle with approx. 1300 km thick, a liquid outer core and a solid inner core (approx. 90 km and 240 km thick, respectively) (Wieczorek et al., 2006; Jaumann et al., 2012; Kuskova et al., 2018; Kronrod et al., 2018). However, the proposed models of the internal structure of the Moon using the PSE data may be biased, since the acquisition of passive seismic data has probably been attenuated due to the thickness and composition of the regolith layer under the stations.

To mitigate the attenuation of seismic waves, National Aeronautics and Space Administration (NASA) performed an active seismic experiment, whose data provided parameters to calculate the thickness and nature of the lunar regolith. The active seismic experiment (ASE) was carried out during Apollo missions 14, 16, and 17 (Kovalch and Watkins, 1973; Lauderdale and Eichelman, 1974; NASA, 1980; Horvath et al., 1980; Heffelsa et al., 2017). ASE data suggest that the thickness of the regolith under the seismographic stations ranges from 9 to 19 m

(Kovalch and Watkins, 1973; Horvath et al., 1980). Recently, a new estimative of lunar regolith thickness was obtained by orbital and rover missions (Ling et al., 2019). Data from the lunar orbit laser altimeter (LOLA) were used to estimate the thickness of the regolith, where the estimated regolith layers vary from 3 to 16 m thick (Shkuratov, 2001; Bart et al., 2011). In 2013, the Chang'E-3 mission provided lunar penetration radar (LPR) data that suggested a regolith layer ranging from 5 to 12.5 m thick (Ling et al., 2019). This uncertainty in the thickness and composition of the regolith can influence the estimates of the internal structure of the Moon, since the differences between the arrival times of shear and compression waves in the records of the stations are what refine the models, analyzing the distribution of seismic velocity in the subsurface and the decline in the amplitude of the shear wave as a function of distance (Horvath, 1979). The complex waveforms of lunar seismic signals and the low coherence between the different components caused by the regolith make it very difficult to identify these reflected or converted arrivals.

In this scenario, the present study aims to provide a new estimate of the thickness of the lunar regolith, using different methodological approaches of shallow seismic (tomography inversion, interpretation of the critical point of refractive seismic and analysis by synthetic model), from the reanalysis of active seismic data collected by the Apollo missions in the ASE experiments. Also, this study will discuss the implications of the thickness and nature of the regolith for the seismic experiments and consequent models of internal lunar structure.

Background

Geological context

The processes of lunar origin and evolution culminated in the formation of two large geomorphological features that make up the surface of this satellite, the Highlands, with elevated areas of light color (Parmentier et al., 2002; Yan et al., 2011) and the Maria, darker colored plains (Jolliff et al., 2000; Wieczorek and Phillips, 2000). The Highlands occupy approximately 85% of the Moon and have a rougher appearance, with a higher density of impact craters (density of $\geq$ 20 km craters on the Maria of N(20) = 6.5 $\pm$ 1 and the Highlands of N(20) = 184 $\pm$ 3 (Fassett, 2016). Maria occupies approximately 15% of the Moon's surface and has fewer impact craters than the Highlands, suggesting that it has a younger age of formation. Geochronological studies carried out on samples brought by the Apollo missions confirmed that the Highlands are older than Maria's areas (Jolliff et al., 2000; Arai et al., 2008; Borg et al., 2011; Hachay and Khachay, 2019).

Most of the craters on the Moon were recognized as the result of an early bombardment. In contrast, the slightly cratered basalt surfaces of Maria had escaped this bombardment, being much younger. The ages of Maria's surfaces, dated from samples from the Apollo Missions, return between 3.3 and 3.8 billion years old, establishing that the intense craters in the Highlands occurred more than 3.8 billion years ago. Most of the Highlands samples were dated between 3.8 and 4.3 billion years old (Taylor, 2007). Furthermore, geochemical analyses performed in lunar samples show that the regolith of the Highlands is rich in aluminum while the Maria regolith is rich in iron and magnesium, suggesting distinct differentiation stages (Ling et al., 2019). The term regolith refers to the unconsolidated layer of rock fragments of all sizes that cover the bedrock (Shkuratov, 2001; Jaumann et al., 2012; Ling et al., 2019). Lunar regolith is

composed of lithic fragments, minerals, and glass, and includes many of the silicate minerals present on the Moon, components of the series of pyroxene-olivine solid solution, together with several trace minerals (Shkuratov, 2001; Badescu, 2012; Pernet-Fisher et al., 2019).

The primary regolith formation process is associated with meteoritic bombardment. The main phase of this bombardment occurred before the basalts flows and it continues to the present times. This constitutes the main agent of weathering and formation of rocks, breccias and regolith that acts on the lunar surface (Rasmussen and Warren, 1985; Bart et al., 2011; Jaumann et al., 2012; Ling et al., 2019). For example, Apollo 14 breccia studies have indicated that thermal metamorphism is the most reasonable model for breccia lithification (Wieczorek et al., 2006; Gagnepain-Beyneix et al., 2006; Rai and Westrenen, 2014). These breccias are formed when the hot melted material welds the colder clastic fragments together during the meteoritic impact. In the case of lunar breccias, there is no definite distinction between "soil matrix" and "clasts", because of the serial texture of the rock. In these cases, fragments larger than 1 mm are referred to as clasts and smaller than 1 mm in the “soil matrix”. The local breccias have a higher concentration of siderophile elements than lunar rocks of igneous origin, containing mixed meteoritic material (Lauderdale and Eichelman, 1974; Horvath et al., 1980). The formation of craters by impacts erodes geological characteristics to form the regolith, exposing a relationship between its thickness and the ages of the materials on the surface. A characteristic of a regolith reference suite, as different stratigraphic features, grain size, sorting, presence of graded bedding, and the identification of former surface horizons and their variations with depth, illustrate the local (landing site) influence well and directly influence the seismic signal, since the Vp changes with variations in physical properties.

Seismic experiments of Apollo missions and the regolith

As mentioned before, between the end of the 60s and the beginning of the 70s, NASA carried out Apollo missions, whose main objective was defined as the investigation of specific lithology or geological processes of each site stipulated for landing (Figure 4.1). The station 11 operated only 21 terrestrial days, before the loss of the uplink command, which ended its operation and at Apollo 17 the equipment deployed was a lunar surface gravimeter (LSG). The remaining four stations make up the Apollo seismic network. During the investigations, several experiments were carried out, among them the one of Active Seismic Experiment (ASE) (only in Apollo 14, 16 and 17* - Apollo 17 had an active seismic experiment, however, it is part of another program, the LSPE, because the equipment was different), whose data were used in this study.

Apollo 14 mission landed on the Fra Mauro Formation (Maria region), which covers large areas on the nearside of the Moon (Lauderdale and Eichelman, 1974). The Apollo 16 mission to the Highlands of the central region on the nearside of the Moon raised a series of questions about the nature of the original lunar crust, the effects of impact processes on it, and the interpretation of lunar relief forms from photographic evidence (Shkuratov, 2001; Bart et al., 2011; Yan et al., 2011). The regolith in the Apollo 16 Lunar Module area is generally thin (about 1 cm) and thickens to 15 cm or more, where it forms fillets around the friable boulders of the clear soil matrix (Lauderdale and Eichelman, 1974; Horvath et al., 1980; Rasmussen and Warren, 1985; Jolliff et al., 2000).

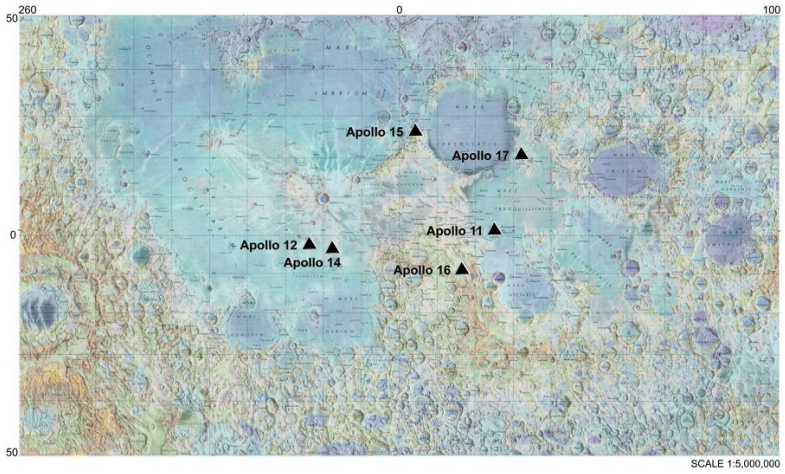

Figure 4.1 Configuration of the installation of the Apollo lunar seismographic network. Each black triangle represents a seismic station. The background image shows topographic highs and lows, the colors represent elevation, from lowest (blue to purple) to highest (yellow to white). Source: NASA/Goddard Space Flight Center/Arizona State University.

The seismograph implanted at the Apollo 16 station was the most sensitive of the four lunar seismographic stations in operation at the time. Based on the initial 45-day operation record, seismic events occurred at a rate of 10,000 per year. The on-site rate for Apollo 14 was 2,000 per year and for Apollo 12 and 15 700 per year. The greater sensitivity of the Apollo 16 seismograph was attributed by Latham et. al. (1972) to the depth and elastic properties of the regolith, the inference is that the regolith below Apollo 16 is deeper or weaker or both. Although the Apollo 14 and 16 rocks are approximately the same age (Rasmussen and Warren, 1985; Arai et al., 2008), it is assumed that the regolith is significantly thicker at the Apollo 16 site, due to large craters that have been filled by the erosion of its edges. During their early history, these areas were subjected to a high rate of meteorite impact flow (Canup and Asphaug, 2018; Hachay and Khachay, 2019), so that large craters were more likely to form (Hiesinger and Head, 2006; Jaumann et al., 2012).

Regolith seismic response

Kovalch & Watkins (1973) and Horvath et al., (1980) used seismic signal amplitude spectrum analysis methods, inferring velocities from 92 to 114 m/s for the regolith, where they characterized it as a homogeneous layer and with different thicknesses for each station and determined velocities at about 300 m/s for the underlying material at the three locations. These velocities and their increase in depth have been demonstrated by laboratory measurements (Houston et al., 1974), where velocities and their gradients are higher for "light material" (Highland regolith), derived from highly feldspar rocks and a wide variety of breccias, than those of the "dark material", which have a similar composition to Maria's basalts.

In these studies, the lunar structure was modeled as a series of homogeneous isotropic horizontal layers. The average ratios of calculated horizontal-vertical spectral amplitude and the shear velocities of the best fit models in the different locations differed from the average of

all locations by up to 20%. According to Horvath (1979), these variations may indicate an inclination in the ellipse of the movement of the particles, which can be produced by inelastic effects of the medium, by the presence of anisotropy, by lateral heterogeneities or by instrumental effects. Thus, the works have good results in terms of information about the physical properties of the lunar interior, however the limitations for modeling ellipticity and the disregard of heterogeneities in the layers make the technique not refined for smaller details of the more superficial structure (first meters subsurface) of the Moon, in this way, our study aimed to use techniques focusing on a better estimate of the lunar surface layers, taking into account inclinations and depth changes in the modeling of the shallow layers, in order to better visualize the shape of the layers and gradual variations in the velocity model.

The regolith at the Apollo 14 site was first stipulated by Horvath et al. (1980) to be approximately 9.5 m thick, but on older surfaces, such as the Fra Mauro Formation, where the regolith is abnormally thicker, it was indicated to contain approximately 11 m, possibly due to accumulations of fragmented debris that filled old craters. In Apollo 16, they suggested that a unit of debris and breccias or impact derivatives of undetermined depth underlies a 12.2 m deep regolith. Regolith, rocks, ejecta, and basalt are typical elements that appear on the Moon. After the impacts, the blocks and regolith are mixed and deposited by layers (Lv et al., 2020). However, the variety of types of rocks collected indicated that the cracks in the Cayley plains are heterogeneous and suggest that they were deposited by a turbulent process characteristic of ejection from large basins, which may present relevant differences in depth. At the same time, the amplitude of the signal is affected by many factors, including the geometrical spreading, shapes of the reflectors, velocity contrasts, and physical parameters (Lv et al., 2020).

Materials and methods

Seismic array and database

Apollo Lunar Surface Experiment Package (ALSEP) is a collection of geophysical instruments designed to monitor the environment of landing sites for at least one year. Among them, there is the Passive Seismic Experiment (PSE), where moonquakes were recorded from natural sources and the Active Seismic Experiment (ASE), where the sources were derived from explosions. The ASE is part of the package of active lunar surface seismic experiments (ALSEP) from the Apollo 14 and 16 missions. The objective was to generate and monitor seismic waves on the lunar surface and use this data to study the internal structure of the Moon at a depth of several tens of meters. The ASE sources are obtained in three ways: (1) Thumper, where a packet of grenades is launched by rocket and the impulse produced by the lunar module (LM); (2) Explosive, where a short stick fired by an astronaut is used to detonate small explosive charges and (3) Grenade, where a grenade (MPA) is launched by a rocket. The PSE was designed to study global areas of the Moon, with greater depth, and the ASE to study local and shallow areas.

In the Apollo 14 ASE, three geophones were allocated towards the south of the ALSEP central station (Figure 4.2a). For convenience, the geophone closest to ALSEP is called “geophone 1” and the furthest “geophone 3”. The firing started on geophone 3 and continued at 4.6 m intervals along the line, firing 21 pulses. In the Apollo 16 ASE arrangement (Figure 4.2b), the operation started on the geophone 3 and continued with intervals between 4.75 m (except

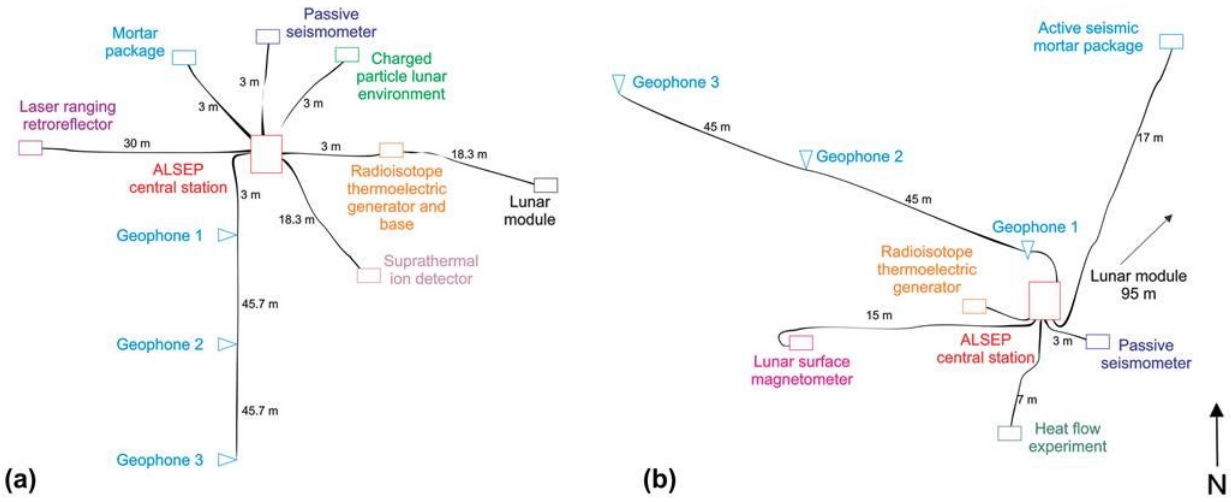

Figure 4.2 Deployment configuration for (a) Apollo 14 ALSEP and (b) Apollo 16 ALSEP. Adapted from Lauderdale and Eichelman, 1974.

between positions 11 and 12 and positions 18 and 19, which are in intervals of 9, 5 m) towards geophone 1, totaling 19 shots.

The active seismic data recorded between 1971 and 1972 by the Apollo 14 and 16 seismographs were reprocessed here. The choice of the arrival times of the seismic wave was made with attention dedicated to the estimation of uncertainties and associating the arrival of the P wave in the records of the Apollo missions in each shot. A total of 32 processing events were used, 13 from Apollo 14 and 19 from Apollo 16, shown in Table 1 (Figure 4.3).

New data processing

We calculated the velocity fields for each fixed source location of the ASE experiments using refraction analysis. Pre-processing was performed using Seismic Unix software (Cohen and Stockwell Jr, 1999), where the common-shots were rearranged into common-receiver gathers, to allow better visualization of the seismic phases. Apollo 14 and Apollo 16 data were divided into 3 parts, due to the acquisition design. We used Refrapy software (Guedes et al., 2018) to pick P waves arrivals for each common-receiver. From the markings, a depth profile was modeled using the Plotrefa software, from the SeisImager package (Geometrics Inc and OYO Inc., 2009), using tomography inversion. By marking the estimate of the arrival of the P wave in the records (Figure 4.4), it was possible to model the data with the Plotrefa software, generating a depth profile in relation to the Vp below the seismic acquisition line each station.

For validation purposes, we modeled a synthetic seismogram using the results found by tomography inversion, using the Geoscilabs package, from Python, considering variations in velocity, impedance and reflectivity, without considering changes in density. A synthetic Vp by depth model was also made, using the pyGIMLi package (Giroux and Larouche, 2013), from Python, according to the positions of the geophones in the acquisition of ASE data. This synthetic model performs ray tracing for a two-layers and a vertical gradient model and compares the resulting traveltimes to analytical solutions of traveltime at a minimal offset of the direct and

Apollo Site	Active Event	Year	DOY	Origin Time			Data End Time			Distance (m)			
				Hour	Min	Sec	Hour	Min	Sec	G1	G2	G3	G4
A14	Thumber Shot 1	1971	37	18	10	38,781	18	10	43,78	91,44	45,72	0	-
	Thumber Shot 2			18	12	13,494	18	12	18,49	86,868	41,148	4,572	-
	Thumber Shot 3			18	13	33,315	18	13	38,32	82,296	36,576	9,144	-
	Thumber Shot 4			18	14	38.890	18	14	43,89	77,724	32,004	13,716	-
	Thumber Shot 7			18	20	31.980	18	20	36,98	64,008	18,288	27,432	-
	Thumber Shot 11			18	24	12,121	18	24	17,12	45,72	0	45,72	-
	Thumber Shot 12			18	26	29,733	18	26	34,73	41,148	4,572	50,292	-
	Thumber Shot 13			18	27	18,322	18	27	23,32	36,576	9,144	54,864	-
	Thumber Shot 17			18	31	16,797	18	31	21,8	18,288	27,432	73,152	-
	Thumber Shot 18			18	32	28,716	18	32	33,72	13,716	32,004	77,724	-
	Thumber Shot 19			18	33	47.770	18	33	52,77	9,144	36,576	82,296	-
	Thumber Shot 20			18	34	42,306	18	34	47,31	4,572	41,148	86,868	-
	Thumber Shot 21			18	37	6.960	18	37	11,96	0	45,72	91,44	-
A16	Thumber Shot 1	1972	112	20	1	51,851	20	1	56,85	91,44	45,72	0	-
	Thumber Shot 2			20	2	38,758	20	2	43,76	86,868	41,148	4,572	-
	Thumber Shot 3			20	3	17,376	20	3	22,34	82,296	36,576	9,144	-
	Thumber Shot 4			20	3	53,157	20	3	53,21	77,724	32,004	13,716	-
	Thumber Shot 5			20	4	49,709	20	4	54,71	73,152	27,432	18,288	-
	Thumber Shot 6			20	5	27,299	20	5	32,3	68,58	22,86	22,86	-
	Thumber Shot 7			20	6	13,675	20	6	18,68	64,008	18,288	27,432	-
	Thumber Shot 8			20	6	49,332	20	6	54,33	59,436	13,716	32,004	-
	Thumber Shot 9			20	7	30,203	20	7	35,2	54,864	9,144	36,576	-
	Thumber Shot 10			20	8	13,808	20	8	18,81	50,292	4,572	41,148	-
	Thumber Shot 11			20	9	42,508	20	9	47,51	45,72	0	45,72	-
	Thumber Shot 12			20	10	29,512	20	10	34,51	36,576	9,144	54,864	-
	Thumber Shot 13			20	11	6,603	20	11	11,6	32,004	13,716	59,436	-
	Thumber Shot 14			20	12	14,656	20	12	19,66	27,432	18,288	64,008	-
	Thumber Shot 15			20	12	45.090	20	12	50,09	22,86	22,86	68,58	-
	Thumber Shot 16			20	13	23,572	20	13	28,57	18,288	27,432	73,152	-
	Thumber Shot 17			20	14	12,072	20	14	17,07	13,716	32,004	77,724	-
	Thumber Shot 18			20	14	52.150	20	14	57,15	9,144	36,576	82,296	-
	Thumber Shot 19			20	15	51,232	20	15	56,23	0	45,72	91,44	-
A17	Explosive 1	1972	352	0	42	36,808	0	42	51,84	2899	2813	2867	2889
	Explosive 2		353	0	44	56,827	0	45	11,86	334	426	377	372
	Explosive 3		353	3	7	22,312	3	7	37,34	246	338	291	291
	Explosive 4		351	19	8	34,691	19	8	49,72	262	172	211	213
	Explosive 5		352	23	16	41,061	23	16	56,09	2280	2365	2334	2352
	Explosive 6		350	23	48	14,583	23	48	29,61	1199	1234	1190	1145
	Explosive 7		351	2	17	57,111	2	18	12,14	787	840	791	751
	Explosive 8		352	3	45	46,094	3	46	1,09	178	106	124	114

Figure 4.3 Table 1 - Active Seismic Experiment Data Catalog (Lauderdale and Eichelman, 1974).

critically refracted wave, governed by Snell's law. An approximation of the raypath is found by the shortest-path through a grid of nodes, improved by secondary nodes along the cell edges.

Results

The Vp depth profile generated for Apollo 14 and Apollo 16 ASE indicates the existence of an interface where the P wave propagation velocity difference occurs (Figure 4.4), interpreted as a possible regolith-rock limit at different depths for Apollo 14 and Apollo 16 sites.

Figure 4.5a and 4.5b show a discontinuity (or steeper gradient) at a depth of approximately 8.3 m (Apollo 14) and 10.4 m (Apollo 16), which is proposed as a regolith-rock/large scale ejecta interface. These values are similar to the published values of 9.5 m and 12.2 m by the first NASA report (NASA, 1980), for Apollo 14 and 16 stations, respectively, whose difference in the position of the interface may be related to different weights of the error of data assigned in processing (Gagnepain-Beyneix et al., 2006) and may also reflect changes in velocity related to fractures produced by impact craters or the possibility that seismic data are sampling the junction of different lunar terrains (Lognonné et al., 2003).

In the regolith layer, mean Vp values of 119.5 m/s were found for Apollo 14 and 119.8 m/s for Apollo 16 and the supposed adjacent layer of rock values equal to and greater than 300 m/s. In addition to this discontinuity (abrupt increase in the P wave propagation velocity) at 8.3 m in Apollo 14 and 10.4 m in Apollo 16, it is possible to observe in the resulting graph (Figure 4.5c and 4.5d) of the inversion model made using the WaveEq software, from the SeisImager package, that there are gradual transitions of the crustal velocity values to the addition of, on average, 6 m for the Apollo 14 and 2 m for the Apollo 16.

For comparison purposes, a synthetic model with random noise was made using the Geoscilabs package in Python (Figure 4.6a), considering the values of Vp and layer depth found in the tomography inversion model (Figure 4.5a and 4.5b), without considering changes in other factors, such as density (Figure 4.6a). It is possible to observe in the original seismogram (Figure 4.6b) that the critical point, where the direct wave (red line) and the refraction (blue line) cross, in fact, occurs in a position similar to that of the synthetic generated to test the model's characteristics (Figure 4.6a), however with approximately 5 m increase in the x-axis (Offset) of the graph. The critical point is used in the interpretation of refractive seismic data as a factor that explains the depth location of the refractory interface, that is, the interface/layer in which there is a change in the elastic properties of the medium, which increase Vp. This small difference between the distance in the synthetic model and the actual data may be due to a variation in the density of the material since the granulometry of the regolith gradually increases with the depth and there is an increase of blocks derived from the basement rocky.

Considering the values found of 8.3 m and 10.4 m for the regolith thickness below Apollo 14 and Apollo 16, a synthetic Vp by depth model was created, using the pyGIMLi package, filled with the positions of shots and geophones of the original acquisition. We compared the precision of 0 to 5 secondary nodes, performing travel time and P wave recording time calculations (Figure 4.7).

Adding the gradual increase in the velocity (Figure 4.7b), the analysis by synthetic model showed adequacy to the characteristics of the ASE data, with the calculated synthetic analytical values (Figures 4.7c, e, and f) of 230 ms and 38 m (average values between Apollo 14

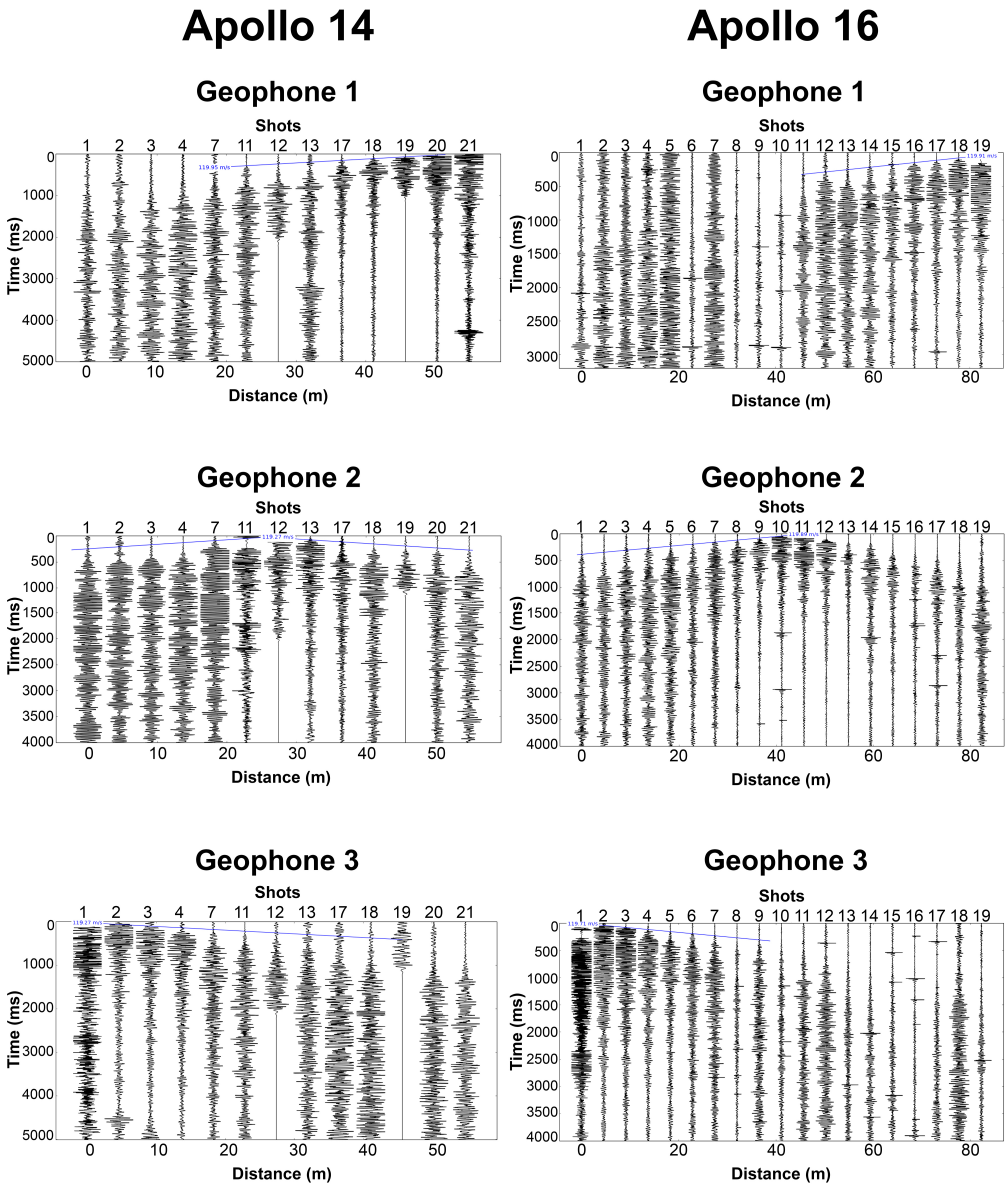

Figure 4.4 Apollo 14 and Apollo 16 seismic records. In blue, the estimated arrival of the P wave and its respective Vp.

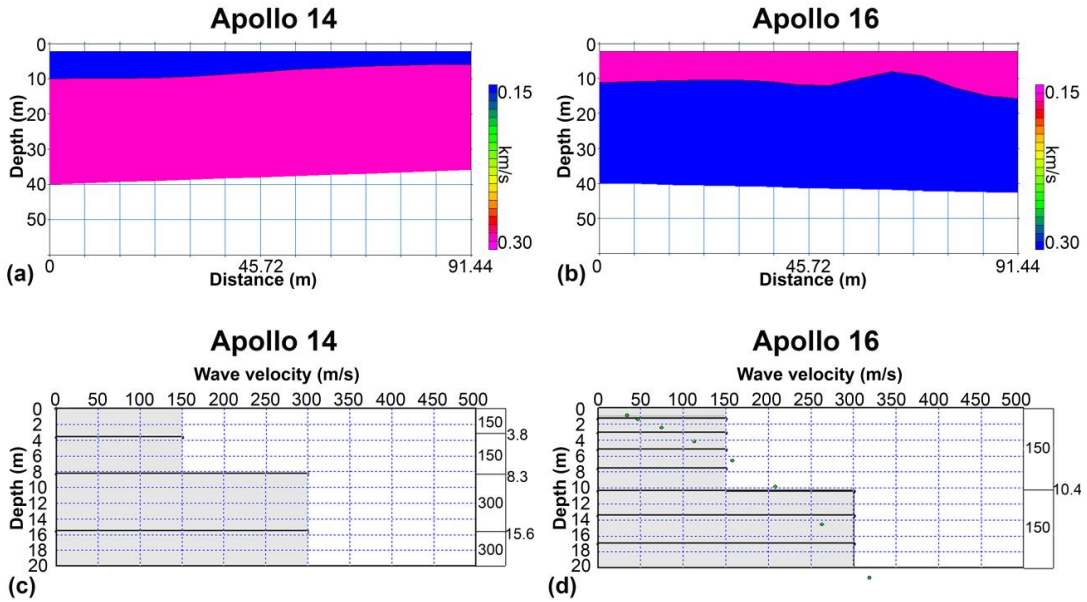

Figure 4.5 Tomography inversion of Vp below the seismic acquisition line, developed for (a) Apollo 14 and (b) Apollo 16. (c) Inversion layer model considering slopes made using the software WaveEq, from the SeisImager package, for Apollo 14 and (d) for Apollo 16.

and Apollo 16) (Figure 4.6) for the critical point, referring to the location of the depth of the refractory layer, against 252 ms and 36.58 m for the values found in the original seismogram.

Finally, this average of 9.35 m concerns the regolith layer (Figure 4.8) in the diagram block of the lunar crust, composed of increasing granulometry with depth, represented by the first layer in the inversion with an average of 150 m/s (0.15 km/s) of Vp, up to the lower layer, of large scale ejecta the refractory layer in the inversion, with 300 m/s (0.3 km/s) of Vp. Figure 4.8c is from NASA publications, where it shows the relationship between Vp and gradual fracturing of the crust.

Discussion

Kovalch & Watkins (1973) published one of the first works to process ASE data, using a time-aligned seismic recording section method, assigning 8.5 m of regolith depth for Apollo 14 and 12.2 m for Apollo 16. Our processing used the same data set, and we assigned 8.3 m and 10.4 m deep for the same stations, respectively. Currently, other geophysical methods have been employed to study regolith. Among them, Shkuratov et al. (2001) used the Kaguya LRS data, where they assigned 1.5 m to 10 m (average of 5 m) of regolith depth for Maria and 1 m to 18 m (average of 12 m) for the Highlands; Fa et al. (2010) used data from the Chinese Chang'E-1 mission, finding 4.5 m for Maria and 7.6 m for Highlands; Bart et al.(2011) used data from NASA's LROC, and published the values of 5.6 m for Maria and 11.2 m for Highlands and, more recently, Ling et al. (2019) used the LPR data from the Chinese Chang'E-3 mission and allocated 5.2 m for the regolith in the Maria area and 9.2 m for the Highlands area. The graph in Figure 4.9 compares the average values of regolith depth between the works cited. Works with

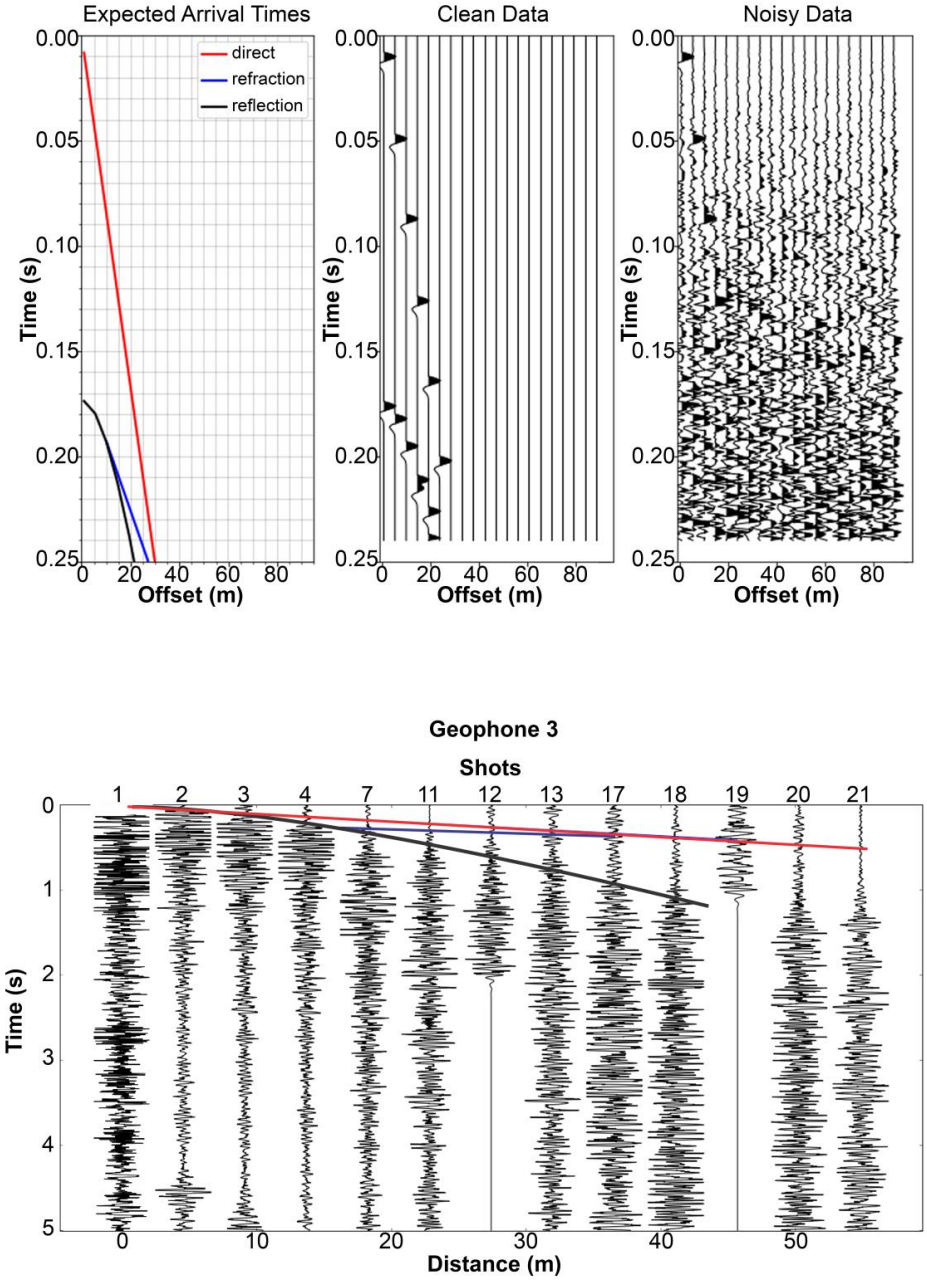

Figure 4.6 Synthetic model with noise for Apollo 14, made using the Geoscilabs package, from Python, considering variations in velocity, impedance and reflectivity, without considering changes in density (up) and original Apollo 14 seismogram, with markings (down).

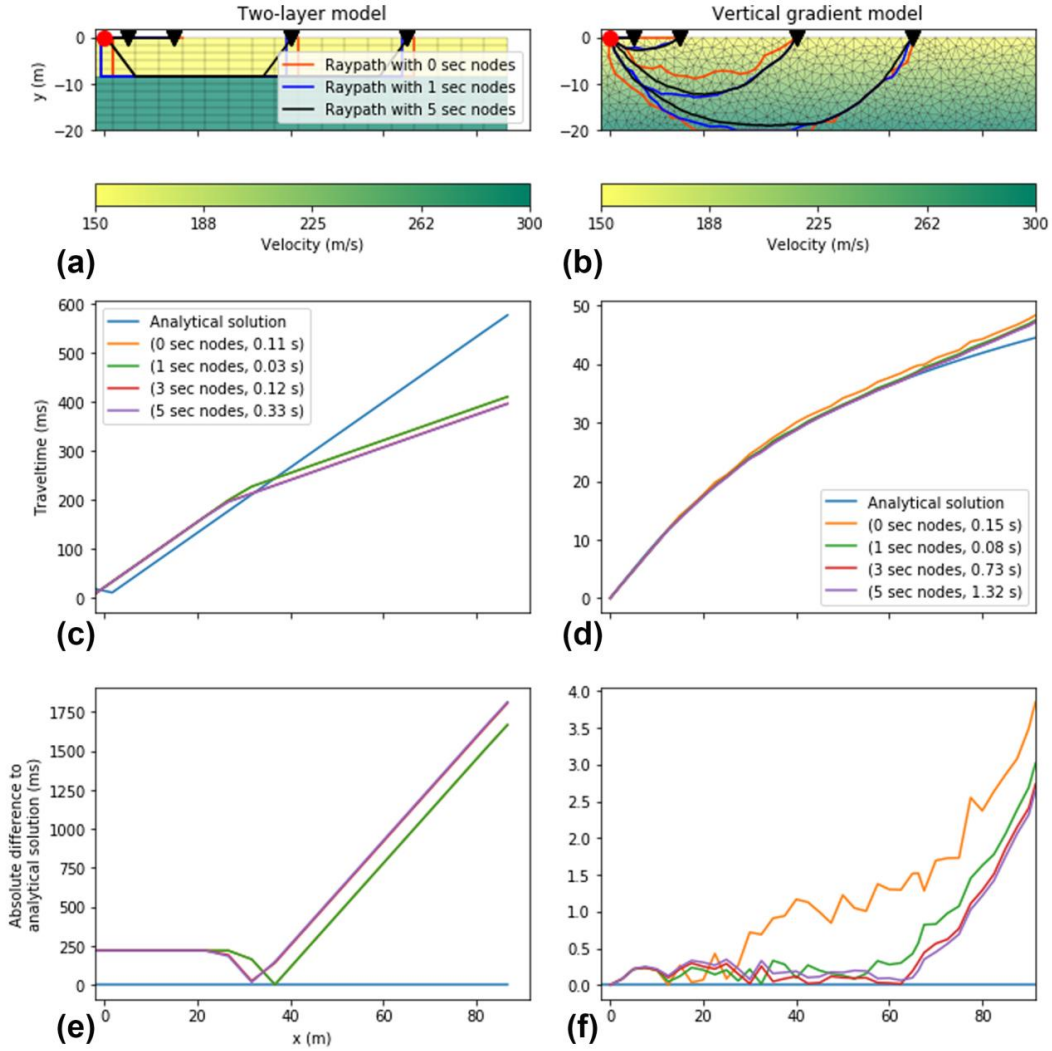

Figure 4.7 Analysis of the synthetic reflective layer velocity and depth model: (a) 2-layer model with a depth (interface) of 9.35 m (average between 8.3 m and 10.4 m) and constant velocities of 150 m/s and 300 m/s; (b) model with vertical gradient; (c) wave path time calculations (according to the number of nodes) (1 node = direct wave and 5 nodes = refracted wave); (d) error for calculating 0-5 secondary nodes; (e) and (f) P wave recording time calculations.

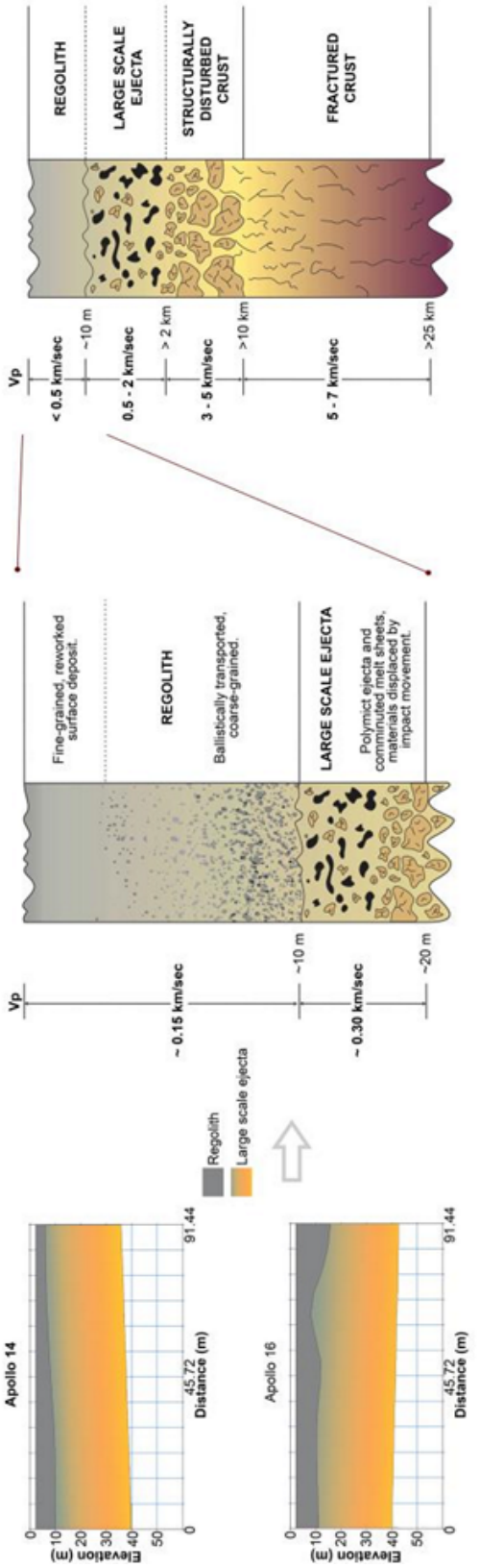

Figure 4.8 Block diagram of the lunar crust, with discrimination of layers and their respective Vp (in km/s)(up). The zoom under the first layer (middle), on the left side, represents the characteristic of gradual granulometric increase of the regolith and its limit with the refractory layer (large scale ejecta) found on the tomography inversion model (down).

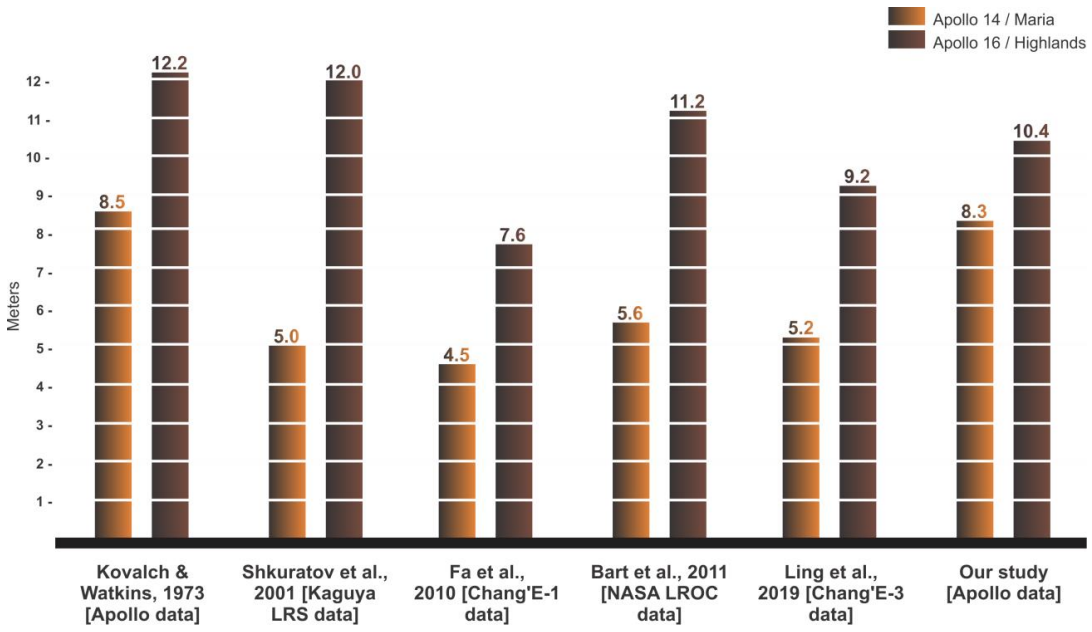

Figure 4.9 Comparative graph of average values of regolith depth between previous works.

Chang'E data used Lunar Penetrating Radar (LPR) and/or image analysis, as well as works using data from Kaguya LRS and NASA LROC are also composed of image analysis.

In general, studies that used non-seismic data found lower mean values of the regolith depth, as they analyze lunar geological areas in a regional/global data set (Apollo 14 is located within the Maria area and Apollo 16 within the Highlands area), unlike the works that used the seismic data from ASE (Kovalch and Watkins, 1973; Horvath et al., 1980; Villanova et al., 2021a), whose data set is local. In any case, the average depth range of the regolith for Maria areas and Highlands areas is agreed between all of them.

The recorded PSE data have a dominant peak in the average spectral amplitude of about 0.45 Hz, which deviates to lower frequencies with increasing depth (Horvath, 1979). Since the spectral amplitude ratios are dominated by long-term noise at frequencies where the amplitudes are low, of about 1.6 and 1.7 Hz for stations 14 and 16, respectively, they are generally independent of the depth of the source, where spectral rates are mainly determined by the physical parameters of the zone close to the surface (Horvath, 1979), such as regolith, so the records have a large amount of noise and are affected by the difference in thickness of the regolith layer in each Apollo station, its chemical composition and the great variability in the shape of grains and breccias. The sensitivity of the travel times of the seismic waves, however, provides a model of average velocity in two layers but does not allow discriminating between a continuous increase and clear interfaces with great certainty.

Passive seismic lunar signals have emergent beginnings from Vp records, gradually increasing to a maximum spectral peak of, on average, 0.85 Hz for the horizontal component of soil movement and 1.6 to 1.7 Hz for the vertical component (Horvath, 1979) and then slowly decay. After the first or the first two cycles of the initial movement of the P wave, the movement of the ground (regolith) becomes so complex that there is little or no correlation between any two

components. Thus, many of the analysis techniques considered useful in terrestrial seismology cannot be applied directly to the processing of PSE data in a satisfactory way, being rarely possible to determine the direction of propagation of the particle movement by analyzing a single station (Latham et al., 1972). These and other unusual characteristics of the lunar seismic signals have been interpreted as resulting from intense seismic waves but subjected to losses due to the heterogeneous layer in terms of composition and depth of regolith that covers the entire surface of the Moon. It is attributed that the variations in the detection rates between the stations are mainly due to the differences in the thickness of the local regolith of each seismic station. Corresponding variations in the amplification of soil movement would explain the differences in sensitivity between them. The fact that the variation exists is confirmed by measurements of the relative amplitude of the impact seismic signals (Latham et al., 1972). The background noise in the registers of each station has different characteristics, related to the depth and the elastic properties of the regolith in each location. This explains the much higher sensitivity at the Apollo 16 station, for example, concerning the records compared between all other stations and its higher resolution in modeling.

The velocities, then, are characterized by two zones; a thin surface zone (approx. 10 m thick) with a high-velocity gradient (regolith), followed by a low-velocity gradient zone (large ejecta). The lower velocities extend to a greater depth in Apollo 16, which may reflect a greater unevenness due to the bombardment of meteoroids, which exists in different forms over each lunar area, implying greater soil movement (regolith) and greater movement complexity. Horvath (Horvath, 1979) assigned the values of 2.3, 1.6, 2.1, and 1.7 Hz for Apollo 12, 14, 15, and 16, respectively, as the frequency at which the signal's spectral ratio becomes that of noise. It is possible to observe that Apollo 12 and 15 have much higher values, which may suggest greater lateral heterogeneities since they are located in transitional areas, but this will not be discussed here. The higher frequency of Apollo 16 spectral ratio, in relation to Apollo 14, can be attributed to the greater existence of unevenness in the reflective layer, pointed out in our model (Figure 4.5). Therefore, parameters such as the compositional difference between Maria and the Highlands and aspects of their geological formation can be attributed as the main influencers of the velocity of propagation of seismic waves, but the unevenness in the reflective layer, mainly due to greater exposure to the bombardment of meteoroids, can be attributed as main influencers of the movement of particles and, consequently, to greater noise contained in the seismic record.

Conclusion

A new model of the regolith layer was presented, based on the arrival times of the P waves in 32 records of active seismic. The model created provides a new estimate of the regolith thickness in the range of 8.3 m and 10.4 m for the Apollo 14 and Apollo 16 stations, respectively. With an independent set of travel times in each station, other recent studies are confirmed, pointing out that in Apollo 16 the thickness of the regolith is thicker than in Apollo 14 site, also related to the presence of numerous craters in the area and its compositional characteristics (Highlands). The depths of the layers can vary by a few meters, the exact resolution being difficult to quantify, due to associated uncertainties such as location and timing errors, seismic heterogeneities that change amplitudes, or affect direction and dispersion in wave propagation,

as well as record numbers reasonably low. The results obtained were in agreement with previous and more recent works, with seismic and non-seismic data, being considered satisfactory. In all cases, the velocity increases with depth, according to publications on studies related to lunar regolith, gradually.

4.2 Paper 2

EARTH-MOON DEEP QUAKES TRIGGERED BY ORBITAL VARIABILITY
Villanova et al.
IN SUBMISSION

Villanova, L.S. - lyara.villanova@aluno.unb.br; http://lattes.cnpq.br/8444097347243654
Institute of Geosciences - University of Brasília (UnB) - Brazil, Brasilia, Federal District

The genesis of deep quakes on Earth and on the Moon challenges scientists for decades. Previous studies suggest that these deep quakes can be triggered by gravitational variability, i.e., tidal periodicity. Deep moonquakes, for example, have been associated with lunar orbital cyclicity. However, this relationship is still unclear once its hypocenters occur in deeper areas and may not be sensitive to tidal stress. On Earth, deep quakes occur close to the mantle transition zone and their origin is often associated with dehydration of lithospheric slabs. Also, the angle relation between the lunar apse parallel to the axis of rotation of the Earth has been associated with an increase in the number of large earthquakes, due to tidal stresses. Here, we correlate deep moonquakes and deep earthquakes with the main orbital parameters of the Sun-Earth-Moon system using machine learning and spectral approaches. Our results show that deep quakes are triggered by the movement of the Earth and the Moon in their own orbital plane. We found that deep seismicity arises from the orbital movements of Inclination of the lunar plane (IN), Longitude of Ascending Node (OM), True Anomaly (TA), and Argument of Perifocus (W). Deep quakes occur in specific seismic regions suggesting that event occurrence may be attributed to external factors to the planetary body. These results also suggest that the Earth and the Moon have specific layers with elastic behavior that respond seismologically in a similar way.

Earth-Moon centrifugal acceleration movement at the partial melting interface on Earth produces subsidence of Earth's lower mantle, disturbing the liquid outer core (Christensen, 2001; Carbone et al., 2020; Hsieh et al., 2020). This orbital relationship has been increasingly studied to better understand the terrestrial geodynamics and the associated seismicity (Kolvankar and Atomic, 2010; Zhao et al., 2012; Harada et al., 2014). Indeed, correlations between seismicity and lunar periods have been found using data from moonquakes or earthquakes (Allmann and Shearer, 2009; Frohlich and Nakamura, 2009; Gupta, 2012; Ide et al., 2016). However, these correlations are limited to specific orbital periods. Despite tidal stresses are considered shallow to control dynamic rupture processes related to deep earthquakes (Christensen, 2001; Ide et al., 2016; Kawamura et al., 2017; Watters et al., 2019; Passelègue et al., 2020; Zhan,

2020), their effects are usually correlated with periodic seismicity observed in deep moonquakes data (Frohlich and Nakamura, 2009; Weber et al., 2010; Gupta, 2012; Ide et al., 2016). Although these correlations are important in terms of seismological causalities, the seismic physical mechanism remains unknown.

Due to the propagation of seismic waves, the main information provided by deep moonquakes is related to the internal structure and rheology states of the Moon (Lognonné et al., 2003; Nakamura, 2005; Hao et al., 2018). Deep moonquakes probably have a non-tectonics origin, as the lunar lithosphere is immobile (Chen, 2018; Valantinas and Schultz, 2020), and the moonquakes are too deep to be related to it. Thus, even with increased surface stresses caused by tidal variability, another physical mechanism is needed to generate the moonquakes. Seismic events reflect an accumulation of energy and mass movement whose physical mechanism is related to the orbital movement of the body and its physical characteristics in the seismic band of the hypocenters (Weber et al., 2010; Watters et al., 2019). Mass movement depends on the physical property of the material, as both deep moonquakes and deep earthquakes are concentrated in specific structural ranges. Therefore, the mass movement can change the state of tension of the entire seismic band according to orbital movement and, therefore, cause quakes (Lognonné et al., 2003; Frohlich and Nakamura, 2009; Weber et al., 2010; Gupta, 2012; Harada et al., 2014; Ide et al., 2016; Valantinas and Schultz, 2020).

Although the mass movement depends on the amplitude of the orbital movement, previous studies focused only on the tidal stress and specific lunar periods (Frohlich and Nakamura, 2009; Gupta, 2012). The amplitude of the orbital movement increases during the maximum point of the body's Perifocus in its orbital plane. For the Moon this occurs in cycles of 6 years. Deep moonquakes can occur at pressures where a common fracture is not possible, with relatively low stresses, because the rock resistance is reduced by a fatigue process induced by tidal stress (Frohlich and Nakamura, 2009), and the number of major earthquakes may increase due to the lunar orientation parallel to the Earth's axis of rotation (Gupta, 2012). However, the relationship between the seismic events and orbital system remains unclear.

Considering that the Earth-Moon system is self-influencing, we investigated the possible effects of the amplitude of the orbital movement on the occurrence of quakes using deep moonquakes and earthquakes daily time series, and 13 orbital parameters, by wavelet analysis. The moonquakes time series was made compiling all the deep seismic events in the Apollo passive seismic catalog (JAXA - see on the Methods), and the earthquakes time series was made using the Wilber3 Tool (IRIS – on the Methods). Figure 4.10 shows the relationships between the time series of quakes and the correlation between them. The peaks, with the highest count of deep moonquakes per day (Figure 4.10a), occurred close to the moon's peak at its maximum point in orbit (in the middle of the years 1971 and 1977). The same pattern can also be observed in the deep earthquakes time series (Figure 4.10b). However, the deep moonquakes and deep earthquakes time series correlate over periods of days, months, and years (Figure 4.10c). The highest correlations occur in periods of approximately 8, 18 and 182 days. Deep moonquakes and deep earthquakes time series show that there is a phase correlation between seismic events and the precession period of the periapsis argument, i.e., the 6-yr period in the relation of the terrestrial and lunar orbital planes (Figure 4.10a and 4.10b).

The 166 epicenters of the lunar events with the latitudes, longitudes, and depths described

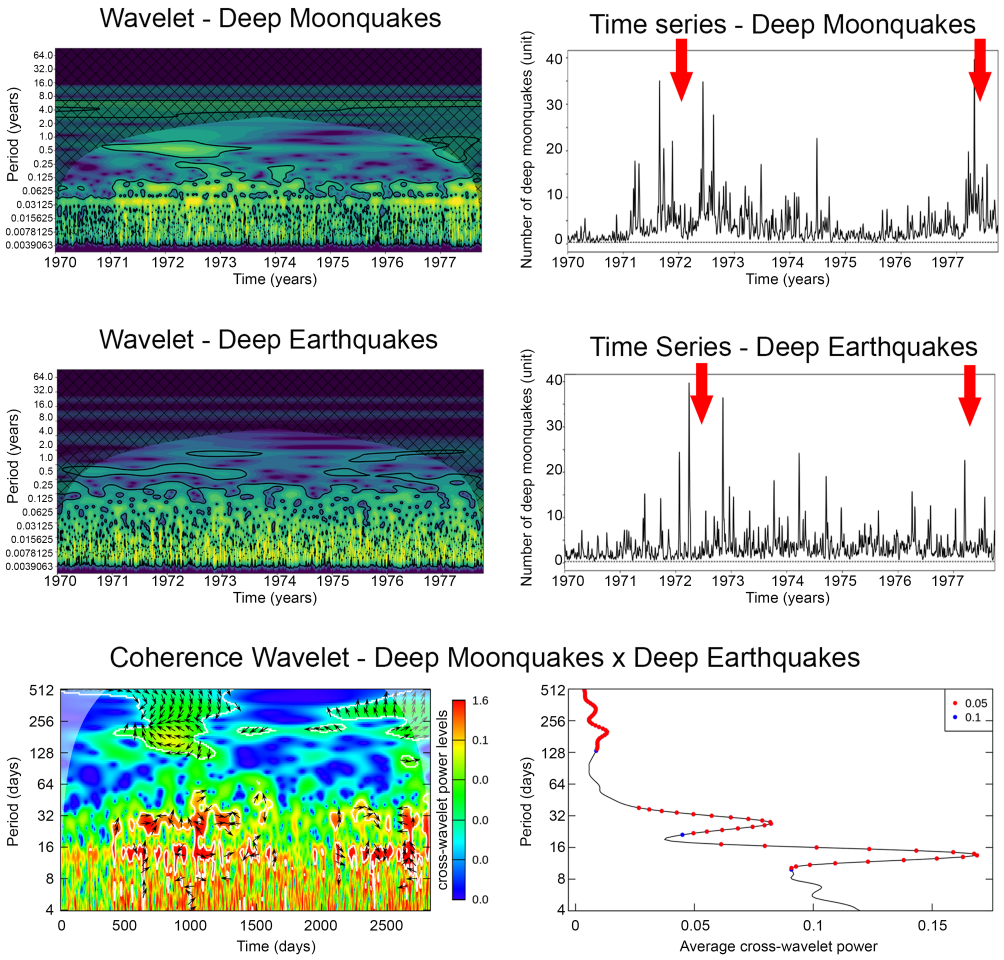

Figure 4.10 Cyclicity analysis of deep moonquakes and earthquakes. (a) Wavelets of deep moonquakes and (b) deep earthquakes time series with prominent peaks. (c) Coherence wavelet between deep moonquakes and deep earthquakes.

in the catalog, with different magnitudes, in general, <M2 (Figure 4.11c) presented an angular similarity with the angular relationships of the Sun-Earth-Moon system and the main orbital parameters (Figures 4.11a and 4.11b). We observed a correlation at approximately 8 and 18 days between the time series of deep moonquakes and deep earthquakes. These days correspond to the critical points of the Moon's orbit around the Earth (maximum and minimum points of the orbital plane and nodal points) (Figure 4.11a), represented by the smallest periods in the wavelet analysis (fewer quakes with a high frequency, Figure 4.10a). Spectral peaks of 182-day correspond to the extreme points of Earth's orbital plane around the Sun.

The occurrence of deep moonquakes is cyclical, as well as the orbital periods that interfere with the gravitational forces that act on the Earth-Moon system (Latham et al., 1972; Kolvankar and Atomic, 2010; Weber et al., 2010; Watters et al., 2019). Using wavelets applied to the deep quakes time series, we identified patterns and correlations among the parameters that act on the causal physical mechanism and the events, as well as delimiting the periods of the greatest influence on their occurrence. The model that inferred the concentrations of correlations among all parameters was made using machine learning, presenting an error of 4%.

The epicenters band distribution when added to perpendicular tension has a similar pattern of Moon angular variation, i.e., Earth's obliquity added lunar orbital inclination (Figure 4.11). The decrease in volume due to the rock mass contraction in the direction of tension is compensated by an increase in volume due to expansion in orthogonal directions (Figure 4.11c). In this compensation, the energy release occurs in a seismic band formed by its contraction angle and expansion, perpendicular to each other (Wiens, 2001; Amoruso and Crescentini, 2020). An inclination of the Moon's orbit (IN = 5.15°), in relation to the ecliptic plane, causes latitudinal vibrations, which generate essential forces for the dissipation of the orbital energy on the Moon (Figures 4.11a and 4.11b). This behavior tends to decrease the orbital eccentricity (EC) and the semi-major axis (A), while the torques exerted by the Earth tend to increase the same parameters on the Moon (Williams and Dickey, 2002; Williams and Boggs, 2015). Therefore, the orbital evolution of the Moon is intricately linked to the thermal state of the lunar interior and its selenodynamics (Christensen, 2001; Carbone et al., 2020; Hsieh et al., 2020). The presence of the partial melting zone in the lunar interior, then, is causally linked to the rate of dissipation and elasticity in its Mantle (Lognonné et al., 2003; Zhao et al., 2012; Harada et al., 2014; Kronrod et al., 2018; Hao et al., 2018; Watters et al., 2019), where deep moonquakes occur.

A body's reaction to applied forces is causally linked to the elastic characteristics of the environment and its ability to accumulate tension (energy) (Pernet-Fisher et al., 2019). This release of energy, in general, occurs through the quakes (Burmin et al., 2016; Watters et al., 2019). As rocks can readily deform inside the planets, it is a good approximation to consider the planets as being in a state of tension completely described by the dependence of depth pressure (Wiens, 2001; Amoruso and Crescentini, 2020).

By examining the number of occurrences of deep earthquakes according to epicenters' depths (Figure 4.12, in orange, on the left), and the deep moonquakes with the same configuration (Figure 4.12, in blue, on the right), we found that deep quakes both on Earth and on the Moon, occur with a periodic relationship (as seen in the wavelet analysis, Figure 4.10), concentrated in a specific seismic range in depth. This suggests that the terrestrial transition zone (approx. 410 - 660 km) and the lower lunar mantle (approx. 750 - 1250 km) have simi-

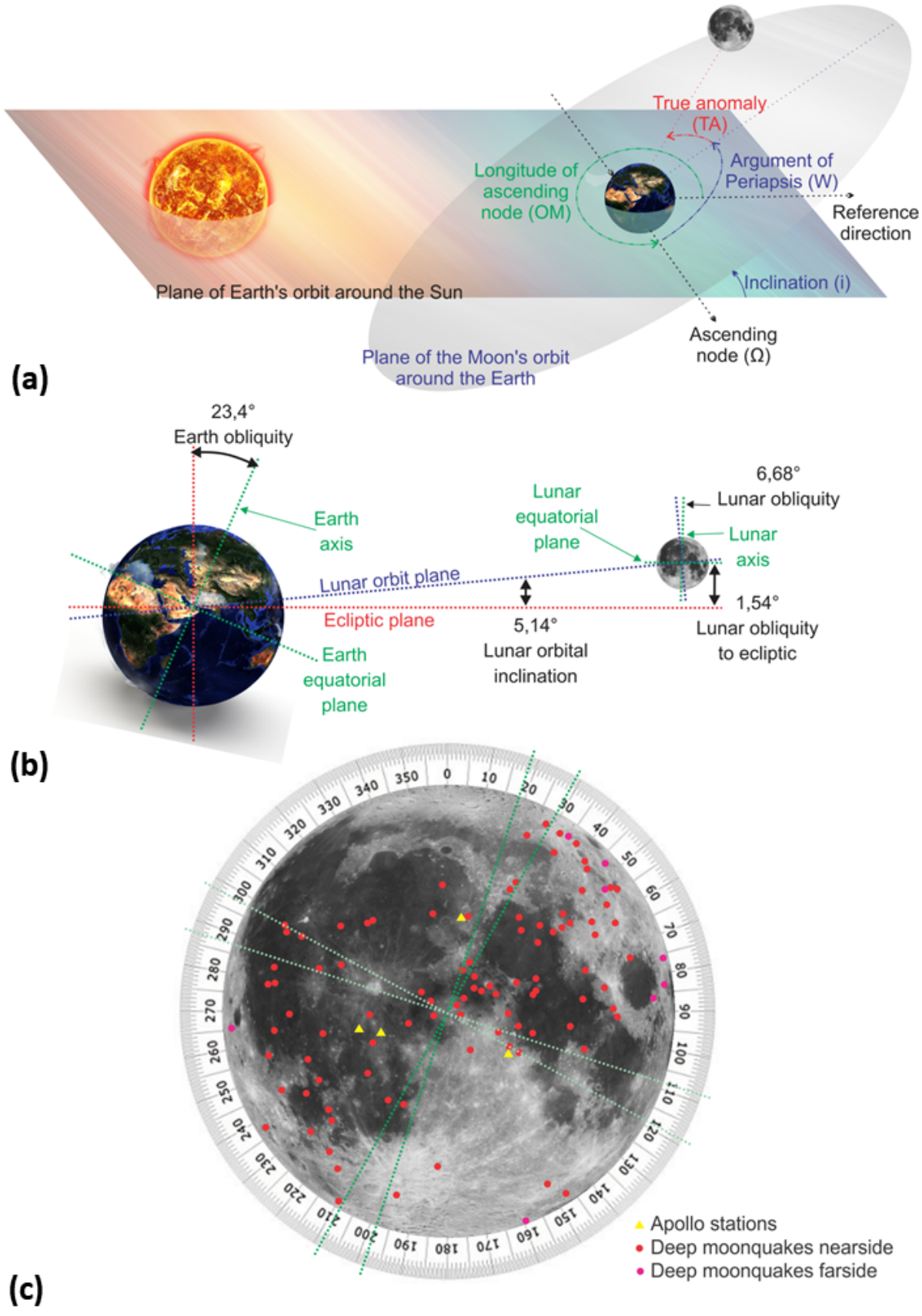

Figure 4.11 Relationship among orbital parameters and deep quakes. (a) Relevant parameters for correlation with deep earthquakes and deep lunar earthquakes. (b) Angular relations between Moon and Earth. (c) The epicenters of deep moonquakes and the relationship between the lunar seismic band and the angular variation suffered by the Moon (Earth obliquity + lunar orbital inclination).

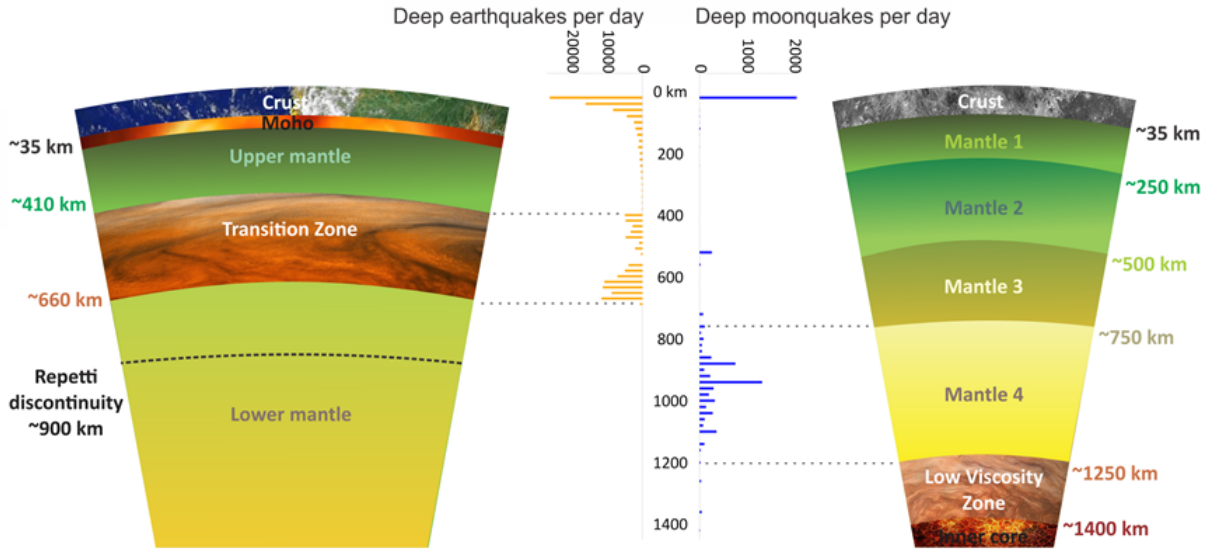

Figure 4.12 Occurrence of deep earthquakes according to the depth of the epicenters, in orange, and of deep moonquakes, in blue, related to their respective internal structures.

lar physical and mineralogical characteristics since they present the same behavior through the same physical causal mechanism. The fluid behavior of the Earth's mantle can be explained by solid-state flow processes, as in the transition zone. At lower levels of stress and temperatures, close to the solid rock, the dominant flow process is the diffusion of ions through the crystalline network (Wiens, 2001; Nédélec et al., 2017) that results in tension. Both the diffusion and displacement flows are thermally activated, as is the case of the lower lunar mantle, where deformation rates are inversely proportional to the temperature exponential (Wiens, 2001; Christensen, 2001; Maurice et al., 2017).

By mass conservation's principle, any change in volume of a body must be accompanied by a change in its density, in balance under the action of all forces and torques exerted on the body's area. The resulting shear tension acts on the cross-section of the plane normal to the layers of the internal structure, and a horizontal force is applied to the same layers. The sum of moments generates a liquid torque in the counterclockwise direction in the body, and the forces are separated, exerting a net torque on the body in a clockwise direction. The vertical force and the tensor moment are the result of the gravitational force of the body acting on the descending layer in its internal structure (Wiens, 2001; Williams and Boggs, 2015; Amoruso and Crescentini, 2020).

Seismic studies state that the lunar mantle is not liquid because it propagates shear waves (Lognonné et al., 2003; Nakamura, 2005; Hao et al., 2018). To have an elastic layer like the terrestrial transition zone, variations in rheology with depth are needed, but they depend on the rate of heat loss from the inner surface. Heat transfer occurs by molecular collisions, in which the molecules transmit kinetic energy by colliding with each other in a medium of spatial gradient temperature (Wiens, 2001; Maurice et al., 2017). Heat transfer by convection is associated with the movement of the medium (in this case, the orbital movement). Thus, the

total deformation of the body is the sum of the deformations associated with stress and those associated with temperature. The locations of deep earthquakes occurrence provide direct evidence of active mantle convection at depths around 660 km. As the lower mantle is expected to contain significant concentrations of radioactive isotopes, we presume that the mantle convection will occur in the lower mantle to transport the resulting heat, a mechanism that operates in the upper and lower terrestrial mantle, in the transition zone (Christensen, 2001; Maurice et al., 2017; Nédélec et al., 2017).

Earth's rotation and variations in internal lateral density promotes variations of the gravity's acceleration with location (celestial coordinates and their associated orbital parameters). As the gravitational field is conservative, the potential energy per unit of mass depends only on the position of the field and not on the path described by the mass. Thus, the deeper ductile-ruptile layers of the mantle in the Earth and in the Moon that present expansion/contraction behaviors may show changes in the local density. In fact, bodies with a radius less than 38 km can be dragged in the mantle flows, when these ductile-ruptile layers of the mantle suffer applied gravitational torque and move, in response to the orbital movement of the planetary body (Maurice et al., 2017; Nédélec et al., 2017). Therefore, the deep terrestrial and lunar seismicity is mostly derived from external forces of the planetary body in question.

Datasets

Apollo missions recorded moonquakes in different periods of time: Apollo 11 has data from 7/21/1969 to 8/3/1969 and between 8/19/1969 and 8/26/1969; Apollo 12 has data from 19 / 11/1969 to 09/30/1977; Apollo 14 has data from 02/05/1971 to 09/30/1977; Apollo 15 has data from 07/31/1971 to 09/30/1977; Apollo 16 has data from 04/21/1972 to 09/30/1977, and Apollo 17 with data from 03/01/1976 to 09/30/1977. Apollo 11 records are composed of non-continuous data, generating a gap in the deep moonquakes time series. For this reason, these data were discarded. Among all records, only events classified as "deep" were used, discarding all others. Due to the non-continuous nature of registration in 1969, the use of data from 01/01/1970 to 09/30/1977 (last day of registration of stations) was limited. In summary, the deep moonquakes time series consists of counting events classified as "deep" per day, for a total of 2830 days.

A time-series of deep earthquakes per day was also made during the same period. To make a time series of deep earthquakes, it considered all events with a hypocenter located at depths equal to or greater than 300 km. This data is available in "Wilber 3", Tool from IRIS (Incorporated Research Institutions for Seismology), with the following configuration: Date: 01/01/1970 - 09/30/1977; Magnitude: 0-10; Depth: 300-6371. Deep earthquakes and deep moonquakes occurrence and their depth dependence with epicenters were analyzed in Python scripts. All scripts and databases are available at Code availability.

Orbital parameters of the Moon-Earth-Sun system were calculated using NASA's HORIZONS software. For the calculation, the following configurations were used: Target Body: Moon [Luna] [code 301]; Mass Center: Earth-Moon Barycenter [code 500 @ 3]; Time Span: Start = 1970-01-01, Stop = 1977-09-29, Step = 1 day; Table Settings: output units = KM-S; TP type = RELATIVE. Each orbital parameter (A = Semi-major axis (km), AD = Apoapsis distance (km), EC = Eccentricity, IN = Inclination w.r.t XY-plane (degrees), JD = Julian Day

Number, Barycentric Dynamical Time, MA = Mean anomaly (degrees), N = Mean motion (degrees / sec), OM = Longitude of Ascending Node (degrees), PR = Sidereal orbit period (sec), QR = Periapsis distance (km), TA = True anomaly (degrees), Tp = Time of periapsis relative to epoch (sec), W = Argument of Perifocus (degrees) was arranged in a time series separately, composed of the value calculated in the respective units of each parameter per day.

Statistical analysis

Stationary character and/or trend of all seismic time-series were statistical analyzed. This statistical analysis was performed using the Action Stat software. For this first analysis, we conducted Mann-Kendall (trend test), and Dickey-Fuller (stationary test) statistical tests. In the Mann-Kendall test, the p-value obtained was 0.0294, indicating a non-null hypothesis at the significance level of 0.05 (the series' observations are independent and identically distributed). Therefore, we conclude that there is a significant trend if the statistic is less than 0.0294. In the Dickey-Fuller test, the p-value obtained was 0.01, indicating also a non-null hypothesis at the significance level of 0.05 (there is at least one root within the unit circle). Thus, we conclude that the data is stationary if the statistic is less than 0.01. We noticed that all parameters, except JD (Julian Day), are stationary, which implies that the orbital parameters and deep quakes reflect an occurrence with stable equilibrium, with its cyclically oscillating around their average in a relatively orderly behavior. The JD parameter has a non-stationary nature, since it is a count of days, with no fixed average over an infinite period or changing the analyzed period. The trend in the JD, OM, W, and deep moonquakes and deep earthquakes series is linked to a change in the medium level in the long run. In other words, the trend reflects the decline/increase in the average value of the long-term time series. So, before processing the data, the trend of the JD, OM, W, Deep Moonquakes, and Deep earthquakes series was removed and the non-stationarity of the JD series, using Python.

Data analysis

Wavelet Transform (WT) analysis was performed on all 15 parameters and was performed using a script using Python. The Wavelet Coherence (WC) analysis was performed only between the deep moonquakes and deep earthquakes' series, using R. Knowing that the deep moonquakes and deep earthquakes are correlated, all series (including orbital parameters) were grouped in a single database, normalized (since they have different physical quantities, such as km, km/sec, sec, degrees, degrees/sec, etc.) and analyzed using Machine Learning, in the Weka software, in order to detect which orbital relationships influence the occurrence of quakes. All possible ML models for numerical data were used. The closer the coefficient correlation to "1.0" and the closer to "0.0" the errors, the better the model's adequacy. Finally, the database was analyzed, still with ML, in the Weka software, in the attribute evaluator mode, to explain the percentage in which the parameters are related. The attribute evaluator was used in the CfsSubsetEval configuration.

Data availability

The data from the Apollo Seismographic Network are available in the "Technical Reports On Lunar Data", in the NASA directory, under constant review by Dr. Yosio Nakamura (Naka-

mura, 2008). To view the seismograms and make the seismic catalog, we used the Moon Seismic Monitor that is online software from JAXA (Japan Aerospace Exploration Agency), available at $https://www.darts.isas.jaxa.jp/planet/seismology/apollo/app/'$. The Moon Seismic Monitor shows characteristics of each event, such as the latitude and longitude of the hypocenters and depth of the epicenters, as well as their classification (shallow, deep, thermal, etc). This information in the JAXA directory was used to produce the lunar seismic catalog, adding up to 13,055 events in all. To make the earthquakes series, we used the"Wilber 3", a tool from IRIS (Incorporated Research Institutions for Seismology), available at '$http://ds.iris.edu/wilber3/find\_event'$ was used. The orbital parameters of the Moon-Earth-Sun system were calculated using NASA's HORIZONS software, available at: '$https://ssd.jpl.nasa.gov/horizons.cgi'$.

4.3 Paper 3

INFLUENTIAL ORBITAL VARIABILITY IN MOONQUAKES RECORDS
Villanova et al.
IN PREPARATION

Villanova, L.S. - lyara.villanova@aluno.unb.br; http://lattes.cnpq.br/8444097347243654
Institute of Geosciences - University of Brasília (UnB) - Brazil, Brasilia, Federal District

Abstract

The regolith under each Apollo station has been appointed as the main cause of noise in lunar seismological records. Particularly in the records of deep moonquakes, this noise makes it difficult to identify wave arrivals. In addition to the regolith layer that influences the velocity of waves' propagation, any ground movement below the station was detected due to station's sensitivity. Therefore, thermal expansion due to exposure of the surface to the Sun, diurnal variability, and surface variation derived from tidal stresses, meteoritic impacts, or even seismic wave propagation can influence on the noise increases. Here, we calculate the Fast Fourier Transform (FFT) and the Power Spectral Density (PSD) of deep quakes recorded when the Moon was at specific points in its orbit, where the angle was critical (0°, 90°, 180°, and 270°), for the horizontal components (x and y) and the vertical component (z) individually. We noticed that the z component presents greater noise since any ground movement below the station is more easily detected by the station's sensitivity, compared to external factors such as celestial movement. The horizontal components have greater noise when the Moon was at approximately 0° and 180° of its argument of periapsis, and the y component has a simple higher noise content compared to the x component. The horizontal y component is perpendicular to Earth and parallel to the direction of the lunar orbit. This suggests the noise may indicate a response to variation in location on the celestial plane (celestial coordinates and their associated orbital parameters). We conclude that, in addition to the characteristics of the regolith at each station location, sensors aimed at greater displacement variability are also more sensitive to recording noise derived from particle movements arising from thermal variability.

Introduction

Apollo's passive seismic experiments (PSE) were intended to provide information about the lunar interior (Latham et al., 1972). Although the PSE numerous information about the lunar internal structure, the lunar seismological data are restricted or biased due to sparse seismological network, weak sources, strong wave dispersion, and regolith noise, which impose limitations on knowledge about the Moon interior (Latham et al., 1972; Nakamura, 2005; Kawamura et al., 2017; Watters et al., 2019; Zhan, 2020).

To bypass these restrictions some studies have implemented techniques for identifying wave amplitude information and filtering these noisy records, identifying the seismic phases signal (Jarosch, 1977; Goins, 1978; Horvath, 1979). These techniques were satisfactory efficient to filter the noise attributed to local geology (i.e., regolith). However, others studies suggest that the occurrence of deep moonquakes is cyclical and forced by orbital variability (Frohlich and Nakamura, 2009; Weber et al., 2010; Kolvankar and Atomic, 2010; Gupta, 2012; Villanova et al., 2021b). This implies that not only the stations' location on the Moon interferes with the signal-to-noise frequency, but also the stations' location on the celestial plane. Therefore, the signal of the moonquakes, especially the deep ones, is affected by orbital variability (Villanova et al., 2021b).

In this contribution, we employ a signal-to-noise analysis on deep moonquakes that were recorded when the Moon was in specific orbital positions. The components of lunar seismograms were analyzed in terms of frequency and ground movement below the station. We compared these components to each other in order to verify possible dependencies of the characteristics of the signal with its position in the celestial plane, gravitational and/or thermal forces.

Background

Deep moonquakes are the most numerous types of seismic events on the Moon (Latham et al., 1972; Frohlich and Nakamura, 2009; Weber et al., 2010). Their occurrence correlates very well with the variation of tidal forces (Weber et al., 2010; Kolvankar and Atomic, 2010; Gupta, 2012; Villanova et al., 2021b). The waveforms of the records and the low coherence between the components of ground movement make the identification of arrivals very difficult. These arrivals are necessary to identify the discontinuities and velocity limits of the lunar interior. The main tool to identify secondary arrivals is the particle motion filter (Horvath, 1979). For this, it is necessary to obtain the ground movement from the signal. This process is called instrumental deconvolution, where the Fourier transform is used to calculate the impulse response, obtained as a solution of the equations of motion (Chakrabarty and Choudhury, 1964; Horvath, 1979; Williams and Boggs, 2015). Special attention must be paid to the effects of noise in determining seismograph parameters because the signal-to-noise ratio is quite small for most calibration pulses. High-frequency noise, which is caused by amplifier and transducer noise, does not affect the calculations because the instrumental response is low at high frequencies. Thus, the majority of the long-period noise is attributed to thermal noise (Jarosch, 1977; Horvath, 1979).

The simplest way to estimate the signal-to-noise ratio of a calibration pulse is to inspect

its phase spectrum. The phase spectra of the peak mode calibration pulses are oscillatory at frequencies above of 1.3 Hz. Near this frequency, the amplitude of the noise is approximately that of the signal (Horvath, 1979). Signals from deep moonquakes at stations 12 and 15 have smaller horizontal amplitudes than at stations 14 and 16. Since spectral amplitude ratios are dominated by noise at frequencies where signal amplitudes and instrumental sensitivities are low compared to the noise level, the apparent dependence of the source of the spectral ratios can be attributed to the use of less energetic signals, registered by the seismometers. Dispersion and coupling to the ground can also influence the spectral ratio. Horvath (1979) assigned the lower limit to the frequency band in which the long-period noise is small enough and is about 0.3 Hz for all stations. The upper limit is the frequency at which the horizontal-vertical spectral ratio becomes that of noise is about 2.3, 1.6, 2.1, and 1.7 Hz for stations 12, 14, 15, and 16, respectively.

Velocities are mainly characterized by a thin surface zone (attributed to the depth of the regolith), with a high-velocity gradient (Kovalch and Watkins, 1973; Parmentier et al., 2002; Watters et al., 2019). At older sites (Apollo 14 and 16) the average shear and compression velocities are lower, and the upper layers of the layered models are thicker than in the younger sites (Apollo 12 and 15) (Latham et al., 1972; Pernet-Fisher et al., 2019). Velocities are lower at location 16 than at other locations. Lower velocities at older sites may simply reflect longer exposure to meteoroid bombardment (Kovalch and Watkins, 1973; Horvath, 1979; Villanova et al., 2021a).

Methods

The Apollo missions recorded moonquakes in different periods among some stations, being Apollo 11 (between 21/07/1969 and 03/08/1969, between 19/08/1969 and 26/08/1969), Apollo 12 (between 19 /11/1969 and 9/30/1977), Apollo 14 (between 2/05/1971 and 9/30/1977), Apollo 15 (between 7/31/1971 and 9/30/1977), Apollo 16 (between 21/04/1972 and 30/09/1977) and Apollo 17 (between 01/03/1976 and 30/09/1977). Among all records, only events classified as "deep" were used, discarding all others. The orbital parameters of the Moon-Earth-Sun system were calculated using NASA's HORIZONS software. The following settings were used for the calculation: Target Body: Moon [Luna] [code 301]; Mass Center: Earth-Moon Barycenter [code 500@3]; Time Span: Start = 1970-01-01, Stop = 1977-09-30, Step = 1 day; Table Settings: output units = KM-S; TP type = RELATIVE. Each orbital parameter (IN = Inclination wrt XY-plane (degrees), JD = Julian Day Number, Barycentric Dynamical Time, OM = Longitude of Ascending Node (degrees), TA = True anomaly (degrees), W = Argument of Perifocus (degrees)) was arranged in a time series separately, composed of the value calculated in the respective units of each parameter per day. The same procedure was done for the registered deep moonquakes per day. Among the records of deep moonquakes, those that occurred when each parameter was approximately at 0°, 90°, 180°, and 270° were chosen. These angles were chosen because when the Moon is close to 0° and 180° in its orbit, it is passing through the ascending nodes, at 90° and 270º it is close to the lowest/higher point of the orbit in relation to the earth plane.

Fast Fourier Transform (FFT) analysis and 3D peak motion calculation were performed using Wave's software. For both, each event was imported into the software individually, but

the three components (x, y, and z) were imported and analyzed together. The graphics were exported from the software itself, changing only colors and font size. The spectrogram (PSD) analysis was done using Python, with the 'signal' command, from the Scipy module. For filtering, frequency band values of 0.03-3.0 for low pass and 0.8-3.0 for high pass were used.

Apollo Seismographic Network data is available in the IRIS directory at: *'http://ds.iris.edu/gmap/#network=XA&planet=moon'*, as no format data. Revised SEED data, with x, y, and z components, are available in Lunar Seismology: a data and instrumentation review - Electronic Supplement (Nunn et al., 2020) at *'https://zenodo.org/record/3560482#.%20YIHwyehKjIU/'*.

The orbital parameters of the Moon-Earth-Sun system were calculated using NASA's HORIZONS software, available at: *'https://ssd.jpl.nasa.gov/horizons.cgi'*.

Results and discussions

The present study was done using deep moonquakes, where the Moon was at 0°, 90°, 180°, and 270° in its orbit. The results were in full agreement with the values published by Horvath (1979) for spectral ratio in particle motion calculations but showed higher noise (high frequency in the signal) in events that occurred when the Moon was passing through the ascending nodes points of its orbit (0° and 180°), mainly in the z component.

Based on the results of Villanova et al. (2021a), we selected some deep moonquakes events that occur under specific orbital parameters (IN = Inclination XY-plane (degrees), OM = Longitude of Ascending Node (degrees), TA = True anomaly (degrees), W = Argument of Perifocus (degrees)). Events recorded at critical angles in each of these parameters, described in Table 1 (Figure 4.13), were chosen. For the IN parameter, events recorded at the smallest and largest angles that occurred during the operation of the stations were chosen. For TA and W, events registered at 0°, 90°, 180° and 270° of the orbits were chosen and for OM, only events registered at 0° and 270° were chosen, because the operating time of the stations is less than the time to complete the 360° of the orbit. The use of these points/angles is convenient to also capture the potential effects of lunar periods on the amplitude of noise in the records, which is often correlated with thermal (surface exposure to the Sun), diurnal variability, and tidal forces, where there is the occurrence of positive and negative peaks of high frequency and low signal amplitude.

The noise calculated at the stations show values of 2.21 Hz for Apollo 12 (Figure 4.14a), 1.93 Hz for Apollo 14 (Figure 4.14b), 2.04 Hz for Apollo 15 (Figure 4.14c), and 1.94 Hz for Apollo 16 (Figure 4.14d), where the signal frequency (high frequency) becomes noise, concomitant with the values of 2.3 Hz, 1.6 Hz, 2.1 Hz, and 1.7 Hz, respectively, published by Horvath (1979). This result shows that the location of the stations on the Moon, in fact, affects the signal noise, due to differences in the composition and depth of the regolith.

A more complete interpretation of the data is to analyze the frequency contained in each component individually, as each component has different influences and characteristics. For this, the PSD method was used to understand how the frequency band is changed and from which high frequency the signal becomes noise, according to these influences. This noise processing system is unique in that, there is no need to filter the data, as is commonly done in seismic noise analysis (McNamara and Boaz, 2005). In fact, examining artifacts related to station operation and episodic noise allows estimating overall station quality, and a baseline noise

IN	OM	TA	W	Number of events	Date	Julian Day
4.99197091	236.520677	159.5297542	294.496581	3	22/08/1975 – 15:50	2442646.5
5.30135088	269.002734	139.2941846	181.149437	1	21/12/1973	2442037.5
5.15385154	270.087508	250.080915	184.773257	2	06/11/1973 – 10:09	2441992.5
5.09562788	344.485655	238.7849707	327.931417	1	01/01/1970 – 01:40	2440587.5
5.20180233	232.684787	90.9423913	298.246892	2	10/10/1975 – 01:05	2442695.5
5.29067836	232.163944	180.001688	304.452818	1	14/11/1975 – 02:28	2442730.5
5.20507716	323.436629	270.1073143	47.5012629	1	21/03/1971	2441031.5
5.124305	288.241821	359.960494	131.360915	3	21/11/1972	2441642.5
5.25025146	305.721432	105.9595312	90.389737	2	04/01/1972 – 14:31	2441320.5
5.08256697	275.751636	123.932081	180.427816	3	02/09/1973	2441927.5
5.10767707	252.290571	291.791671	270.059689	2	08/10/1974 – 11:32	2442328.5
5.2884452	324.082621	43.46831132	359.286125	1	31/01/1971 – 06:07	2440982.5

Figure 4.13 Table 1 – List of analyzed events and their respective angles in each parameter. In yellow are the dates on which the events used were recorded, in extreme calculated values of IN (an acronym for the inclination of the orbital plane). In green, the dates and calculated values for OM (longitude of ascending node). In orange, dates, and values for TA (true anomaly), and in blue, dates, and values for W (Perifocus argument).

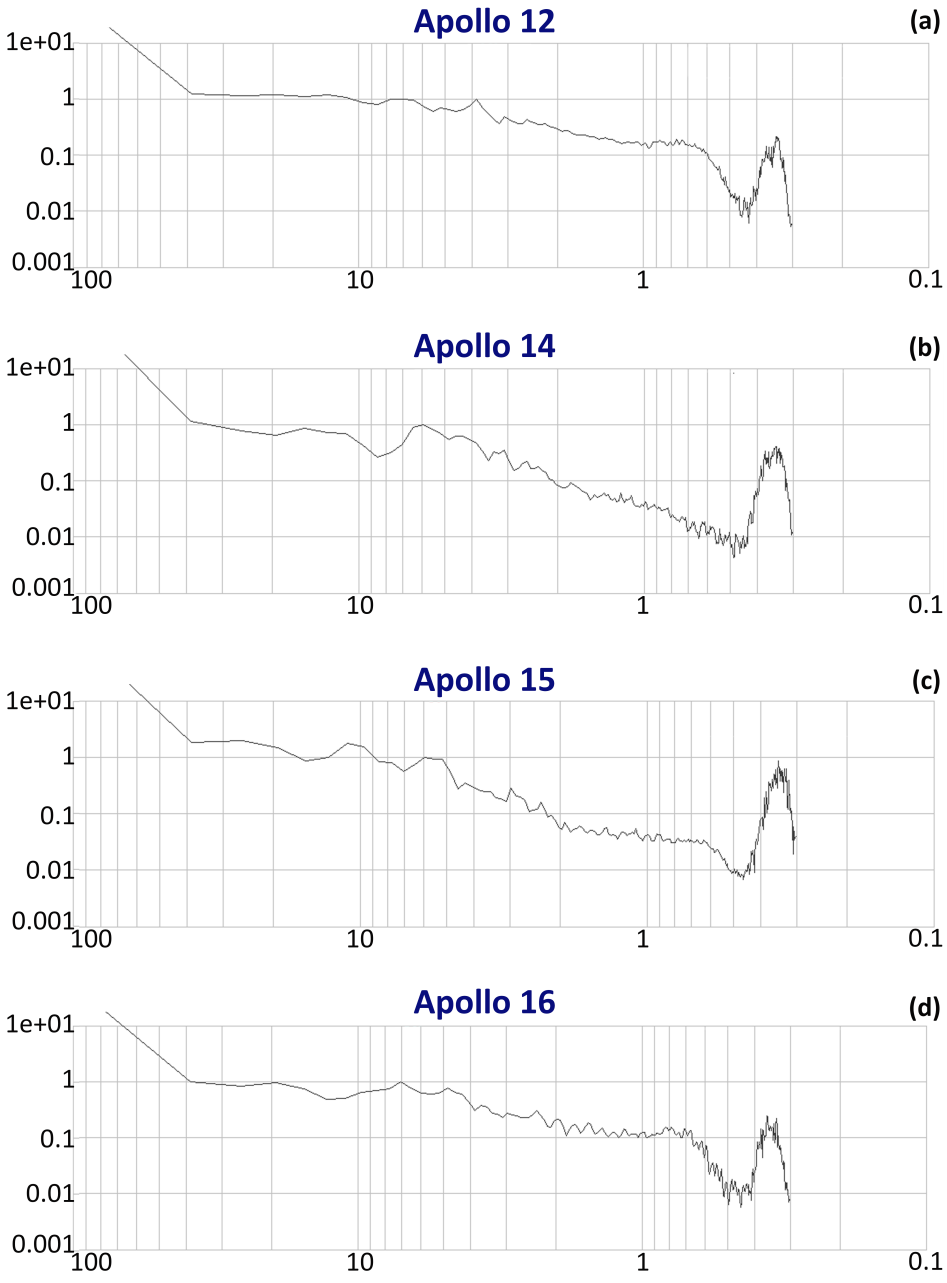

Figure 4.14 Signal-to-noise curve for (a) Apollo 12, (b) Apollo 14, (c) Apollo 15 and (d) Apollo 16.

level at each location. The noise analysis of this method differs from many noise studies because it no attempt to filter the continuous waveforms to eliminate surface waves or calibration pulses. These signals are included in the processing because they are low probability occurrences that do not contaminate the seismic noise. In fact, transient signals are often useful for evaluating station performance (Horvath, 1979; McNamara and Boaz, 2005). This approach is useful because stations exhibit considerable variations in noise levels as a function of time of day, season, location, and installation.

The way in which the celestial body reacts to applied forces is directly related to the elastic characteristics of the compositional materials and its capacity to accumulate efforts (Pernet-Fisher et al., 2019) whose energy release, in general, occurs through quakes (Burmin et al., 2016; Watters et al., 2019). However, most features of the recorded lunar seismograms were quite different from terrestrial seismograms. The long-term continuous reverberation, the onset of emergent body waves, the almost complete lack of correlation between components were explained by relatively low magnitudes and intensive scattering in the most superficial layer (i.e., regolith) (Chakrabarty and Choudhury, 1964; Houston et al., 1974; Lauderdale and Eichelman, 1974; Jarosch, 1977). Tension might change the frequency at which the signal becomes noise and must be different in each component since the Moon's position in the celestial plane is a three-dimensional coordinate (Horvath et al., 1980; Allmann and Shearer, 2009; Gupta, 2012; Williams and Boggs, 2015; Ide et al., 2016; Kawamura et al., 2017).

The spectrogram (PSD) of deep moonquakes recorded at station Apollo 12 when the Moon was at approximately 0°(Figure 4.15a), 90° (Figure 4.15b), 180° (Figure 4.15c), and 270° (Figure 4.15d) in its orbit around the Earth (parameter W). Only Apollo 12 data was used, as the other stations did not record events on these same dates. The fact that different events were recorded in the same station is very important, so there is no noise due to compositional differences and variations in the thickness of the regolith, the noise recorded being only derived from orbital/thermal factors. In all events, the vertical component z has a larger high-frequency band, where at approximately 1.5 Hz the signal becomes noise, regardless of the Moon's position. The horizontal components x and y present greater noise, also starting at approximately 1.5 Hz, when the Moon is positioned at the 0° and 180° angles of its orbit (Figure 4.17).

Since any change in amplitude must be accompanied by a change in density, a resulting shear force acts on the cross-section of the normal plane to the layer, and a horizontal force is applied to the layer (Parmentier et al., 2002; Williams and Boggs, 2015; Watters et al., 2019). The moments combine to generate an anticlockwise torque on the body. The forces are separated and apply torque on the body in a clockwise direction. The vertical force and tensor moment are the results of the gravitational force of the body acting on the descending layer (Allmann and Shearer, 2009; Williams and Boggs, 2015; Ide et al., 2016). As materials can contract and/or rupture on temperature changes, it is a good approximation to consider planetary bodies to be in a state of tension fully described by the distance between bodies and increased surface exposure to the Sun.

The analysis of the components of the records referring to the W parameter indicated that the vertical component z has a larger noise frequency band and that the horizontal components x and y present greater noise in positions equivalent to the ascending nodes (Figure 4.17). The same analysis was performed for all events described in Table 1 (Figure 4.13), to verify whether

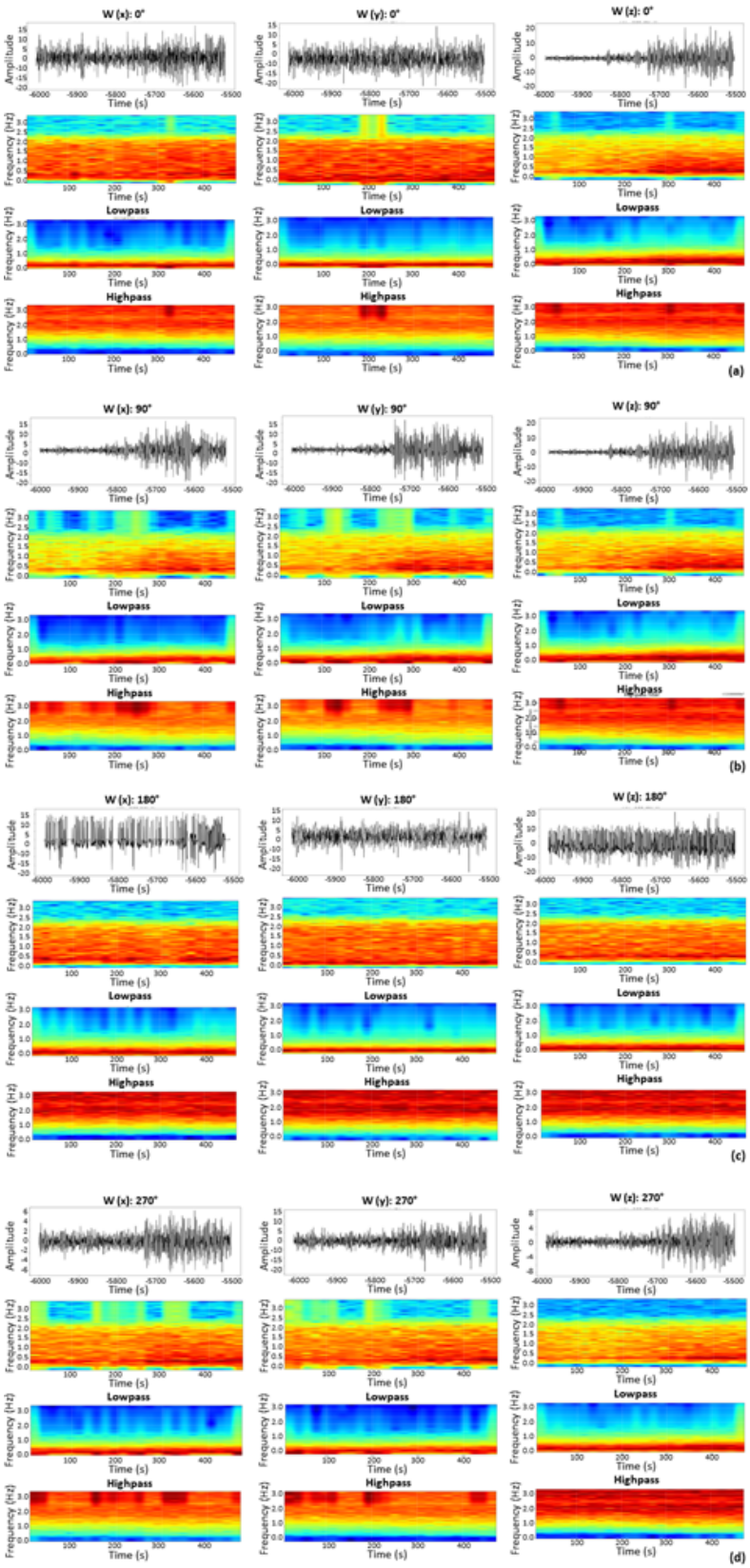

Figure 4.15 (a)Original event, spectrogram, low-frequency PSD and high-frequency PSD of the x, y and z components of the recorded event when W = 0°; (b) Original event, spectrogram, low-frequency PSD, and high-frequency PSD of the x, y and z components of the recorded event when W = 90°; (c) Original event, spectrogram, low-frequency PSD and high-frequency PSD of the x, y and z components of the recorded event when W = 180° and (d) Original event, spectrogram, low-frequency PSD and high-frequency PSD of the x, y and z components of the event logged when W = 270°.

the position in the celestial plane influences the noise contained in the record. The result can be seen below, in Table 2 (Figure 4.16).

In general, in all parameters and their respective angles, the vertical component presented lower frequency values in which the signal becomes noise or is predominantly contained by it. This may be mostly related to the regolith layer just below the station, as it is a layer of high energy dispersion of seismic waves and signal scattering. Similar compression velocities between 92 and 119.8 m/s were obtained for the regolith, by analyzing data from active seismic experiments, at the Apollo 14 and 16 sites (Kovalch and Watkins, 1973; Cooper et al., 1974; Lauderdale and Eichelman, 1974; Villanova et al., 2021a), of different thicknesses at different locations (between 8.3 and 8.5 m for Apollo 14 and 10.4 and 12.2 m for Apollo 16), and compression velocities of around 300 m/s for the underlying material in both seasons. This implies that these differences in wave propagation velocity, differences in thickness, and also differences in the shape of the layer directly influence the recording of the vertical sensor (z), since any movement in the ground just below the station (either due to thermal expansion and diurnal variability or variation derived from tidal forces, impacts or even wave propagation) will be more easily detected by the sensitivity of the station, compared to external factors such as celestial motion.

In the results shown in Table 2 (Figure 4,16), the horizontal components x and y seem to present, in general, greater noise at stations 12 and 15 and in events recorded when the Moon was approximately at 0° and 180° angles of the parameters that describe elliptical movements of 360°. In figure 4.17 it is also possible to observe in the FFT, applied directly to the signal (events of parameter W, recorded in Apollo 12, previously analyzed in Figure 4.15), the y component has a higher noise content compared to the x component. The horizontal y component is perpendicular to Earth but parallel to the direction of the orbit. This increase in noise may then indicate a direct response to variation in location, since, because of the Earth's rotation and internal lateral density variations, the acceleration of gravity, and hence of the force applied on all points on the surface, differs with location (celestial coordinates and their associated orbital parameters).

Conclusions

As the gravitational field is conservative, the potential energy per unit of mass depends only on the position in the field. The lunar mantle layers, where deep moonquakes occur, show dilation/contraction behavior and local density changes, when they suffer application of gravitational torque, in response to their orbital motion. Therefore, the deep lunar seismicity is, for the most part, derived from external forces of the planetary body, additionally to the pressure and temperature conditions of the mantle layers. The physical principle that occurs on the lunar surface also comes from orbital influences, but it is related to thermal conditions on the surface, due to greater or lesser exposure to the Sun, resulting from the Moon's position in orbit. Therefore, in addition to the geological context at each station site, sensors aimed at greater variability of displacement on the Moon in the plane are also more sensitive to record noise, derived from particle movements arising from thermal variability.

	IN (componente x)	IN (componente y)	IN (componente z)	
Apollo 12	1.7	1.5	1.6	~5°
Apollo 14	2.5	2.6	1.5	
Apollo 15	2.5	1.5	1.6	
Apollo 16	2.4	2.4	2.6	~5.3°

	OM (componente x)	OM (componente y)	OM (componente z)	
Apollo 12	2.4	2.5	1.2	~345°
Apollo 14	2.3	2.5	1.4	~270°
Apollo 16	2.5	2.4	2.3	

	TA (componente x)	TA (componente y)	TA (componente z)	
Apollo 12_3	2.4	2.3	2.4	~0°
Apollo 15	1.5	2.2	1.6	
Apollo 16	2.4	2.2	1.6	
Apollo 12_4	2.5	2.3	2.3	~90°
Apollo 16	2.4	2.4	1.8	
Apollo 12_5	-	-	-	~180°
Apollo 14	2.4	2.3	2.3	~270°

	W (componente x)	W (componente y)	W (componente z)	
Apollo 12_3	1.6	2.4	1.5	~0°
Apollo 12_1	2.3	2.3	1.6	~90°
Apollo 14_3	2.4	2.4	1.5	
Apollo 12_5	1.6	1.4	1.5	~180°
Apollo 14_1	2.5	1.6	1.6	
Apollo 15	1.5	1.5	1.6	
Apollo 12_7	2.4	2.3	1.5	~270°
Apollo 16	2.4	2.1	2.3	

Figure 4.16 Table 2 - Frequency values where the signal becomes noise, for all events in Table 1.

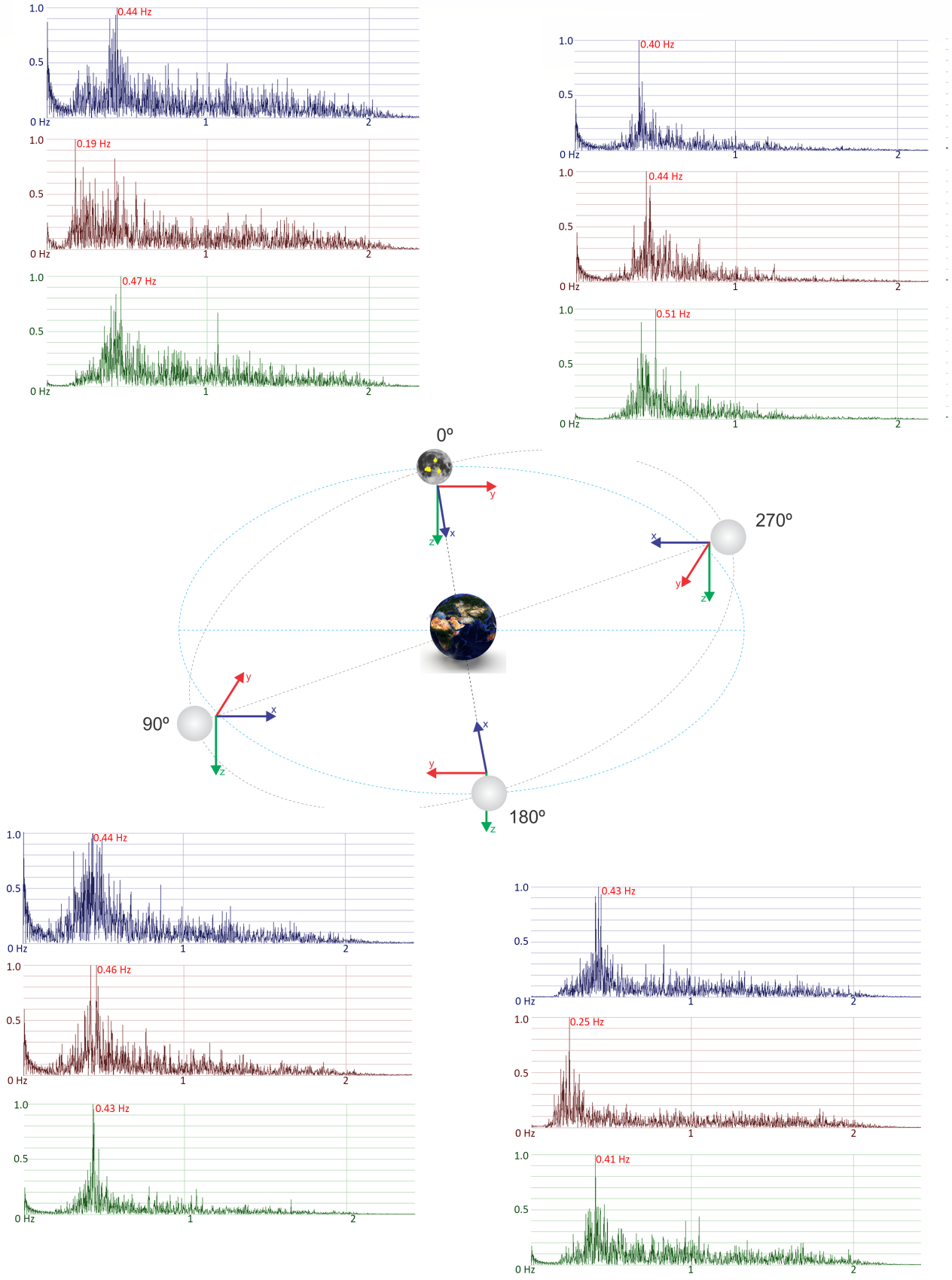

Figure 4.17 Diagram of the lunar orbit and the direction of components in the celestial plane. The FFT plotted are the same events in Table 1, for parameter W, recorded in Apollo 12.

CHAPTER 5

Conclusions

The most accepted hypothesis of the origin of the Moon was where a planetary body the size of Mars collided with the Earth, 4.5 billion years ago. The impact sent materials from the Earth and the body through space, and part of them joined together, forming the Moon. This formation and evolution of the Moon brought a fractional crystallization that resulted in the deposition of mafic minerals in the mantle and in the rising concentration of plagioclase in the crust, followed by a concentration of KREEP materials in the last crystallization zones.

In the Earth-Moon relationships, the gravitational one is the most important, controlling from the fluid movement at the mantle-core boundary to the position of the orbital axis. The effects of tidal forces are caused by the Earth's orbital motion around its axis, which is faster than the Moon in its orbit. The friction resulting from this tug of war forces the Moon into a wider orbit, and the interaction of these Forces causes the effects of a solid-body tide, which affects the Moon's gravitational torque and its orientation in space.

Earth-Moon centrifugal acceleration movement at the partial melting interface on Earth produces subsidence of Earth's lower mantle, disturbing the liquid outer core. Indeed, correlations between seismicity and lunar periods have been found using data from deep moonquakes or deep earthquakes. However, these correlations are limited to specific orbital periods. Due to the propagation of seismic waves, the main information provided by deep moonquakes is related to the internal structure and rheology states of the Moon, and both deep moonquakes and deep earthquakes are concentrated in specific structural ranges.

The elastic characteristics of the solid material are directly linked to the material's ability to accumulate tensions and release the accumulated energy that, in general, occurs through quakes. Thus, studying quakes and their forms of occurrence can help to better understand the cause and effect relationships in the Earth-Moon system, since, proportionally, what happens on the Moon also occurs on Earth, according to the physical laws of action and reaction. However, some questions about the deeper lunar seismicity are still under debate, such as the mechanism that generates these deep moonquakes, the frequency of their occurrence, and the frequency of the locations of the epicenters.

For this reason, this research aimed the main objective of reinterpreting data from lunar seismology to refine the understanding of the physical causal mechanism of deep moonquakes and their cyclicity of occurrence. The research also aimed three special objectives, that were developed in three papers, being: to analyze the depth and shape of the lunar regolith layer below the stations, which strongly influences the noise recorded in the seismograms; to understand the causality and cyclicality in the occurrence of deep moonquakes; and correlate the causality of events with geological and orbital mechanisms.

Considering that the Earth-Moon system is self-influencing, we investigated the possible

effects of the amplitude of the orbital movement on the occurrence of quakes. The highest correlations occur in periods of approximately 8, 18, and 182 days. Deep moonquakes and deep earthquakes time series show that there is a phase correlation between seismic events and the precession period of the periapsis argument, i.e., the approximate 6-yr period in the relation of the terrestrial and lunar orbital planes.

In addition, the regolith layer influences the velocity of waves propagation, and also a thermal expansion due to exposure of the surface to the Sun, diurnal variability, and surface variation derived from tidal stresses, meteoritic impacts, or even seismic wave propagation can influence the recorded noise at the lunar seismograms.

In general, the vertical z component presents greater noise, since any ground movement below the station will be more easily detected by the station's sensitivity, compared to external factors such as celestial movement. The horizontal components seem to have greater noise when the Moon was at approximately 0° and 180° (W orbital parameter), and the y component has a higher noise content compared to the x component. The horizontal y component is perpendicular to Earth and parallel to the direction of the lunar orbit. This suggests the noise may then indicate a response to variation in location on the celestial plane (celestial coordinates and their associated orbital parameters).

APPENDIX A

Appendix

Appendix I - Moon/Earth comparison

Data available at: $https://nssdc.gsfc.nasa.gov/planetary/factsheet/moonfact.html$

Table A.1 Bulk parameters.

	Moon	Earth	Ratio (Moon/Earth)
Mass ($10^{24}kg$)	0.07346	5.9724	0.0123
Volume ($10^{10}km^3$)	2.1968	108.321	0.0203
Equatorial radius (km)	1738.1	6378.1	0.2725
Polar radius (km)	1736.0	6356.8	0.2731
Volumetric mean radius (km)	1737.4	6371.0	0.2727
Ellipticity (Flattening)	0.0012	0.00335	0.36
Mean density (kg/m^3)	3344	5514	0.606
Surface gravity (m/s^2)	1.62	9.80	0.165
Surface acceleration (m/s^2)	1.62	9.78	0.166
Escape velocity (km/s)	2.38	11.2	0.213
GM ($*106km^3/s^2$)	0.00490	0.39860	0.0123
Bond albedo	0.11	0.306	0.360
Geometric albedo	0.12	0.434	0.28
V-band magnitude V(1,0)	-0.08	-3.99	-
Solar irradiance (W/m^2)	1361.0	1361.0	1.000
Black-body temperature (K)	270.4	254.0	1.065
Topographic range (km)	13	20	0.650
Moment of inertia (I/MR^2)	0.394	0.3308	1.191
J2 ($*10^{-6}$)	202.7	1082.63	0.187

LUNAR ATMOSPHERE
Diurnal temperature range (equator): 95 K to 390 K (-290 F to +240 F)
Total mass of atmosphere: 25,000 kg
Surface pressure (night): 3 x 10-15 bar (2 x 10-12 torr)
Abundance at surface: 2 x 105 particles/cm3

.
Estimated Composition (night, particles per cubic cm):
Helium 4 (4He) - 40,000 ; Neon 20 (20Ne) - 40,000 ; Hydrogen (H2) - 35,000
Argon 40 (40Ar) - 30,000 ; Neon 22 (22Ne) - 5,000 ; Argon 36 (36Ar) - 2,000
Methane - 1000 ; Ammonia - 1000 ; Carbon Dioxide (CO2) - 1000
Trace Oxygen (O+), Aluminum (Al+), Silicon (Si+)
Possible Phosphorus (P+), Sodium (Na+), Magnesium (Mg+)
.

Composition of the tenuous lunar atmosphere is poorly known and variable, these are estimates of the upper limits of the nighttime ambient atmosphere composition. Daytime levels were difficult to measure due to heating and outgassing of Apollo surface experiments.

Table A.2 Orbital parameters (for orbit about the Earth).

	Moon
Semimajor axis (106 km)	0.3844
Perigee (106 km)*	0.3633
Apogee (106 km)*	0.4055
Revolution period (days)	27.3217
Synodic period (days)	29.53
Mean orbital velocity (km/s)	1.022
Max. orbital velocity (km/s)	1.082
Min. orbital velocity (km/s)	0.970
Inclination to ecliptic (deg)	5.145
Inclination to Earth equator (deg)	18.28 - 28.58
Orbit eccentricity	0.0549
Sidereal rotation period (hrs)	655.728
Obliquity to orbit (deg)	6.68
Recession rate from Earth (cm/yr)	3.8

* These represent mean apogee and perigee for the lunar orbit, and were used for calculating the maximum and minimum velocities. The orbit changes over the course of the year so the distance from the Moon to Earth roughly ranges from 357,000 km to 407,000 km, giving velocities ranging from 1.100 to 0.966 km/s.

Appendix II - NASA Missions

Data avaliable at: "Lunar Constants and Models Document", from Ralph B. Roncoli. September 23, 2005. JPL Technical Document D-32296.

Link to download: $https://ssd.jpl.nasa.gov/dat/lunar_cmd_2005_jpl_d32296.pdf$

1. Lunar Exploration Mission Summary

The majority of the data presented in this section were extracted from the Lunar Exploration Timeline compiled by the NASA National Space Science Data Center (NSSDC). The list of missions summarized in Appendix only includes those missions that are known to have (or possibly have) deposited terrestrial material (whether intended or not) onto the surface of the Moon. This includes lunar orbiters whose orbit lifetimes have (or are believed to have) expired (i.e. the orbiters crashed into the surface of the Moon).

1.1. Soviet Luna Probes

The Luna series of unmanned probes included the first to fly by the Moon and photograph the farside of the Moon, the first to impact the Moon, the first to soft land and return photographs, the first robotic sample return (which occurred after the manned Apollo 11 and Apollo 12 had already returned their lunar samples), and the first to deploy a remotely-controlled rover (listed in the Table A.3).

1.2 U.S. Ranger Probes

The Ranger series included both probes which impacted the Moon at high velocity, returning images with increasing resolution up to the moment of impact, and "hard landers" which fired a braking motor at the last moment, dropping an instrument package protected by a balsa wood spherical shock absorber. The early Ranger missions were plagued by problems – the first successful mission was Ranger 7 in 1964. None of the hard landers succeeded. The three successful missions were all imaging impact probes. Ranger 8 flew a direct-in trajectory toward Mare Tranquillitatis, the Sea of Tranquility, providing the first close-up views which indicated the surface was smooth enough for the Apollo Lunar Module to land there (listed in the Table A.4).

1.3. U.S. Surveyor Landers

The Surveyor soft landers proved the lunar surface was sufficiently flat and strong to allow the Apollo Lunar Module to land. (Prior to the soft landings by Luna 9 and Surveyor 1 in 1966, some believed that the Moon was covered by a deep sea of dust which would be unable to support the weight of a lander – i.e. any landed vehicle would sink beneath the surface.) The Surveyor probes were equipped with steerable cameras which provided panoramic views of their landing sites. Later Surveyors carried a robotic scoop which could excavate soil, move rocks, and deposit soil into instruments for analysis, which provided the first in-situ data about the composition of the lunar regolith (listed in the Table A.5).

Table A.3 Launch222

Mission	Mission Type	Date
Luna 2	Impact	12 Sep 1959
Luna 5	Lander	9 May 1965
Luna 7	Lander	4 Oct 1965
Luna 8	Lander	3 Dec 1965
Luna 9	Lander 31	Jan 1966
Luna 10	Orbiter	31 Mar 1966
Luna 11	Orbiter	24 Aug 1966
Luna 12	Orbiter	22 Oct 1966
Luna 13	Lander	21 Dec 1966
Luna 14	Orbiter	7 Apr 1968
Luna 15	Sample Return	13 Jul 1969
Luna 16	Sample Return	12 Sep 1970
Luna 17	Rover	10 Nov 1970
Luna 18	Lander	2 Sep 1971
Luna 19	Orbiter	28 Sep 1971
Luna 20	Sample Return	14 Feb 1972
Luna 21	Rover	8 Jan 1973
Luna 22	Orbiter	29 May 1974
Luna 23	Sample Return	28 Oct 1974
Luna 24	Sample Return	9 Aug 1976

1.4. U.S. Lunar Orbiters

The Lunar Orbiter program consisted of five Lunar Orbiters which returned photography over 99% of the lunar surface (near and farside) with a resolution, in some images, down to 1 meter. All together the Orbiters returned 2180 high resolution and 882 medium resolution frames. The micrometeoroid experiments recorded 22 impacts showing the average micrometeoroid flux near the Moon was about two orders of magnitude greater than in interplanetary space but slightly less than the near-Earth environment. The radiation experiments confirmed that the design of Apollo hardware would protect the astronauts from average and greater-than-average short-term exposure to solar particle events. The Lunar Orbiters were all eventually commanded to crash on the Moon before their attitude control gas ran out so they would not present navigational or communications hazards to later Apollo flights (listed in the Table A.6).

1.5. U.S. Apollo Manned Lunar Landings

The Apollo manned lunar landings returned more than 380 kilograms of samples from a variety of lunar terrain types and emplaced instrument packages which performed measurements long after the astronauts had left. Seismometers allowed studying the lunar interior, both from

Table A.4 Launch

Mission	Mission Type	Date	Remarks
Ranger 4	Impact	23 Apr 1962	Computer failure. Impacted far-side of Moon.
Ranger 6	Impact/Photo	30 Jan 1964	Camera system failure. No images returned.
Ranger 7	Impact/Photo	28 Jul 1964	Transmitted 4,308 photographs (17 minutes of flight).
Ranger 8	Impact/Photo	17 Feb 1965	Transmitted 7,137 photographs (23 minutes of flight).
Ranger 9	Impact/Photo	21 Mar 1965	Transmitted 5,814 photographs (19 minutes of flight).

Table A.5 Launch

Mission	Mission Type	Date	Remarks
Surveyor 1	Lander	30 May 1966	Operated until 7 Jul 1966.
Surveyor 2	Lander	20 Sep 1966	Impacted the Moon.
Surveyor 3	Lander	17 Apr 1967	Spacecraft lifted off the surface before engines shut down.
Surveyor 4	Lander	14 Jul 1967	Lost contact approximately 2.5 minutes before touchdown.
Surveyor 5	Lander	8 Sep 1967	First in-situ chemical soil analysis.
Surveyor 6	Lander	7 Nov 1967	Engines were restarted after landing lifting the vehicle.
Surveyor 7	Lander	7 Jan 1968	Operated 80 hours past sunset on first lunar day.

response to natural moonquakes and impacts from spent Saturn IV-B stages (that boosted the Apollo spacecraft to the Moon) and Lunar Module ascent stages (jettisoned in lunar orbit) that were deliberately crashed into the Moon. Laser retroreflectors left by Apollo missions remain in use today, providing data for research in topics ranging from dynamics of the Earth-Moon system to tests of general relativity (listed in the Table A.7).

1.6 Other Lunar Orbiting Missions
Listed in the Table A.8.

2. Site Coordinates of Apollo Surface Mission Elements and Lunokhod 2 Rover
Listed in the Table A.9.

Notes:

• In this table the list of Apollo artifacts left on the surface of the Moon only includes the major surface mission elements and does not include things like American flags, seismic mortars, discarded items, and personal artifacts (e.g. pictures, plaques, Alan's Shepard's golf balls, etc.).

• Site coordinates are expressed in the IAU/IAG mean Earth / rotation system.

• Acronyms

Table A.6 Launch

Mission	Mission Type	Date	Remarks
Lunar Orb 1	Orbiter	10 Aug 1966	Initial period 208.1 min, IN 12 deg, EC 0.33.
Lunar Orb 2	Orbiter	6 Nov 1966	Initial period 208.07 min, IN 11.9 deg, EC 0.35.
Lunar Orb 3	Orbiter	5 Feb 1967	Initial period 208.1 min, IN 20.9 deg, EC 0.33.
Lunar Orb 4	Orbiter	4 May 1967	Initial period 721 min, IN 85.5 deg, EC 0.28.
Lunar Orb 5	Orbiter	1 Aug 1967	Initial period 510.08 min, IN 85 deg, EC 0.26.

Table A.7 Launch

Mission	Mission Type	Date	Remarks
Apollo 11	Manned/Lander	16 Jul 1969	First humans to step foot onto another celestial body.
Apollo 12	Manned/Lander	14 Nov 1969	First recorded artificial moonquake.
Apollo 14	Manned/Lander	31 Jan 1971	Traverse distance 3.45 km. Sample return 42.9 kg.
Apollo 15	Manned/Lander	26 Jul 1971	LRV explored regions within 5 km of the landing site.
Apollo 16	Manned/Lander	16 Apr 1972	LRV explored regions within 4.5 km of the landing site.
Apollo 17	Manned/Lander	7 Dec 1972	Last mission to carry humans. 7.5 km of the landing site.

LRRR: Lunar laser Ranging RetroReflector, PSEP: Passive Seismic Experiment Package [Note: The combination of the Apollo 11 LRRR and PSEP were referred to as the EASEP – Early Apollo Scientific Experiment Package].

LM: Lunar Module (Descent Stage), ALSEP: Apollo Lunar Surface Experiment Package

MET: Modularized Equipment Transporter, LRV: Lunar Roving Vehicle

• The ALSEP locations in this table really just indicate the location of the antenna on the ALSEP central station. The layout or configuration of ALSEP components on the surface of the Moon differed substantially for each Apollo mission (as did many of the components themselves). For example, the Radioisotope Thermoelectric Generators (RTGs) that powered the ALSEP investigations were generally located only about 3m from the central station, but the placement of some of the seismic sensors (geophones), for a few of the Apollo missions, extended out to a range of approximately 90 m from the ALSEP central station. For more information on the deployment configuration of the Apollo ALSEP investigations see Reference 36.

• Reference 37 indicates the results of an analysis performed by E. M. Jones using photographs taken by the Apollo 15, 16, and 17 astronauts of the LMs from the LRVs in their final, parked positions and photographs of the parked LRVs taken from the LMs to estimate the final positions of the LRVs relative to the LMs.

Table A.8 Launch

Mission	Mission Type	Date	Remarks
Explorer 35	Orbiter	19 July 1967	U.S. spacecraft also known as IMP-6.
Explorer 49	Orbiter	4 July 1968	U.S. spacecraft also known as RAE-2 (or RAE-B).
Hiten	Orbiter	24 Jan 1990	Japanese satellite originally called MUSES-A.
Hagoromo	Orbiter		Sub-satellite deployed from Hiten on 18 March 1990.
Lunar Prospector	Orbiter	7 Jan 1998	U.S. spacecraft to study the Moon.

Table A.9 Launch

Mission element	Latitude (degree)	East Longitude (degree)	Radius (km)
Apollo 11			
LRRR	0.67337	23.47293	1735.472
PSEP	0.67322	23.47299	
LM (Eagle)	0.67408	23.47297	
Apollo 12			
ALSEP	-3.00942	336.57542	1736.014
LM (Intrepid)	-3.01239	336.57843	
Apollo 14			
LRRR	-3.64421	342.52120	1736.335
ALSEP	-3.64398	342.52252	1736.343
LM (Antares)	-3.64530	342.52864	
MET	-3.64530	342.52864	
Apollo 15			
LRRR	26.13333	3.62837	1735.476
ALSEP	26.13407	3.62981	1735.477
LM (Falcon)	26.13222	3.63386	
LRV	26.13110	3.63972	
Apollo 16			
ALSEP	-8.97537	15.49812	1737.453
LM (Orion)	-8.97301	15.50019	
LRV	-8.97292	15.50279	
Apollo 17			
ALSEP	20.19209	30.76492	1734.814
LM (Challenger)	20.19080	30.77168	
LRV	20.19043	30.77726	
Luna 21 – Lunokhod 2 Rover			
LRRR	25.83223	30.92201	1734.638

Appendix III - Orbital Parameters

.
****
Revised: July 31, 2013 Moon / (Earth)
****
GEOPHYSICAL DATA (updated 2018-Aug-15):
.
Vol. mean radius, km = 1737.53+-0.03
Mass, $*10^{22} kg$ = 7.349
Radius (gravity), km = 1738.0
Surface emissivity = 0.92
Radius (IAU), km = 1737.4
GM, $\frac{km^3}{s^2}$ = 4902.800066
Density, $\frac{g}{cm^3}$ = 3.3437
GM 1-sigma, $\frac{km^3}{s^2}$ = +-0.0001
V(1,0) = +0.21
Surface accel., $\frac{m}{s^2}$ = 1.62
Earth/Moon mass ratio = 81.3005690769
Farside crust. thick., km = 80 - 90
Mean crustal density, $\frac{g}{cm^3}$ = 2.97+-.07
Nearside crust. thick., km = 58+-8
Heat flow, Apollo 15, $\frac{mW}{m^2}$ = 3.1+-.6
Mean angular diameter = 31'05.2"
Heat flow, Apollo 17, $\frac{mW}{m^2}$ = 2.2+-.5
Sid. rot. rate, rad/s = 0.0000026617
Geometric Albedo = 0.12
Mean solar day, d = 29.5306
Obliquity to orbit, $degree$ = 6.67
Orbit period, d = 27.321582
Semi-major axis, km = 384400
Eccentricity = 0.05490
Mean motion, $\frac{rad}{s}$ = $2.6616995x10^{-6}$
Inclination, $degree$ = 5.145
Apsidal period, d = 3231.50
Nodal period, d = 6798.38
Solar Constant ($\frac{W}{m^2}$) = Perihelion: 1414+-7, Aphelion: 1323+-7, Mean: 1368+-7
Maximum Planetary IR ($\frac{W}{m^2}$) = Perihelion: 1314, Aphelion: 1226, Mean: 1268
Minimum Planetary IR ($\frac{W}{m^2}$) = Perihelion: 5.2, Aphelion: 5.2, Mean: 5.2
****
Ephemeris / WWWUSER Thu Jan 2 07:13:26 2020 Pasadena, USA / Horizons
****
Target body name: Moon (301) source: DE431mx

Center body name: Earth-Moon Barycenter (3) source: DE431mx
Center-site name: BODY CENTER
****
Start time : A.D. 1970-Jan-01 00:00:00.0000 TDB
Stop time : A.D. 1977-Sep-30 00:00:00.0000 TDB
Step-size : 1440 minutes
****
Center geodetic : 0.00000000,0.00000000,0.0000000
E-lon(deg),Lat(deg),Alt(km)
Center cylindric: 0.00000000,0.00000000,0.0000000
E-lon(deg),Dxy(km),Dz(km)
Center radii : (undefined)
Keplerian GM : 3.8897282712664292E+05 $\frac{km^3}{s^2}$
Output units : KM-S, deg
Output type : GEOMETRIC osculating elements
Output format : 10
Reference frame : ICRF/J2000.0
Coordinate systm: Ecliptic and Mean Equinox of Reference Epoch
****
Coordinate system description:
Ecliptic and Mean Equinox of Reference Epoch
Reference epoch: J2000.0
XY-plane: plane of the Earth's orbit at the reference epoch
Note: obliquity of 84381.448 arcseconds wrt ICRF equator (IAU76)
X-axis : out along ascending node of instantaneous plane of the Earth's orbit and the Earth's mean equator at the reference epoch
Z-axis : perpendicular to the xy-plane in the directional (+ or -) sense of Earth's north pole at the reference epoch.
.
Symbol meaning:
JD = Julian Day Number, Barycentric Dynamical Time
EC = Eccentricity, e
QR = Periapsis distance, q (km)
IN = Inclination w.r.t XY-plane, i (degrees)
OM = Longitude of Ascending Node, OMEGA, (degrees)
W = Argument of Perifocus, w (degrees)
Tp = Time of periapsis relative to epoch (P-E) (sec)
N = Mean motion, n (degrees/sec)
MA = Mean anomaly, M (degrees)
TA = True anomaly, nu (degrees)
A = Semi-major axis, a (km)
AD = Apoapsis distance (km)
PR = Sidereal orbit period (sec)

Geometric states/elements have no aberrations applied.
****
Computations by ...
Solar System Dynamics Group, Horizons On-Line Ephemeris System
4800 Oak Grove Drive, Jet Propulsion Laboratory
Pasadena, CA 91109 USA
Information: http://ssd.jpl.nasa.gov/
Connect : telnet://ssd.jpl.nasa.gov:6775 (via browser)
http://ssd.jpl.nasa.gov/?horizons
telnet ssd.jpl.nasa.gov 6775 (via command-line)
Author : Jon.D.Giorgini@jpl.nasa.gov
****

Appendix IV - Seismometers

Apollo stations (Figure A1) consist of two main subsystems: The sensing unit and a separate electronic module built into the central transmission station. The sensing unit, shown schematically in Figure A2, contains three combined long-period (LP) sensors (with resonant periods of 15s), orthogonally aligned to measure one vertical (Z) and two horizontal (X and Y) components of surface motion. The station unit also includes a short period (SP) sensor (with a 1s resonance period) that is sensitive to vertical movement at higher frequencies. (Latham et al., 1972).

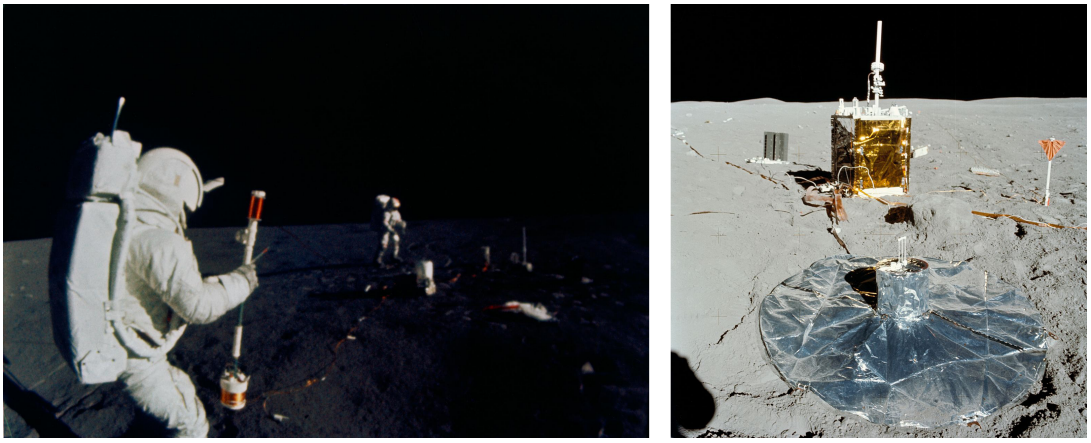

Figure A.1 Apollo seismic station. Available at: *images-assets.nasa.gov/image/S71-19509/S71-19509 orig.jpg.*

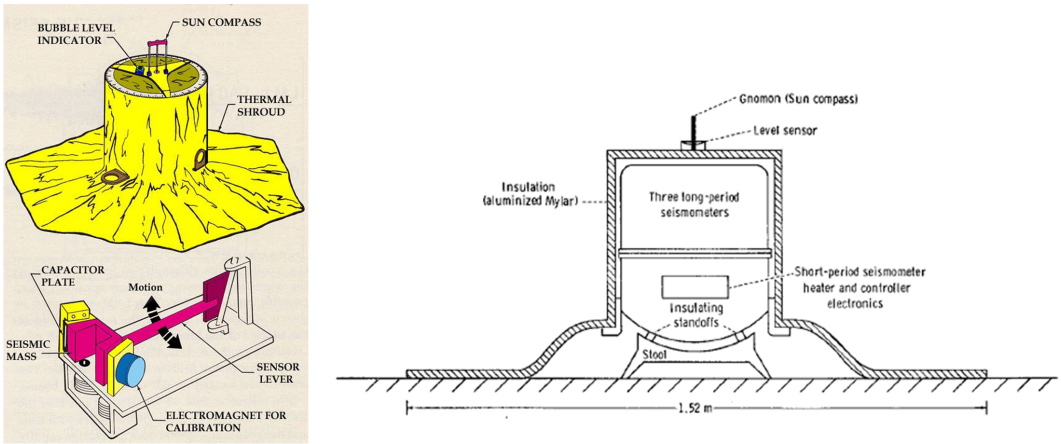

Figure A.2 The schematic sensor unit of Apollo stations. From Latham et al., 1972.

Two modes of operation of LP are possible: the flat response mode and the peak response mode. In flat mode, seismometers have natural periods of 15s and can detect ground movements as small as 0.3 nm over the frequency range 0.1Hz to 1 Hz. In peak mode, seismometers act like pendulums underground with natural periods of 2.2 s. Maximum sensitivity is increased

by a factor of 5.6 in peak response mode, but sensitivity to low-frequency signals is reduced (Latham et al., 1972). The SP can detect motion from 0.3 nm to 1 Hz with peak sensitivity at 8 Hz.

APPENDIX B

Appendix

Appendix V - Comparative summary between mother wavelets

Table B.1 Comparative summary between mother wavelets. From Cunha, 2013

Properties	Morlet	Mexh	Meyer	Haar	DbN	Gaus	SymN	CoifN	BiorNrNd
Compact support	No	No	No	2	2N-1	No	2N-1	6N-1 2	Nd+1
Symmetry	Yes	Yes	Yes	Yes	No	Yes	Near	Near	Yes
Number of nulls	-	-	-	1	N	-	N	2N	Nr-1
Scale function	No	No	Yes	Yes	Yes	No	Yes	Yes	Yes
Orthogonal Analysis	No	No	Yes	Yes	Yes	No	Yes	Yes	No
Biotorgonal Analysis	No	No	Yes	Yes	Yes	No	Yes	Yes	Yes
FIR filter (size)	No	No	No	2	2N	No	2N	6N	Yes
Fast Algorithms	No	No	No	Yes	Yes	No	Yes	Yes	Yes
CWT	Yes	Yes	Yes	Yes	Yes	Yes	Yes	Yes	Yes
DWT	No	No	Yes	Yes	Yes	No	Yes	Yes	Yes
Explicit expression	Yes	Yes	No	Yes	No	Yes	No	No	No

APPENDIX C

Appendix

Appendix VI - Theoretical Reference

C.1 Wavelet

Currently, numerous methods for analyzing frequencies and signals are available. In this context, Wavelet has been used as a method with wide applicability, as it has characteristics that allow it to be molded at different frequencies, which other methods are not capable of.

The signal analysis can be done mathematically considering it as a stationary series, however, in a real geophysical signal, the series are rarely stationary. To analyze a non-stationary system, there are two types of signal processing methods. One of them decomposes the signal based on pre-established models, where it is modeled as the sum of a finite number of frequency components. The number of components is previously established and the frequency and amplitude are estimated by the adequacy of the original signal to the model. The second group decomposes the data, based on transforms and filters, into components such as harmonics and interharmonics. These components have two forms: Analysis of the frequency domain, being ideally used for stationary signals. The Discrete Fourier Transform DFT or FFT are the most used to analysis in the time-frequency domain, being ideally used for non-stationary signals. The Short-Time Fourier Transform (STFT) method and the Discrete Wavelet Transform (WTD) are the DFT most used (Torrence and Compo, 1998) (Cunha, 2013).

The Wavelet method, was developed by Jean Morlet (Geophysicist) and Alex Grossman (Physicist) in 1981, constituting a new study base for signals. However, the theory of frequency signal analysis was initiated with the studies of Jean Fourier, in 1807, therefore, for a better understanding of the Wavelets, the function of the Fourier Transform (FT) and differences of applicability will be briefly mentioned below.

C.1.1 Fourier Transform

The Fourier Transform (FT) is a representation in the frequency domain of a function over time and it is a technique used on a large scale in signal processing. The FT of a $f(t)$ function, satisfying suitable conditions, is defined as:

$$F(\omega) = \frac{1}{\sqrt{2\pi}} \int_{-\infty}^{\infty} f(t) e^{-i\omega t}\, dt \tag{C.1}$$

The Fourier Transform is limited to the analysis of stationary signals, whose spectrum does not vary over time. FT uses sinusoidal bases to describe the signals, therefore, it has no local

character and the entire signal $(-\infty < t < \infty)$ is taken into account. This implies that the FT is efficient in determining the frequencies contained in the analyzed signal, but it is not efficient to determine the location in the time at which these frequencies occur.

To extend the use of FT to non-stationary signals, Dennis Gabor proposed an adaptation, known as Short-Time Fourier Transform (STFT) or Windowed Fourier Transform (WFT), where there is a temporal translation of a concentrated energy Gaussian function $g*(t)$ multiplied by the $f(t)$ function within the integral, under the same limits of integration:

$$F(\omega,\tau) = \int_{-\infty}^{\infty} f(t)g*(t-\tau)e^{-j\omega t}\,dt \tag{C.2}$$

The Gaussian function acts on the sinusoidal functions of the base, working as a type of modulation, generating an oscillatory wave of concentrated energy (Figure 3.1).

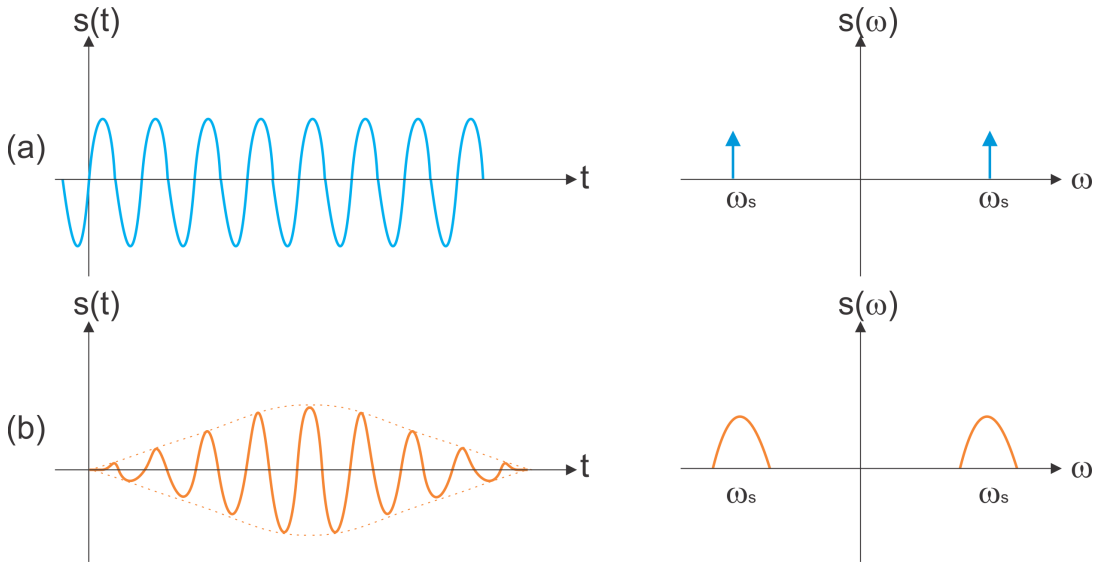

Figure C.1 (a) A sinusoidal function and its FT and (b) the modulated function and its STFT. Author's figure.

This adaptation introduces a local character to FT, dependent on the instant of evaluation, that is, a fixed-size window slides across the signal at defined intervals, mapping the signal by a two-dimensional function of time and frequency and processing the signal by a Discrete Fourier Transform.

The STFT solved the shortage of FT, simultaneously analyzing the domains of time and frequency, however, once the window size is defined (processing intervals or spreading of the Gaussian function), it remains constant for all frequencies, making "lose" information if the signal needs a more flexible approach, that is, the uncertainty relationship between the domains cannot be changed, where the analysis considers a single resolution.

Subsequently, it was understood that, for the signal analysis that present parts of low frequencies and parts of high frequencies (such as seismic signals), a analysis of multi-resolution (AMR) would be necessary, as high frequencies require a high resolution in the temporal do-

main. (small scales) and low frequencies require low resolution in the temporal domain (large scales), giving rise to the Wavelet theory.

C.1.2 Wavelet Transform

Throughout the twentieth century, ideas began to emerge to circumvent the STFT insufficiency (such as Haar (in 1910), Franklin (in 1928), Littlewood and Paley (in 1937), and Calderón (in 1964)). Wavelet analysis uses a variable window technique across the area of analysis, allowing the use of large temporal intervals, for the study of lower frequencies and shorter intervals, for high frequencies, therefore, the main characteristic of the Wavelet Transform (WT) is the multi-resolution analysis that breaks the signal down into sub-signals with different resolutions. Wavelet is defined as a function $\psi(t) \in L1(R) \cap L2(R)$ such that the family of functions is

$$\psi_{j,k}(t) = 2^{\frac{-j}{2}} \psi(2^{-j}t - k) \tag{C.3}$$

where j and k are integers, orthonormal basis for $L2(R)$, so, $\psi(t) \in L2(R)$ is equivalent to

$$\psi_{j,k}(t) = \int_{-\infty}^{\infty} |\psi(t)|^2 dt < \infty \tag{C.4}$$

$$\psi_{j,k}(t) = \int_{-\infty}^{\infty} \psi(t) dt = 0 \tag{C.5}$$

implying that $\psi(t)$ oscillates in order to cancel the positive and negative areas by dropping the integral, so the graph of $\psi(t)$ is composed of a short duration wave.

In the STFT, the functions $g_{\omega,t}(t)$, are translated for a certain time and filled with high-frequency oscillations, presenting the same width, regardless of ω. As for the functions $\psi_{j,k}(t)$ the time and width are adapted according to the frequency (the behavior of the function is based on expansions and contractions of the so-called mother wavelet).

The Wavelet Transform analysis depends on the choice of the mother wavelet. To obtain good data compression, the mother Wavelet must produce high coefficients at certain levels of interest in the signal and values close to zero for the others, making it possible to eliminate them and not compromise the waveform of the original signal. The mother wavelets have variations (Appendix V), such as short support and number of null moments. Short support is important to obtain a low number of high coefficients, making it easier to set cut levels. The null moment helps to suppress the regular shape of the signal, highlighting the shape of the transients. Unfortunately, the short support and the null moments are opposite, so a compromise between both must exist.

C.1.2.1 Continuous Wavelet Transform

The Continuous Wavelet Transform (CWT) is defined as a convolution between the $f(t)$ signal and the mother wavelet ψ scaled and translated by the 'a' and 'b' factors:

$$\psi_{a,b}(t) = \frac{1}{\sqrt{|a|}} \int f(t) \psi(\frac{t-b}{a}) dt \tag{C.6}$$

Where $\frac{1}{\sqrt{|a|}}$ normalizes the energy of the function, $\psi(\frac{t-b}{a})$ is the window, a is the scale (window size), where, smaller windows are used to analyze high frequencies and larger windows for low frequencies and b the translation factor (position in time of the mother wavelet).

In conclusion, the CWT decomposes the signal without restricting resolutions, being continuous in terms of displacement over time. The CWT delegates high computational effort, as the parameters a and b vary continuously.

C.1.2.2 Discrete Wavelet Transform

The Discrete Wavelet Transform (DWT) discretizes the parameters a and b, so that narrow wavelets are translated by small scales (for high frequencies) and wide ones by large scales (for low frequencies), optimizing the computational cost and enabling the extraction of local aspects of the analyzed signal.

The DWT calculation decomposes the signal based on the analysis of the multi-resolution (AMR) technique, which allows the study of signals in multiple frequency bands. The following equation shows the DWT calculation using the CWT as a basis with discrete scale and translation parameters, where a is the expansion and b is the translation:

$$TWD(j,k) = \frac{1}{\sqrt{a_0^j}} \sum_{n=-\infty}^{+\infty} x(n)\psi(\frac{n - kb_0a_0^j}{a_0^j}) \tag{C.7}$$

For different values of j, there are different window widths and b is dependent on j, where narrow wavelets (high frequency) are translated through small windows to cover the entire time interval, and wide wavelets (low frequency) for larger windows. Then, the translation and scaling parameters are discretized, and the independent variable (time) remains continuous, allowing greater efficiency in describing the signal in relation to CWT.

C.1.2.3 Mother wavelet Morlet

Analytical Wavelets are used in the analysis of non-stationary signals, in order to extract frequency information at different scales, with their analysis parameters varying according to the characteristics of the signal attributing versatility when locating high and low frequencies simultaneously in the same stretch. Among CWT and DWT, the most used when relating components of different frequencies in the function of the scale of a time series is CWT. Among the most well-known CWT techniques is Morlet (See Appendix V).

According to Torrence and Compo (Torrence and Compo, 1998), the first base generating function was called Morlet's Wavelet function. This function is made up of scheduling processes by a a parameter and a b variable, forming small analytical wavelets. Morlet's wavelet is a low-oscillation wavelet, temporarily located, where $f0$ is the central frequency of the mother wavelet.

Morlet's Wavelet can be understood as a periodic function combined with a Gaussian curve, having the shape of a Gaussian curve displaced along the frequency axis by $f0$. This displaced Gaussian curve is nothing more than a quarter-cycle delay of the real part of the signal.

It is worth mentioning that Morlet's Wavelet is a complex wavelet. This complexity helps to extract the oscillatory behavior of the signal, the location of events in time, non-stationarities, and singularities in the analyzed signal. In this way, the coefficient phases indicate the variations presented only in the regions of greater energy, identifying regions of discontinuity in the signal and which are more significant.

C.1.3 Wavelet Coherence

Wavelet Coherence (WC) is a technique based on CWT that allows detecting similarities between two quantities/parameters in terms of the time-scale of the series/data. The WC is used to extract causal relationships between the variables of two series, which may or may not be related, may or may not have trends, that is, it is possible to analyze how their respective occurrences are correlated over time.

The WC constitutes the normalized WT spectrum, smoothed in time and on the scale, by the energy spectrum of the individual CWT. The coefficients of the WT spectrum indicate when there is a high degree of correlation between two series/parameters. These coefficients are qualitative estimators of the temporal evolution of the degree of linearity of the interaction between the two time series on a scale, as a function of the time and frequency contained in the two series.

C.2 Machine Learning

Machine Learning (ML) is a subfield of Artificial Intelligence (AI) and its main approach is that of learning through examples, to find patterns in data sets instead of programming it with specific rules. An ML algorithm basically takes a set of input data and based on the patterns found it generates the outputs. Each entry in this data set has its features, having a set of them is the starting point for any ML algorithm. The feature is a characteristic that describes an object. Any attribute of an object can be treated as a feature, be it a number, a text, a date, etc.

There are three main classifications of algorithms used and their type of learning: Supervised Learning; Unsupervised learning; Reinforcement learning. The differentiability between these classifications is briefly described below.

C.2.1 Supervised learning

In supervised learning, a data set is given and it is known how the result should be since one has the inputs (X) and the outputs (Y) and uses the algorithm to map the learning function that will do the image of the input to the output Y = f (X), so, when the algorithm has a new input (X) it will be possible to predict which will be the output (Y), from the model produced with the rules learned from the learning function. It is called supervised learning because the learning process can be followed, where the algorithm makes the predictions about the data set and it will be correct if its responses are not according to the expected result. Problems involving supervised learning can be clustered into classification or regression subjects. In a classification problem, the output (Y) is a value between 0 and 1 that determines how close the

evaluation is to the real data. In a regression, the output (Y) is a real value.

C.2.2 Unsupervised learning

In Unsupervised learning, there is only the input (X) of data and there is no output (Y). The objective, in this case, is to model the structure or distribution of the data, to understand its characteristics. Unsupervised learning is called that because there is no feedback based on the prediction results. The algorithms are left by their own mechanisms to discover the data structure, allowing them to address problems with some or no idea about the results. Unsupervised learning problems can be grouped into clustering or association. In a clustering problem, it is desired to discover the groups inherent to the data set, grouping the data based on their characteristics. In an association problem with associative rules, to discover rules that describe large portions of your data, where the algorithms take a set of high-dimensional data and reduce it to a smaller number of dimensions so that it represents as much as possible the original data.

C.2.3 Reinforcement learning

Reinforcement learning uses trial and error, a rewarding method for success. An environment will provide data to which the computer will make decisions step by step according to them. This environment will respond with a reward (which will indicate whether the action was good or not, state of the action), this reward will determine the change of decision rules to act better in the future. The long-term goal of reinforcement learning is to maximize the rewards. The difficulty lies in the fact that the actions taken by the agent can change the environment, and the agent can obtain his reward long after his action. So, it becomes difficult to know which actions led to which reward.

C.3 Seismology

Seismology is the branch of geophysics that studies the causes and effects of quakes. Through the recording and analysis of the propagation of vibration waves transmitted by quakes, it is possible to study the interior of the Earth and other planetary bodies.

C.3.1 Basic definitions

The quake is the abrupt rupture of a fault or fracture that occurs due to the accumulation of tensions in the subsurface, generating vibrations that propagate in all directions. The point where the quake originates is called the hypocenter. The epicenter is the projection of the hypocenter on the surface, that is, the point on the surface located directly on the focus, where the quake reaches its greatest intensity. The intensity of the vibrations of a quake depends on the distance from the epicenter. A quake with great intensity, but shallow, can cause serious damage close to the epicenter. Likewise, quakes with low intensity may not cause any damage to the surface because they have a very deep focus. The energy transported by a wave depends on the amplitude of its oscillation (A) and its period (T). The amplitude of a wave is the maximum

value of the oscillation and it also varies with the distance from the epicenter. There is no direct correlation between the magnitude and intensity of a quake, where a greater magnitude can produce low intensity or vice versa. Magnitude is the amount of energy released in the quake focus, which is usually measured by the Richter Scale. The intensity is the consequence caused by the action of the quake, the destruction caused by it. The scale most used to classify the intensity is that of Mercalli.

C.3.2 The lunar seismic zone and the terrestrial seismic zone

Scientifically, the terrestrial seismic range from 0 to 700 km is divided into three zones. Surface earthquakes are between 0 and 70 km deep; intermediate earthquakes, 70 to 300 km deep; and deep earthquakes from 300 to 700 km deep, the causalities of which are largely associated with the movement of tectonic plates. This plates' junction area is called the subduction zone. More than ¾ of the deep earthquakes occur in these zones, but, although the dynamics between the tectonic plates is the main cause of earthquakes, there are other factors that can concentrate great energy, such as tectonism, volcanism, landslides, cave collapse, explosions atomic, among others, bringing a wide variation of magnitude and intensity.

On the Moon, there are four types of moonquakes: The impact moonquakes, which occur on the lunar surface; thermal moonquakes, events with small amplitude, recurring up to 50 m in depth, caused by the expansion and contraction of the crust due to wide diurnal thermal variation; the shallow moonquakes, which occur in a lunar seismic zone between 50 and 220 km, presenting greater magnitude, between 2 and 5 on the Richter Scale, possibly derived from tectonic movements of dynamics similar to those of intraplate earthquakes or to landslides in fracture zones close to the surface; and the deep moonquakes, with magnitude less than or equal to 2, that occur between a range of 700 and 1300 km on the Moon, whose causalities are still not well understood.

APPENDIX D

Attachment

Attachment I - Time series graphics

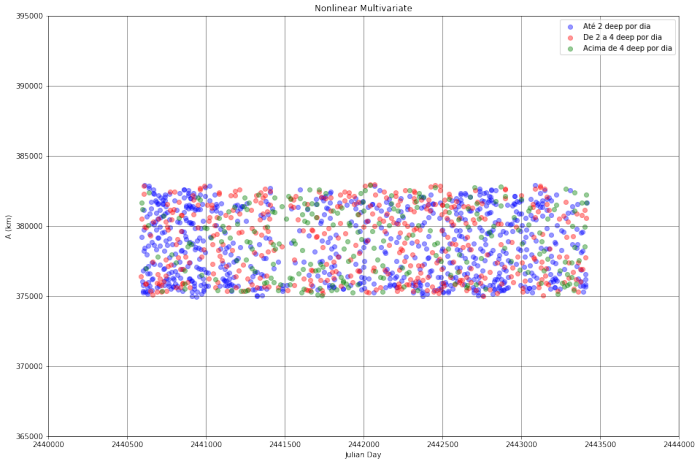

Figure D.1 Graph relating the parameter A to the number of daily deep moonquakes. In blue, until 2 deep moonquakes per day, in red between 2 and 4, and in green, more than 4 events per day.

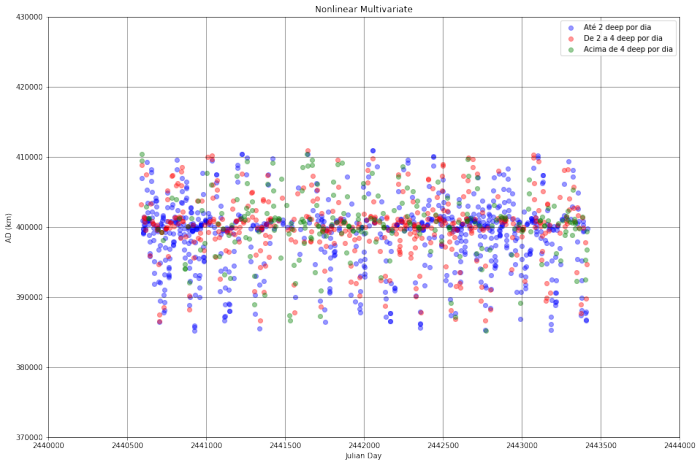

Figure D.2 Graph relating the parameter AD to the number of daily deep moonquakes. In blue, until 2 deep moonquakes per day, in red between 2 and 4, and in green, more than 4 events per day.

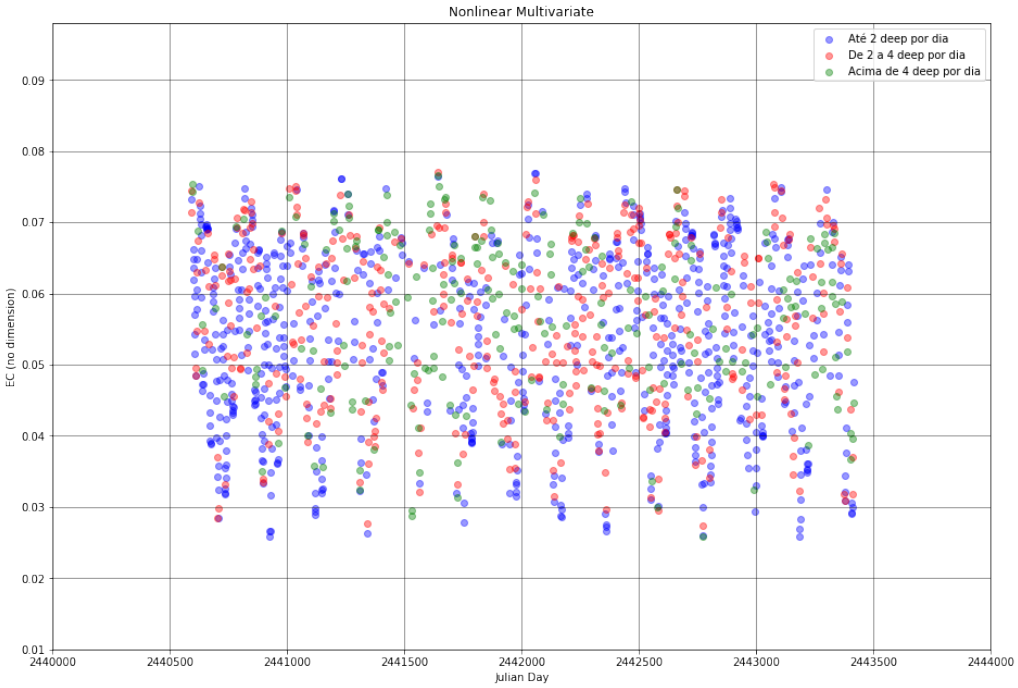

Figure D.3 Graph relating the parameter EC to the number of daily deep moonquakes. In blue, until 2 deep moonquakes per day, in red between 2 and 4, and in green, more than 4 events per day.

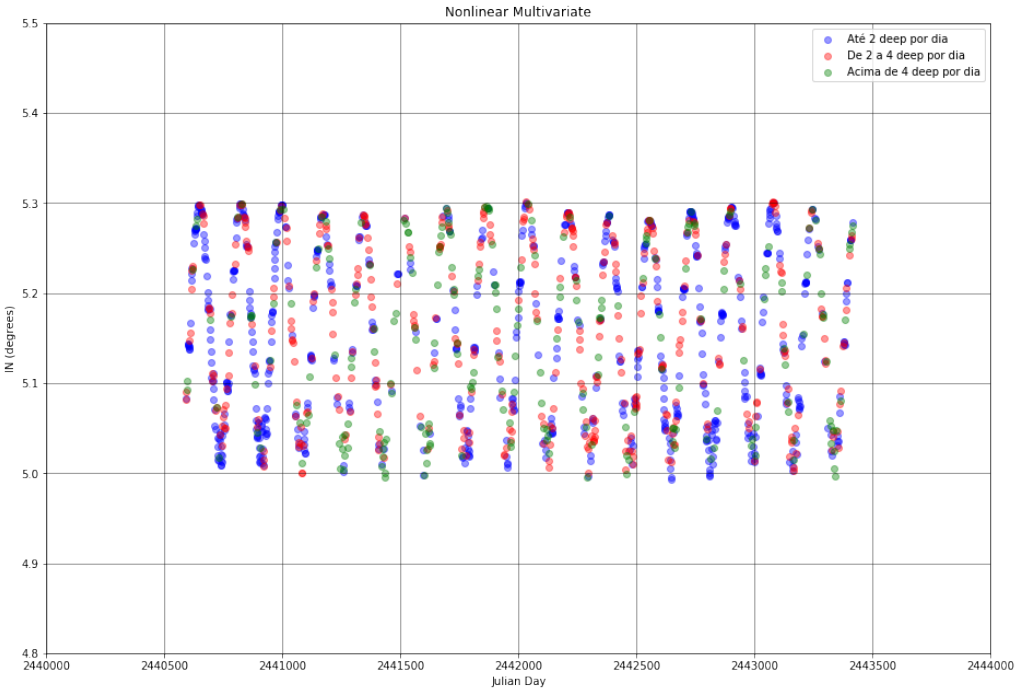

Figure D.4 Graph relating the parameter IN to the number of daily deep moonquakes. In blue, until 2 deep moonquakes per day, in red between 2 and 4, and in green, more than 4 events per day.

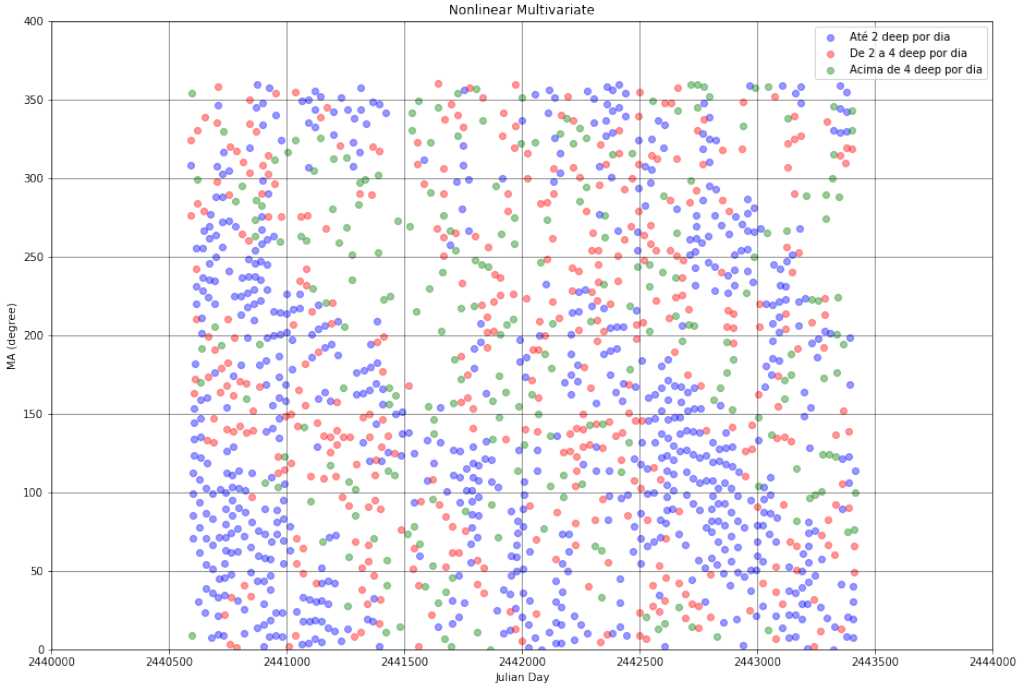

Figure D.5 Graph relating the parameter MA to the number of daily deep moonquakes. In blue, until 2 deep moonquakes per day, in red between 2 and 4, and in green, more than 4 events per day.

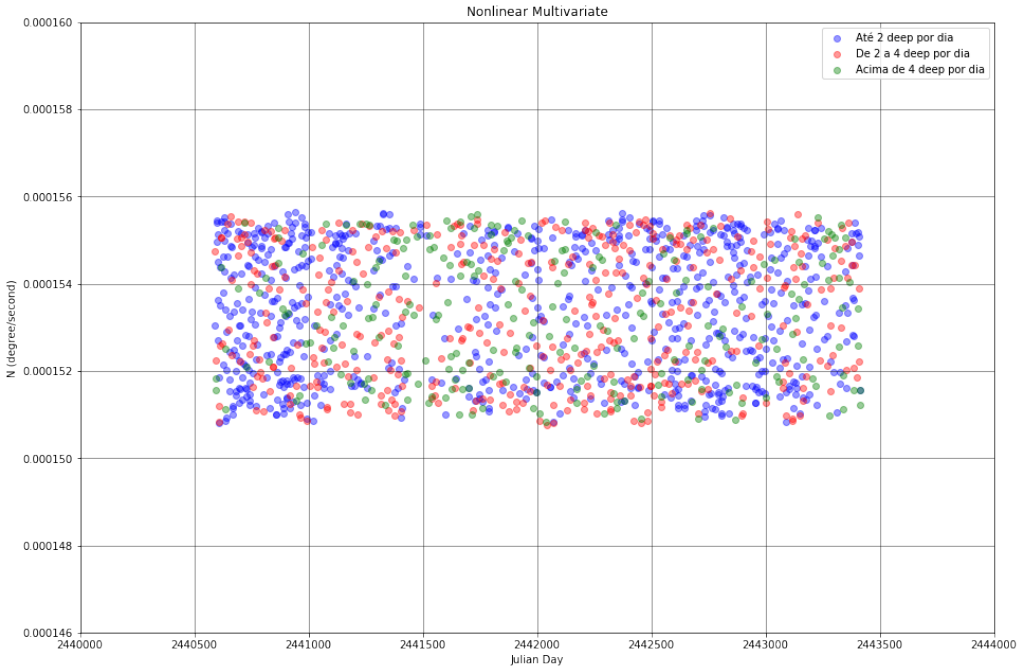

Figure D.6 Graph relating the parameter N to the number of daily deep moonquakes. In blue, until 2 deep moonquakes per day, in red between 2 and 4, and in green, more than 4 events per day.

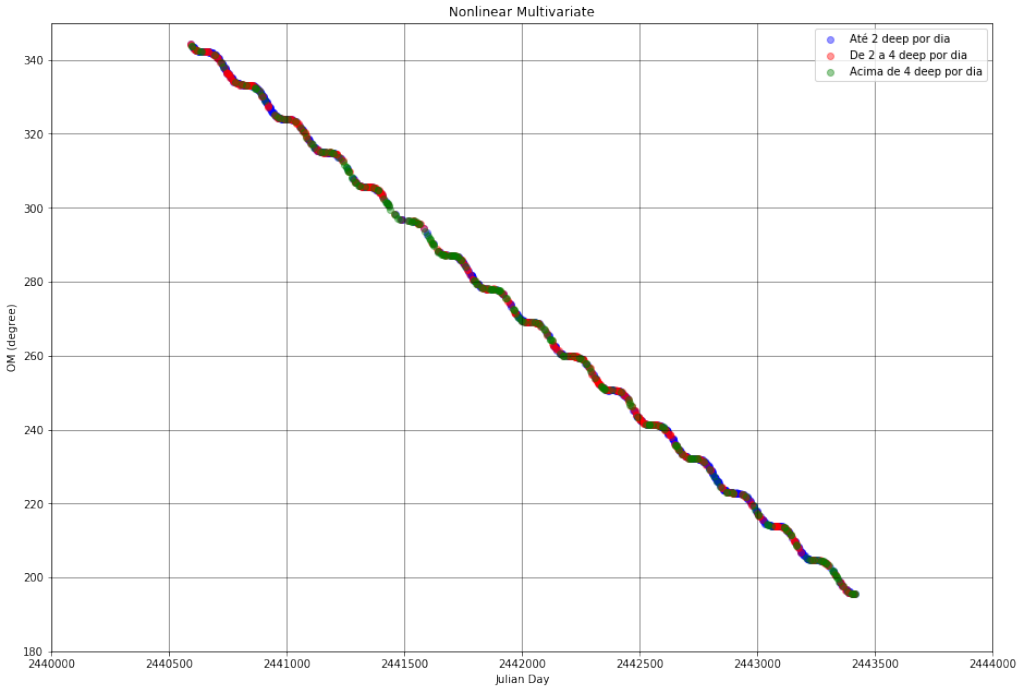

Figure D.7 Graph relating the parameter OM to the number of daily deep moonquakes. In blue, until 2 deep moonquakes per day, in red between 2 and 4, and in green, more than 4 events per day.

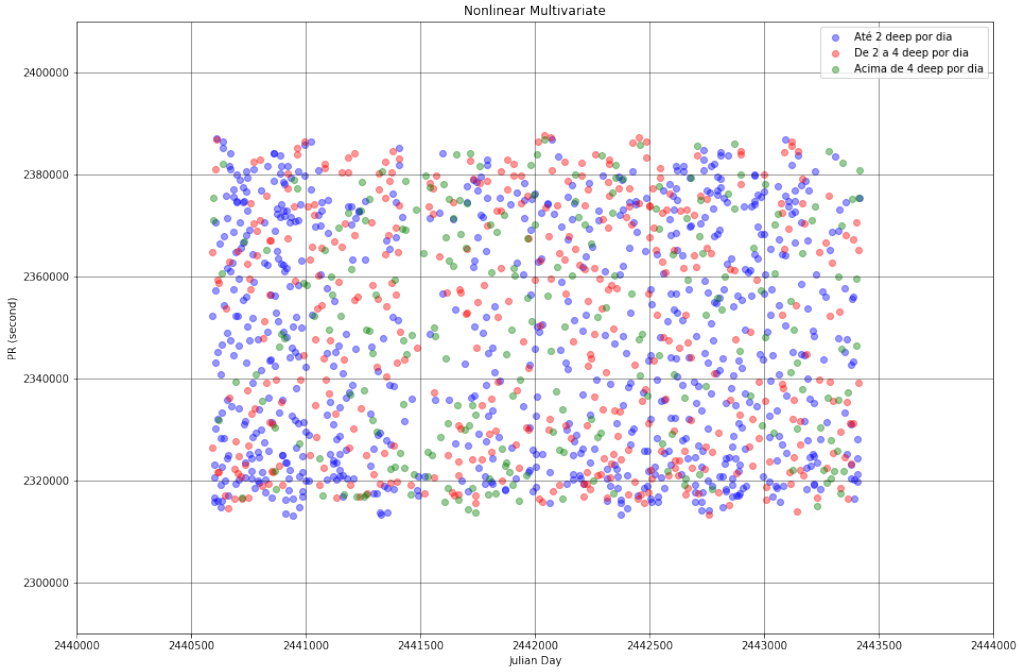

Figure D.8 Graph relating the parameter PR to the number of daily deep moonquakes. In blue, until 2 deep moonquakes per day, in red between 2 and 4, and in green, more than 4 events per day.

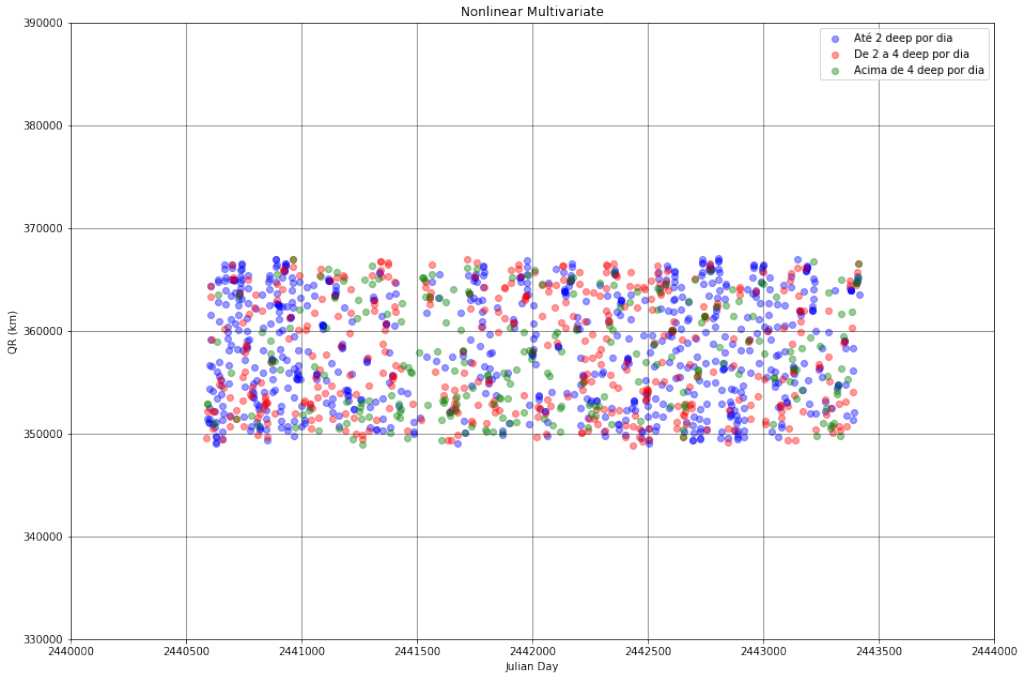

Figure D.9 Graph relating the parameter QR to the number of daily deep moonquakes. In blue, until 2 deep moonquakes per day, in red between 2 and 4, and in green, more than 4 events per day.

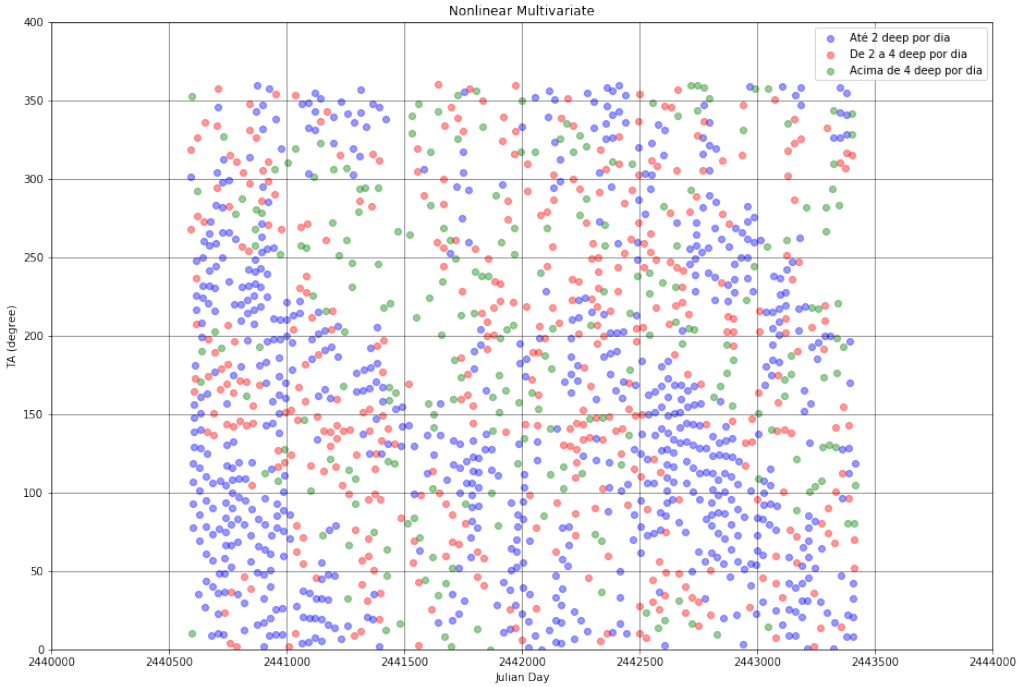

Figure D.10 Graph relating the parameter TA to the number of daily deep moonquakes. In blue, until 2 deep moonquakes per day, in red between 2 and 4, and in green, more than 4 events per day.

Figure D.11 Graph relating the parameter Tp to the number of daily deep moonquakes. In blue, until 2 deep moonquakes per day, in red between 2 and 4, and in green, more than 4 events per day.

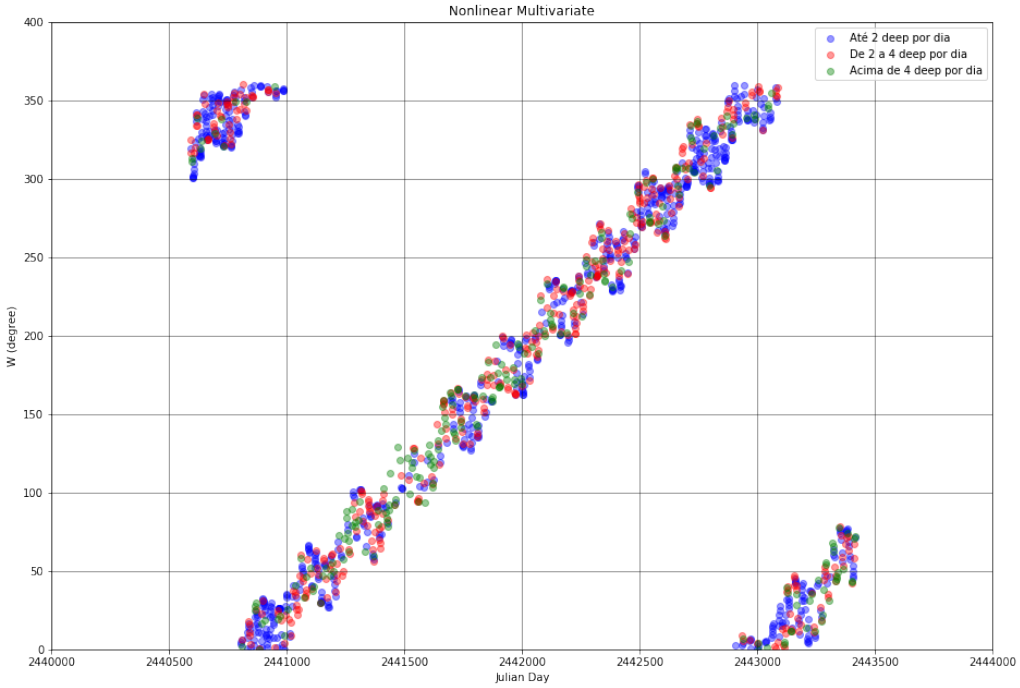

Figure D.12 Graph relating the parameter W to the number of daily deep moonquakes. In blue, until 2 deep moonquakes per day, in red between 2 and 4, and in green, more than 4 events per day.

Bibliography

Allmann, B. P. and Shearer, P. M. (2009). Global variations of stress drop for moderate to large earthquakes. *Journal of Geophysical Research*, 114:1–22.

Amoruso, A. and Crescentini, L. (2020). Parameters of the earth's free core nutation from diurnal strain tides. *Nature Scientific Reports*, 10:9756.

Arai, T., Takeda, H., Yamaguchi, A., and Ohtake, M. (2008). A new model of lunar crust: asymmetry in crustal composition and evolution. *Earth Planets Space*, 60:433–444.

Badescu, V. (2012). Moon prospective, energy and material resources. *Springer-Verlag Berlin Heidelberg*, 1:XXXVII, 749.

Bart, G., Nickerson, R., Lawder, M., and Melosh, H. (2011). Global survey of lunar regolith depths from lroc images. *Icarus*, 215 (2):485–490.

Borg, L. E., Connelly, J. M., Boyet, M., and Carlson, R. W. (2011). Chronological evidence that the moon is young or did not have a global magma ocean. *Nature*, 477:70–72.

Burmin, V. Y., Miroshnikov, V. V., and Fatyanov, A. G. (2016). On the nature of the seismic ringing of the moon. analytical modeling. *Planetary and Space Science*, 126:72–77.

Cameron, A. G. W. (2000). Higher-resolution simulations of the giant impact. *Canup, R. M., Righter, K. (Eds.), Origin of the Earth and Moon.The University of Arizona Press, Tuscon*, page 133–144.

Canup, R. M. and Asphaug, R. (2018). Origin of the moon in a giant impact near the end of the earth's formation. *Nature*, 412:708–712.

Carbone, V., Alberti, T., Lepreti, F., and Vecchio, A. (2020). A model for the geomagnetic feld reversal rate and constraints on the heat fux variations at the core mantle boundary. *Nature Scientific Reports*, 10:13008.

Chakrabarty, S. K. and Choudhury, S. N. R. (1964). Response characteristics and electromagnetic seismographs. *Bull. Seismol. Soc. Am.*, 54:1445–1458.

Chen, S. (2018). Surface of the moon, distribution of materials and structures. *Cudnik B. (eds) Encyclopedia of Lunar Science. Springer*.

Christensen, U. (2001). Geodynamic models of deep subduction. *Physics of the Earth and Planetary Interiors*, 127:25–34.

Cohen, J. K. and Stockwell Jr, J. W. (1999). Cwp/su: Seismic unix release 33: a free package for seismic research and processing, center for wave phenomenon. *Colorado School of Mines*.

Cooper, M. R., Kovach, R. L., and Watkins, J. S. (1974). Lunar near-surface structure. *Reviews of Geophysics, Volume12, Issue3*, pages 291–308.

Cuk, M., Hamilton, D. P., Lock, S. J., and Stewart, S. T. (2016). Tidal evolution of the moon from a high-obliquity highangular-momentum earth. *Nature*.

Cunha, C. F. F. d. C. (2013). Aplicação da transformada wavelet na redução de ruídos em medições de descargas parciais. *Dissertação (mestrado) – UFRJ/COPPE/Programa de Engenharia Elétrica*.

Elkins-Tanton, L. T. (2012). Magma oceans in the inner solar system. *Annual Review of Earth and Planetary Sciences*, Sci.40:113–139.

Fa, W. e. a. (2010a). Analysis of microwave brightness temperature of lunar surface and inversion of regolith layer thickness primary results of chang'e 1 multi-channel radiometer observation. *Science China Information Sciences*, Sci. 53:168–181.

Fassett, C. I. (2016). Analysis of impact crater populations and the geochronology of planetary surfaces in the innersolar system. *Journal of Geophysical Research: Planets*, 121:1900–1926.

Frohlich, C. and Nakamura, Y. (2009). The physical mechanisms of deep moonquakes and intermediate-depth earthquakes: How similar and how different? *Physics of the Earth and Planetary Interiors*, 173:365–374.

Gagnepain-Beyneix, J., Lognonné, P., Chenet, H., Lombardi, D., and Spohn, T. (2006). A seismic model of the lunar mantle and constraints on temperature and mineralogy. *Physics of the Earth and Planetary Interiors*, 159(3-4):140–166.

Geometrics Inc, L. and OYO Inc., L. (2009). Seisimager manual version 3.3 computer program manual. *Japan: OYO Corporation*.

Giroux, B. and Larouche, B. (2013). Task-parallel implementation of 3d shortest path raytracing for geophysical applications. *Computers & Geosciences*, 54:130–141.

Goins, N. R. (1978). Lunar seismology: The internal structure of the moon. *Ph. D. dissertation. M. I. T.*

Guedes, V. J. C. B., Rocha, M. P., and Maciel, S. T. R. (2018). Preliminary results of refrapy - an open-source program for seismic refraction data analysis. *International Congress of the Brazilian Geophysical Society & Expogef. Available from: https://github.com/viictorjs/Refrapy.*

Gupta, B. L. (2012). Effect of orientation of lunar apse on earthquakes. *International Journal of the Physical Sciences*, 7(6):974–981.

Hachay, O. and Khachay, O. (2019). New principles of monitoring seismological and deformation processes occurring in the moon rock massive. *Lunar Science*, page 13.

Hao, W., Li, F., Xiao, C., Yan, J., and M., Y. (2018). Understanding the moon's internal structure through moonquake observations and remote sensing technologies. *Science China Earth Sciences*, 61.

Harada, Y., Goossens, S., Matsumoto, K., Yan, J., Ping, J., and Noda, H. (2014). Strong tidal heating in an ultralow-viscosity zone at the core–mantle boundary of the moon. *Nature Geoscience*, 7:569–572.

Hartmann, W. K. and Davis, D. R. (1975). Satellite-sized planetesimals and lunar origin. *Icarus*, 24:504–515.

Heffelsa, A., Knapmeyera, M., Obersta, J., and Haasec, I. (2017). Re-evaluation of apollo 17 lunar seismic profiling experiment data. *Planetary and Space Science*, 135:43–54.

Hiesinger, H. and Head, J. (2006). New views of lunar geoscience: an introduction and overview. *Reviews in Mineralogy and Geochemistry*, 60:1–81.

Horvath, P. (1979). Analysis of lunar seismic signals – determination of instrumental parameters and seismic velocity distributions. *PhD Dissertation, University of Texas, Dallas*.

Horvath, P., Latham, G. V., Nakamura, Y., and Dorman, H. J. (1980). Lunar near surface shear wave velocities at the apollo landing sites as inferred from spectral amplitude ratios. *Journal of Geophysical Research*, 85:6572–6578.

Houston, W. N., Mitchell, J. K., and Carrier, W. O. (1974). Lunar soil density and porosity. *Lunar and Planetary Science*, Sci. Conf. 5th:2361–2364.

Hsieh, W.-P., Goncharov, A. F., Labrosse, S., Holtgrewe, N., Lobanov, S. S., Chuvashova, I., Deschamps, F., and Lin, J.-F. (2020). Low thermal conductivity of iron-silicon alloys at earth's core conditions with implications for the geodynamo. *Nature communications*, 11:3332:1–7.

Ide, S., Yabe, S., and Tanaka, Y. (2016). Earthquake potential revealed by tidal influence on earthquake size–frequency statistics. *Nature Geoscience*, 9:834–838.

Jarosch, H. S. (1977). The use of surface reflections in lunar seismograms. *Bull. Seismol. Soc. Am.*, 67:1647–1659.

Jaumann, R., Hiesinger, H., Anand, M., Crawford, I. A., Wagner, R., Sohl, F., Jolliff, B. L., Scholten, F., Knapmeyer, M., Hoffmann, H., Hussmann, H., Grott, M., Hempel, S., Kohler, U., Krohn, K., Schmitz, N., Carpenter, J., Wieczorek, M., Spohn, T., Robinson, M. S., and Oberst, J. (2012). Geology, geochemistry, and geophysics of the moon: Status of current understanding. *Planetary and Space Science*, 74(1):15–41.

Jolliff, B., Gillis, J., Haskin, L., Korotev, R., and Wieczorek, M. (2000). Major lunar crustal terranes: surface expressions and crust-mantle origins. *Journal of Geophysical Research*, 105:4197–4216.

Karato, S. (2013). Geophysical constraints on the water content of the lunar mantle and its implications for the origin of the moon. *Earth and Planetary Science Letters*, 384:144–153.

Kawamura, T., Lognonné, P., Nishikawa, Y., and Tanaka, S. (2017). Evaluation of deep moonquake source parameters: Implication for fault characteristics and thermal state. *Journal of Geophysical Research: Planets*, 122:1–18.

Khan, A., Connolly, J. A. D., Olse, n. N., and Mosegaard, K. (2006). Constraining the composition and thermal state of the moon from an inversion of electromagnetic lunar day-side transfer functions. *Earth Planet*, Sci. Lett. 248:579–598.

Kolvankar, V. G. and Atomic, B. (2010). Lunar periodicities and earthquakes. *New Concepts in Global Tectonics*, 56.

Kovalch, R. L. and Watkins, J. S. (1973). The velocity structure of the lunar crust. *The Moon*, 7:63–75.

Koyama, J. and Nakamura, Y. (1979). Re-examination of the lunar seismic velocity structure. *Lunar and Planetary Science X*, page 685–687.

Kronrod, E., Matsumoto, K., Kuskov, O., Kronrod, V., Yamada, R., and Kamata, S. (2018). Joint inversion of geophysical (seismic and selenodetic) and geochemical data for internal structure and composition of the moon. *IOP Conference Series: Materials Science and Engineering*, 468(1).

Kuskov, O. L. and Fabrichnaya, O. B. (1994). Constitution of the moon: 2. composition and seismic properties of the lower mantle. *Physics of the Earth and Planetary Interiors*, 83:197–216.

Kuskov, O. L. and Kronrod, V. A. (1998). Constitution of the moon: 5. constraints on composition, density, temperature, and radius of a core. *Physics of the Earth and Planetary Interiors*, 107:285–306.

Kuskov, O. L., Kronrod, V. A., and Kronrod, E. V. (2016). Testing the reference moon model in respect of the thermal regime and chemical composition of the mantle: Thermodynamics versus seismology. *Physics of the Solid Earth*, 52(3):344–352.

Kuskova, O. L., Kronrod, E. V., and Kronrod, V. A. (2018). Geochemical constraints on the cold and hot models of the moon's interior: 1–bulk composition. *Solar System Research*, 52:467–479.

Latham, G., Ewing, M., Dorman, J., and Nakamura, Y. (1972). Lunar structure and dynamics. *Results From The Apollo Passive Seismic Experiment*.

Lauderdale, W. W. and Eichelman, W. F. (1974). Active seismic experiment (nasa experiment s-033). *Apollo Scientific Experiments Data Handbook NASA Technical Memorandum, TM X-58131, JSC-09166*.

Ling, Z., Zhaofa, Z., Li, J., Ling, H., Zhijuna, H., Jianmina, Z., and Nan, H. (2019). A story of regolith told by lunar penetrating radar. *Icarus*, 321:148–160.

Lognonné, P., Gagnepain-Beyneix, J., and Chenet, H. (2003). A new seismic model of the moon: Implications for structure, thermal evolution and formation of the moon. *Earth and Planetary Science Letters*, 211(1-2):27–44.

Longhi, J. (2006). Petrogenesis of picritic mare magmas: Constraints on the extent of early lunar differentiation. *Geochimica et Cosmochimica Acta*, Acta 70:5919–5934.

Lv, W., Li, C., Song, H., Zhang, J., and Lin, J. (2020). Comparative analysis of reflection characteristics of lunar penetrating radar data using numerical simulations. *Icarus*, 350:113896.

Mallik, A., Ejaz, T., Shcheka, S., and Garapic, G. (2019). A petrologic study on the effect of mantle overturn: Implications for evolution of the lunar interior. *Geochimica et Cosmochimica*, 250:238–250.

Maurice, M., Tosi, N., Samuel, H., Plesa, A., Hutting, C., and Breuer, D. (2017). Onset of solid-state mantle convection and mixing during magma ocean solidification. *Journal of Geophysical Research: Planets*, 122:1–20.

McNamara, D. E. and Boaz, R. (2005). Seismic noise analysis system using power spectral density probability density functions. *Open-File Report 2005-1438. U.S. Geological Survey*.

Nakamura, Y. (2005). Farside deep moonquakes and deep interior of the moon. *Journal of Geophysical Research: Planets*, 110(1):1–12.

Nakamura, Y. (2008). Passive seismic experiment long-period event catalog. *NASA Review*, 118:1–67.

NASA (1980). Apollo seismological investigations. *NASA Reports*, Oct, 1980.

Nunn, C., Garcia, R., Nakamura, Y., and et al. (2020). Lunar seismology: A data and instrumentation review. *Space Science Reviews, volume 216, 89*.

Nédélec, A., Monnereau, M., and Toplis, M. J. (2017). The hadean–archaean transition at 4 ga: from magma trapping in the mantle to volcanic resurfacing of the earth. *Terra Nova*, 29:218–223.

Parmentier, E., Zhong, S., and Zuber, M. (2002). Gravitational differentiation due to initial chemical stratification; origin of lunar asymmetry by the creep of dense kreep? *Earth and Planetary Science Letters*, 201:473–480.

Passelègue, F. X., Almakari, M., Dublanchet, P., Barras, F., Fortin, J., and Violay, M. (2020). Initial effective stress controls the nature of earthquakes. *Nature communications*, 11:5132.

Pavlov, D. A., Williams, J. G., and Suvorkin, V. V. (2016). Determining parameters of moon's orbital and rotational motion from llr observations using grail and iers-recommended models. *Celestial Mechanics and Dynamical Astronomy*, pages 1–29.

Pernet-Fisher, J. F., Deloule, E., and Joy, K. H. (2019). Evidence of chemical heterogeneity within lunar anorthosite parental magmas. *Geochimica et Cosmochimica Acta*.

Rai, N. and Westrenen, W. (2014). Lunar core formation: New constraints from metal–silicate partitioning of siderophile elements. *Earth and Planetary Science Letters*, 388:343–352.

Rasmussen, K. and Warren, P. (1985). Megaregolith thickness, heat flow and the bulk composition of the moon. *Nature*, 313:121–124.

Shkuratov, Y. e. a. (2001). Regolith layer thickness mapping of the moon by radar and optical data. *Icarus*, 149 (2):329–338.

Silveira, F. (2009). As variações dos intervalos de tempo entre as fases principais da lua. *Revista Brasileira de Ensino de Física*, 23(3):300–307.

Szebehely, V. (1967). *Theory of Orbits*. Theory of Orbits: The Restricted Problem of Three Bodies. Academic Press.

Taylor, S. (2007). Encyclopedia of the solar system. *Chapter 12 - The Moon*, Second Edition:227–250.

Torrence, C. and Compo, G. P. (1998). A practical guide to wavelet analysis. *Bulletin of the American Meteorological Society*, 79:61–78.

Valantinas, A. and Schultz, P. (2020). The origin of neotectonics on the lunar nearside. *Geology*, 48:20.

Villanova, L. V., Yokoyama, E., and Maciel, S. T. R. (2021a). Estimation of the lunar regolith layer using apollo mission active seismic data. *Icarus*.

Villanova, L. V., Yokoyama, E., Prado, L. F., and et al (2021b). Earth-moon deep quakes triggered by orbital variability. *Nature*.

Warren, P. H. (1985). The magma ocean concept and lunar evolution. *Annual Review of Earth and Planetary Sciences*, 13:201–240.

Watters, T. R., Weber, R. C., Collins, G. C., Howley, I. J., Schmerr, N. C., and Johnson, C. L. (2019). Shallow seismic activity and young thrust faults on the moon. *Nature Geoscience*, 12:411–417.

Weber, R. (2016). Planetary seismology. *NASA Marshall Space Flight Center Huntsville Presentation*.

Weber, R. C., Bills, B. G., and Johnson, C. L. (2010). A simple physical model for deep moonquake occurrence times. *Physics of the Earth and Planetary Interiors*, 182(3-4):152–160.

Wieczorek, M. and Phillips, R. (2000). The "procellarum kreep terrane": implications for mare volcanism and lunar evolution. *Journal of Geophysical Research*, 105:20417–20430.

Wieczorek, M. A., Jolliff, B. L., Khan, A., Pritchard, M. E., Weiss, B. P., Williams, J. G., Hood, L. L., Righter, K., Neal, C. R., Shearer, C. K., McCallum, I. S., Tompkins, S., Hawke, B. R., Peterson, C., Gillis, J. J., and Bussey, B. (2006). The constitution and structure of the lunar interior. *Reviews in Mineralogy and Geochemistry*, 60:221–364.

Wiens, D. A. (2001). Seismological constraints on the mechanism of deep earthquakes: temperature dependence of deep earthquake source properties. *Physics of the Earth and Planetary Interiors*, 127:145–163.

Williams, J. G. and Boggs, D. H. (2015). Tides on the moon: Theory and determination of dissipation. *Journal of Geophysical Research: Planets*, 120:4:689–724.

Williams, J. G. and Dickey, J. O. (2002). Lunar geophysics, geodesy, and dynamics. *13th International Workshop on Laser Ranging*, pages 7–11.

Williams, J. P., Paige, D. A., Greenhagen, B. T., and Sefton-Nash, E. (2017). Geochemical constraints on the cold and hot models of the moon's interior: 1–bulk composition. *Icarus*, 282:300–325.

Witten, I., Frank, E., Hall, M., and Pal, C. (2016). Data mining: Practical machine learning tools and techniques. *654 pages, 4th edition*.

Yan, J., Goossens, S., Matsumoto, K., Ping, J., Harada, Y., Iwata, T., Namiki, N., Li, F., Tang, G., and Cao, J. (2011). Cegm02: an improved lunar gravity model using chang'e-1 orbital tracking data. *Planetary and Space Science*.

Zhan, Z. (2020). Mechanisms and implications of deep earthquakes. *Annual Review of Earth and Planetary Sciences*, 48:147–174.

Zhao, D., Arai, T., Liu, L., and Ohtani, E. (2012). Seismic tomography and geochemical evidence for lunar mantle heterogeneity: Comparing with earth. *Global and Planetary Change*, 90-91:29–36.

Zhao, Y., Vries, J., Van den Berg, A. P., Jacobs, M. H. G., and Van Westrenen, W. (2019). The participation of ilmenite-bearing cumulates in lunar mantle overturn. *Earth and Planetary Science Letters*, 511:1–11.